DETERMINATION OF SATURATED FILM DENSITIES AND VOLUMES FOR ADSORBED HYDROGEN, AND APPLICATION TO THE CALCULATION OF THE ENTHALPY OF ADSORPTION AT ROOM TEMPERATURE

In Partial Fulfillment

of the Requirements for the Degree

Doctor of Philosophy

---

by

Ernest William Knight

University of Missouri

Dr. Peter Pfeifer and Dr. Carlos Wexler, Dissertation Supervisors

December 2018

The undersigned, appointed by the Dean of the Graduate School, have examined the dissertation entitled

DETERMINATION OF SATURATED FILM DENSITIES AND VOLUMES FOR ADSORBED HYDROGEN, AND APPLICATION TO THE CALCULATION OF THE ENTHALPY OF ADSORPTION AT ROOM TEMPERATURE

Presented by Ernest William Knight,

A candidate for the degree of doctor of philosophy,

And hereby certify that, in their opinion, it is worthy of acceptance.

_____

Professor Peter Pfeifer

_____

Professor Carlos Wexler

_____

Professor Paul Miceli

_____

Professor Gavin King

_____

Professor Yuyi Lin

I dedicate this work to my family:

My parents, Ernie and Vicki Knight, have been tremendously supportive. They taught me the value of education and advancing my own knowledge. I was always encouraged to push myself and they consistently had my back. Whether the event was one of my all-day high school volleyball tournaments or driving down to Columbia for Family Weekend, they have always been by my side, both in person and in spirit. I could not ask for better parents.

Additionally, this work would not have been possible without the love and support of my other half, Kim Deasy. After dating for two years during our undergraduate studies, she stuck with me for an additional four-and-a-half-year long-distance relationship. The distance was difficult, but she might say the PhD beard was even more difficult. Despite the difficult circumstances, she has always been there to give me advice and talk me through tough times. She has been my motivation to finish this dissertation so that I can return home to her. I truly do not know where I would be without her.

I love you, Kim.

ACKNOWLEDGEMENTS

First and foremost, I would like to acknowledge the members of my thesis committee: Drs. Peter Pfeifer, Carlos Wexler, Paul Miceli, Gavin King, and Yuyi Lin for providing professional advice and working with me.

I would like to acknowledge all of the people who have contributed to this work and are not mentioned elsewhere:

University of Missouri Physics Graduate Students: Matthew Prosniewski, David Stalla, Andrew Gillespie, Elmar Dohnke, Tyler Rash, and Matthew Beckner for collaborating and working together on countless projects and for keeping spirits high.

University of Missouri Physics Undergraduate Students: Adam Smith and Mark Sweany for countless hours of Autosorb operation labor.

University of Missouri Physics Machine Shop: Rod Schlotzhauer and Cheston Callais for all the help preparing tanks and fixing instruments.

This work was supported by the United States Department of Defense, Naval Surface Warfare Center under Contract No. N00164-07-P-1306 and N00164-08-C-GS37, the United States Department of Energy, Energy Efficiency and renewable Energy under contract No. DE-FG36-08G018142, the California Energy Commission under contract No. 500-08-022, and the University of Missouri.

TABLE OF CONTENTS

TABLE OF FIGURES

ABSTRACT

The development of high-performance materials for hydrogen storage by physical adsorption requires understanding of detailed microscopic properties of the adsorbed film. In this work, we show that adsorbed hydrogen films in activated carbons have saturation densities ~100 g/L, well in excess of liquid hydrogen, and remarkably independent of sample characteristics and temperature (a property of the adsorbate only). We propose a reliable method to determine the volume of the adsorbed film at cryogenic or room temperatures by extrapolation of the low-coverage adsorption isotherms using the Ono-Kondo model and the saturation film density as a fixed point. Remarkably, film volumes are only ~40% or ~12% of the total pore volume at 77 K and 296 K, respectively (the reduction of pore volume with temperature is explained in terms of population of adsorption sites of different depths). By reliably determining the film volume, absolute adsorption isotherms for an activated carbon are calculated at 273 K and 296 K and used with the Clausius-Clapeyron relation to obtain the enthalpy of adsorption (8.3 kJ/mol, within 1.2% agreement of the low-coverage cryogenic determination for the same adsorbent, in concordance with the fact that at high temperatures deeper adsorption sites are dominant). This methodology should facilitate reliable calculations of the enthalpy of adsorption for room temperatures for weakly adsorbing gases.

This report presents the first investigation of a 5.3-liter tank, filled with 2.86 kg of University of Missouri monolithic carbon, under operation at 23 ºC (room temperature), 0 ºC (ice bath), and –79 ºC (dry-ice bath) and pressures 0-100 bar. Storage and fast charge/discharge data, including temperature and pressure profiles as a function of time are reported. These storage data agree within 2% of small-scale measurements on the commercial instrument, Hiden HTP1-V. Remarkably, the tank can be filled in 3-5 minutes, the DOE target for 2020 and later. The table below shows that there is a large temperature rise and drop, of 30-50 ºC, during filling and discharging even at room temperature. These are unexpectedly large temperature excursions because binding of H_2 on

carbon, with a typical heat of adsorption of 5.0 kJ/mol (H_2 on graphite), is considered weak and a source of major temperature excursions only at liquid nitrogen temperature. It shows, as expected, that equilibration is faster at high temperature than at low temperature.

Key results for the three tank configurations are as follows.

	23 ºC	0 ºC	–79 ºC
Equilibrium data			
Mass of H_2 stored	0.049 kg	0.055 kg	0.093 kg
Gravimetric storage at 100 bar	0.017 kg H_2/kg C 1.7 material wt%	0.019 kg H_2/kg C 1.9 material wt%	0.032 kg H_2/kg C 3.1 material wt%
Volumetric storage at 100 bar	0.009 kg H_2/L tank	0.010 kg H_2/L tank	0.018 kg H_2/L tank
Adsorbed film volume	0.17 cm^3/g	0.18 cm^3/g	N/A
Saturated Film Density	100 g/L	100 g/L	N/A
Kinetic data, fast fill			
Time to reach 100 bar	4.8 min	3.9 min	N/A
Percentage full at 100 bar	94%	90%	N/A
Temp. at 100 bar (max. temp.)	56 ºC	42 ºC	N/A
Time constant, press. drop after peak	6.9 min	7.3 min	N/A
Time constant, temp. drop after peak	7.2 min	8.1 min	N/A
$\Delta P/\Delta T$	0.19 bar/ºC	0.33 bar/ºC	N/A
Kinetic data, fast discharge			
Time to reach 2 bar	4.0 min	4.6 min	N/A
Temp. at 2 bar (min. temp.)	–25 ºC	–50 ºC	N/A
Time constant, press. rise after 2 bar	5.2 min	4.8 min	N/A
Time constant, temp. rise after 2 bar	5.8 min	5.1 min	N/A
$\Delta P/\Delta T$	0.02 bar/ºC	0.02 bar/ºC	N/A

1 Introduction

Due to the environmental impact and finite supply of conventional fossil fuels, substantial steps are needed to seek a cleaner, more sustainable fuel source. Hydrogen-based systems only produce water as a byproduct, making it one of the most desirable alternative fuel sources, especially when produced through sustainable and non-polluting methods such as solar electrolysis or biohydrogen [1]. Hydrogen fuel cell systems can be smaller, weigh less, and can be charged in minutes instead of hours compared to batteries [2]. The largest hurdle to using hydrogen is the storage of the gas itself. In order to make hydrogen a viable fuel source, the low volumetric energy density of hydrogen at ambient conditions (0.0107 MJ/L) must be increased by orders of magnitude to match the energy density of gasoline (31.1 MJ/L) [3].

Current hydrogen-based systems rely solely on liquefying or compressing the gas. Liquefying hydrogen requires expensive refrigeration systems to achieve the low temperatures down to 20 K [4]. Prototype fuel cell vehicles using compression operate at pressures up to 700 bar [4,5]. This level of compression requires large, heavy metallic or expensive carbon fiber gas cylinders that occupy a significant amount of cargo space for storage [6,7]. This reduces the volumetric storage capacity of the entire system.

In addition to the practical difficulties of storing hydrogen at such extreme conditions, a significant amount of energy is lost during liquefaction or compression (~1/3 and ~1/5 of the heating value of hydrogen) [8]. Alternatively, systems utilizing adsorption can greatly increase the stored energy density. Adsorbent materials utilize the van der Waals attraction between the adsorbent and the hydrogen molecules inside of the nanoporous structure, to create a high density film [9–11]. These film densities (100 g/L) can exceed that of liquid hydrogen (71 g/L) [12].

In order to improve the storage capability of an adsorbent material, research has focused on increasing the surface area, optimizing pore geometry, and increasing the adsorption energy. The hydrogen binding energy for most materials is between 4 and 7 kJ/mol [13–17]. Numerical estimates show that an adsorption energy between 12 and 20 kJ/mol will be necessary for ambient temperature operating conditions [13–18]. One method to increase the adsorption energy in microporous materials is to change the pore width to create an overlapping adsorption potential. For activated carbons, the pore widths can be tuned by adjusting the activation parameters [19], e.g. in metal-organic-frameworks (MOFs) the length of the linker can be adjusted to achieve different pore widths [20]. Determining the enthalpy of adsorption of hydrogen is difficult at cryogenic temperatures, but even harder at room temperature. This is due to the relatively weak binding at higher temperatures.

In this paper we seek to develop a method to calculate the enthalpy of adsorption at room temperature using the Clausius-Clapeyron relation between two absolute adsorption isotherms. To get reliable results it is fundamental to know the volume occupied by the adsorbed film, which is normally not available. Firstly, we determined that the density of the adsorbed film at saturation $\rho_{\mathrm{film,sat}}$ is remarkably sample and temperature independent, making it a robust property of the adsorbed gas itself (thus this result should apply to any sample). This result complemented high temperature isotherms to determine the adsorbed film volume using the Ono-Kondo model [21,22] (the film volume is roughly proportional to the specific surface area, decreases with temperature and is significantly smaller than the available pore volume). The enthalpy of adsorption, thus determined has a much lower uncertainty than the large range permitted by the most common assumptions, and lacks the unphysical rise with coverage sometimes reported. The results should be applicable to a wide range of samples and temperatures.

Table 1. DOE Technical Targets for Onboard Hydrogen Storage for Light-Duty Vehicles from 2017

Storage Parameter	**Units**	**2020**	**2025**	**Ultimate**
System Gravimetric Capacity	Kg H_2/kg system	0.045	0.055	0.065
System Volumetric Capacity	Kg H_2/L system	0.030	0.040	0.050
Fuel Cost	\$/kg H_2	333	300	266
Operating Ambient Temperature	^{o}C	-40/60	-40/60	-40/60
Min/Max Delivery Temperature	^{o}C	-40/85	-40/85	-40/85
Operational Cycle Life (1/4 Tank to Full)	cycles	1500	1500	1500
Min Delivery Pressure From Storage System	bar (abs)	5	5	5
Max Delivery Pressure From Storage System	bar (abs)	12	12	12
System Fill Time	min	3-5	3-5	3-5
Minimum Full Flow Rate	(g/s)/kW	0.02	0.02	0.02
Average Flow Rate	(g/s)/kW	0.004	0.004	0.004

1.1 Adsorption

The Lennard-Jones potential is a mathematically simple model that can approximate the interaction between gas molecules and the adsorbent surface [23]. This potential is expressed as

$$V_{\mathrm{LJ}} = \varepsilon \left[\left(\frac{r_{\mathrm{m}}}{r} \right)^{12} - 2 \left(\frac{r_{\mathrm{m}}}{r} \right)^{6} \right] \tag{1}$$

where ε is the depth of the potential well, r is distance between the molecule and the surface, and r_{m} is the distance at which the potential reaches its minimum.

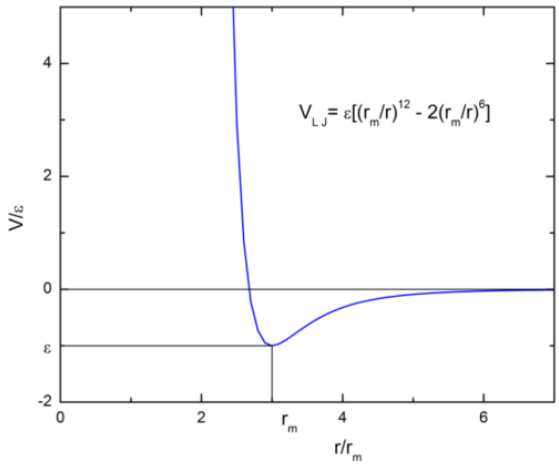

Figure 1. Arbitrary Lennard-Jones potential energy curve as a function of distance from the sorbents surface. The minimum corresponds to the equilibrium distance between an adsorbent and the adsorbate gas.

The r^{-12} term is the short-range repulsive interaction. This is referred to as Pauli repulsion and arises from the overlapping of electron orbitals. The r^{-6} term contains the longer-range attractive interactions. This describes the van der Waals forces. The attractive forces contain Keesom, Debye, and London interactions. The Keesom interaction includes attractive or repulsive electrostatic interactions between permanent charges, dipoles, quadrupoles, and higher order multipoles [24–27]. The Debye interaction (induction or polarization) includes attractive interactions between a permanent multipole on one molecule with an induced multipole on the other [28,29]. And the London interaction (dispersion) includes attractive interactions between a pair of molecules caused by the interactions of instantaneous multipoles [30–32]. The three interaction energies decay very steeply with increasing distance (r^{-6}). Only the London (dispersion) interactions are of significance between macroscopic bodies in condensed systems [33,34]. The addition of these dispersion interactions makes them considerably more long-range; the dispersion energy between two semi-infinite parallel flat slabs decays as r^{-2} [35] for relatively short distances (r < 100 Å) and, due to retardation, as r^{-3} at greater distances [33,36].

These van der Waals interactions lead to the surface phenomenon known as adsorption. In the adsorption process an adsorbate gas will increase in density near the surface of a material. Though hydrogen may be contained at a pressure and temperature at which it would be a low-density gas, introducing an adsorbent material with strong van der Waals forces can condense the hydrogen into a high-density fluid near the surface of the material. One of the primary variables which produce this phenomenon is the large amount of internal surface area in the network of pores in an adsorbent material. This large surface area yields many sites for gas molecules to bind to. The network of pores can also lead to an overlapping of these van der Waals potentials that can trap these molecules. The essential quantity that can be measured on an adsorbent material is excess adsorption. Excess adsorption is defined as follows[37]:

> "*Consider two systems of equal volume. The first system is that of free gas at a temperature T_0, pressure p_0, and contains N_0 gas molecules. The second system contains an external potential $U(\vec{r})$ due to an adsorbing surface outside of the system and the gas has a temperature T, pressure p far from the adsorbing surface, and contains N gas molecules. If both systems have the same temperature and pressure (i.e. $T = T_0$ and $p = p_0$), then the excess adsorption is given by N-N_0*"

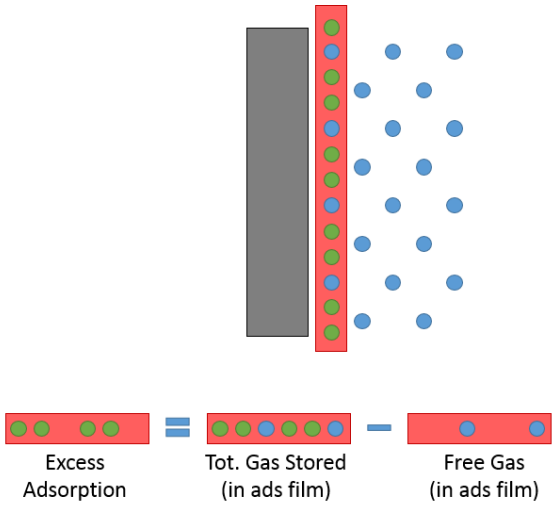

Figure 2. An adsorption schematic of gas in the adsorbed film. The black box is the adsorbent material. Some gas (green circles) is bound to the surface via van der Waals interaction. The other gas (blue circles) is free gas or in the bulk phase. To truly obtain excess adsorption, one must subtract out the gas in the bulk phase.

The following section will provide an overview of the adsorption measurement process and define useful metrics.

1.2 Adsorption Metrics

In our laboratory, there are three different methods for measuring experimental hydrogen adsorption isotherms:

(a) Manometric or volumetric

(b) Gravimetric

(c) With flow meter

Manometric instruments rely on counting particles and having an absolute determination in the several volumes of which the system is comprised. Gravimetric instruments rely solely on the mass of gas in the system. These instruments can be as simple as just adding gas to the sample cell until

it thermally equilibrates and recording the mass increase with a scale. The primary instrument used to collect data in this report utilizes a well calibrated mass flow meter in order to determine how much mass of gas enters the system.

The gravimetric excess adsorption measurements discussed in this report were taken on two instruments. A large sample (2.86 kg) was measured with our 10-Liter Storage System (10LSS). The 10LSS consists of two 5.3-L modular tanks, filling/discharging mass flow meters, and thermal bath vessels. One of the 5.3-L tanks was packed with the 2.86 kg of monoliths. A small sample (~300 mg, 1 cm^3) was measured on the commercial instrument Hiden HTP1-V.

Gravimetric Excess adsorption is the only directly measurable quantity that requires no assumptions of the pore volumes [38], it is calculated from experimental data as

$$G_{\mathrm{ex}} = \frac{m_{\mathrm{H_2,tank}}}{m_{\mathrm{s}}} - \frac{\rho_{\mathrm{gas}}}{m_{\mathrm{s}}}(V_{\mathrm{tank}} - V_{\mathrm{skel}}), \tag{2}$$

where m_{s} is the sample mass, $m_{\mathrm{H_2,tank}}$ is the mass of gas in the system, ρ_{gas} is the compressed gas density, V_{tank} is the volume of the tank or cell, and V_{skel} is the volume of the carbon, known from helium pycnometry. In our analysis, in order to mitigate uncertainties [39], we ensured all instruments were well calibrated and leak proof, samples were outgassed and thermally controlled, ultra-purified hydrogen gas was used. The extremely large sample size aided in reducing the relative error of our excess adsorption measurements.

Gravimetric and volumetric storage capacity are useful engineering metrics. They can be calculated from excess adsorption and porosity measurements. Gravimetric storage capacity is defined as the total amount of adsorbate gas. It can be calculated by

$$\frac{m_{\mathrm{st}}}{m_{\mathrm{s}}} = \frac{m_{\mathrm{ex}}}{m_{\mathrm{s}}} + \frac{\rho_{\mathrm{gas}}}{m_{\mathrm{s}}} V_{\mathrm{void}} \equiv G_{\mathrm{st}} \tag{3}$$

where V_{void} is the total void volume of the system and is equal to the total volume available to the adsorbate gas. It can be convenient to define gravimetric storage capacity in terms of the porosity of the system, defined as

$$\phi = \frac{V_{\mathrm{void}}}{V_{\mathrm{system}}} \tag{4}$$

However, the definitions of these two volumes depend on whether we are referring to the crystalline (envelope) or the tank (bed) porosity. The envelope porosity is defined as the amount of open pore volume normalized to the volume of the total system.

$$\phi_{\mathrm{cryst}} = \frac{V_{\mathrm{pore}}}{V_{\mathrm{system}}} = \frac{V_{\mathrm{pore}}}{V_{\mathrm{pore}} + V_{\mathrm{skel}}} \tag{5}$$

where V_{pore} is the open pore volume of the adsorbent material. The crystalline porosity does not include the gas stored between individual grains of material.

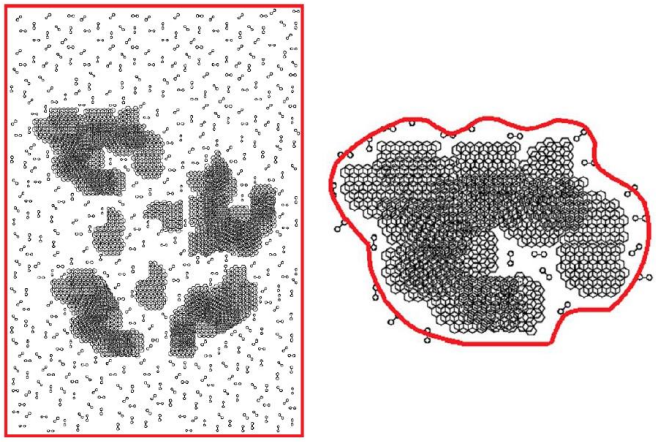

Figure 3. System volumes used in defining porosity. *Left*: System volume for a tank containing adsorbate gas molecules and adsorbent material (gray). This system includes the skeletal volume of the sample, the pore volume of the sample, and the intergranular void space. *Right:* Volume of one crystal of a carbon-based material. This system includes the skeletal volume and the pore volume of the sample [40].

The tank porosity is defined as the amount of

pore volume and intergranular space normalized to the system volume.

$$\phi_{\text{tank}} = \frac{V_{\text{void}}}{V_{\text{system}}} = \frac{V_{\text{pore}} + V_{\text{inter granular}}}{V_{\text{pore}} + V_{\text{skel}} + V_{\text{inter granular}}} \tag{6}$$

Where $V_{\text{inter granular}}$ is defined as the void space between individual grains of adsorbent material [41]. Gravimetric storage capacity can be written in terms of the porosity

$$G_{\text{st}} = G_{\text{ex}} + \frac{\rho_{\text{gas}}}{\rho_{\text{skel}}}\left(\phi^{-1} - 1\right)^{-1} \tag{7}$$

where ρ_{skel} is the skeletal density of the adsorbent material. The void space between individual grains of adsorbent material needs to be accounted for in a tank system [41].

The packing fraction of a system depends on the amount of intergranular void space present [42–44]. The volumetric storage capacity is defined as the total amount of adsorbate gas in the system normalized to the system volume. Since the total mass of gas stored in the system is the same as in the calculation of gravimetric storage capacity, one only needs to multiply by the density of the system to convert to volumetric storage capacity. Therefore, volumetric storage capacity can be calculated by [45]

$$V_{\mathrm{st}} = G_{\mathrm{st}}\rho_{\mathrm{system}} = G_{\mathrm{ex}}\rho_{\mathrm{skel}}(1-\phi) + \rho_{\mathrm{gas}}\phi \tag{8}$$

Here V_{st} and G_{st} are related through several factors including porosity and excess adsorption. **Figure 4** demonstrates the possible variance in storage capacities for activated carbon samples that have a typical ρ_{skel} of 2.0 g/cm^3.

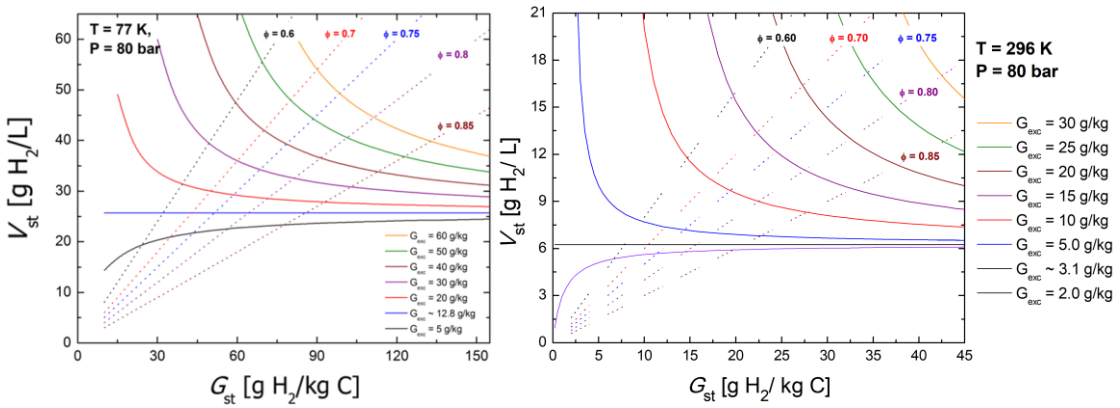

Figure 4. System volume Volumetric (V_{st}) vs. gravimetric (G_{st}) storage capacities, with curves of constant excess adsorption (G_{ex}) and constant porosity (ϕ) at 77 K and 296 K. Reproduced from Ref. [46].

One of the methods for increasing storage capacity is to increase the specific surface area. In most circumstances, increasing the specific surface area will increase the number of adsorption sites for

gas molecules to bind to [47,48]. However, there can be physical limits to how large the SSA may be. The maximum theoretical surface area is 2,965 m^2/g [49]. On the other hand, it has been theorized that by removing carbon atoms, a surface area as high as 7,000 m^2/g may be achieved [50].

Absolute adsorption is a metric that is necessary to determine an adsorbent material's enthalpy of adsorption. G_{abs} isdifferent than gravimetric storage capacity in that absolute adsorption only includes gas molecules in the adsorbed phase and does not include gas in the bulk phase. The absolute adsorption is defined as the total mass of adsorbate gas in the adsorbed film per mass of sample and can be expressed as

$$G_{\mathrm{abs}} = \frac{m_{\mathrm{abs}}}{m_{\mathrm{s}}} = G_{\mathrm{ex}} + \rho_{\mathrm{gas}} V_{\mathrm{film}} \tag{9}$$

where V_{film} is the specific film volume of the material. This conversion requires knowing or estimating the adsorbed film volume. A method for determining V_{film} will be explored in **sections 1.3** and **5.1.**

Deliverable storage capacity can be a useful metric to determine how beneficial it is to introduce an adsorbent material into an operating tank system. In order to determine the deliverable storage capacity of a tank, one must know the amount of gas stored at the maximum operating pressure of the tank, P_{max}, and at the rail pressure of the system, P_{rail}. The volumetric storage capacity can be defined as

$$V_{\mathrm{st,Del}} = V_{\mathrm{st}}(P_{\mathrm{max}}) - V_{\mathrm{st}}(P_{\mathrm{rail}}) \tag{10}$$

Deliverable storage capacity will be further explored in **section 6**.

1.3 Enthalpy of Adsorption and Absolute Adsorption

Much of the ongoing research among adsorption scientists involves efforts into estimating the differential enthalpy of adsorption. This is an especially important metric for adsorbent material performance. This metric can determine the adsorbed film volume capacity of a material. It also determines how readily gas will desorb, thus dictating the materials deliverable storage capacity. A high enthalpy will lead to a large adsorbed film volume, but can lead to a reduction in deliverable fuel. Therefore, it is desirable to find an adsorbent material with an optimal enthalpy of adsorption, which is proposed to exist between 10-20 kJ/mol [13–18]. A common approach to calculating the enthalpy of adsorption is to apply the Clausius-Clapeyron relation to isothermal data from two different temperatures [9,51]. The Clausius-Clapeyron relation is expressed as

$$\Delta H = \frac{RT_1T_2}{T_2 - T_1} ln \frac{P_2}{P_1} \tag{11}$$

where T_1 and T_2 are the temperatures at which the two adsorption measurements were taken and P_1 and P_2 are the pressures at which a constant number of particles exist in the adsorbed phase[9]. As discussed in Ref. [52], the isotherms need to be compared at equal absolute adsorption, G_{abs}. Experimentally, only the excess adsorption G_{ex} is measured directly, thus a conversion is necessary. In order to determine the enthalpy of adsorption. Converting excess into absolute adsorption requires knowledge or estimation of the adsorbed film volume. Common assumptions are $V_{\mathrm{film}} = 0$ (i.e., G_{ex}) and $V_{\mathrm{film}} = V_{\mathrm{pore}}$ (which overestimates $G_{\mathrm{abs}} = G_{\mathrm{st}}$, obviously $V_{\mathrm{film}} \leq V_{\mathrm{pore}}$). The former assumption overestimates ΔH, whereas the latter underestimates it [53–56]. We observe in **Sec. 5.1** that for BR-0311 V_{film} = 0.58 cm^3/g at cryogenic temperatures (≈ 40% of V_{pore} = 1.45

cm^3/g); at room temperature, the discrepancy is even higher ($V_{film} \approx 0.12\ V_{pore}$, **Sec. 5.1)**. Some researchers will take the entire pore volume to be the film volume, because the total pore volume can easily be determined from subcritical nitrogen isotherms. If this assumption is made, the absolute adsorption will become equal to the gravimetric storage capacity. Once converted into absolute adsorption, the data can be fit with an appropriate model in order to interpolate the pressure corresponding to absolute adsorption values. Differences in model choice can yield slightly different enthalpy values, especially at low coverage (absolute adsorption). In this report, all absolute adsorption isotherms were interpolated using the Modified Redlich-Peterson Model, because it fits the data incredibly well ($R^2 > 0.9999$). The original Redlich-Peterson Model is expressed as

$$G_{abs} = \frac{aP}{1 + bP^c} \tag{12}$$

where a, b, and c are empirical constants. The model obeys Henry's Law in the low pressure limit, however it requires numeric approximation methods to interpolate between experimental data [57]. The Modified Redlich-Peterson Model is expressed as

$$G_{abs} = \frac{a(bP)^{1-c}}{1 + (bP)^{1-c}} \tag{13}$$

where a, b, and c are empirical constants. This model does not satisfy Henry's Law. It does however allow for pressures to be calculated analytically, thus no need for numeric methods. After all fitting parameters have been determined for the isothermal data, P_1 and P_2 can be determined analytically and Eq (8) can be used to calculate the enthalpy of adsorption for any intersecting points of constant coverage. This estimation method is highly sensitive to the choice of adsorbed film volume and quality of the model used to fit experimental data.

In order to determine the film volume, we start with the equation for Gibbs excess adsorption, given by

$$m_{\text{ex}} = \int_{V_{\text{ads}}} (\rho_{\text{ads}} - \rho_{\text{gas}}) dV \tag{14}$$

where V_{ads} is the adsorbed film volume, ρ_{ads} is the density of the adsorbed film volume, and ρ_{gas} is the bulk gas density. A large majority of cryogenic excess adsorption isotherms tend to show a linear regime at high pressures. This occurs when the monolayer closest to the surface reaches saturation and increasing layers observe insignificant adsorption. After this adsorbed film reaches saturation, V_{ads} and ρ_{ads} become constant with increasing ρ_{gas}.

$$m_{\text{film}} = \int_{V_{\text{ads}}} \rho_{\text{ads}} dV = const. \tag{15}$$

alternatively,

$$m_{\text{ex}} = m_{\text{film}} - \int_{V_{\text{ads}}} \rho_{\text{gas}} dV \tag{16}$$

and

$$\frac{dG_{\text{ex}}}{d\rho_{\text{gas}}} = -V_{\text{film}} \tag{17}$$

As a result, the equation becomes linear with a negative slope with increasing bulk gas density. The magnitude of the slope is the saturated, adsorbed film volume and the intercept is equal to the monolayer capacity [40,46,58]. So as long as the excess adsorption vs gas density data experiences

a maximum and has a sufficient linear regime, the data can be linearly fit in the high-density limit. This happens frequently for most cryogenic isotherms, but only a few samples exhibit such a linear regime, or even a local maximum in excess adsorption, at room temperature and pressures less than 200 bar. One such sample is shown in **Figure 5**.

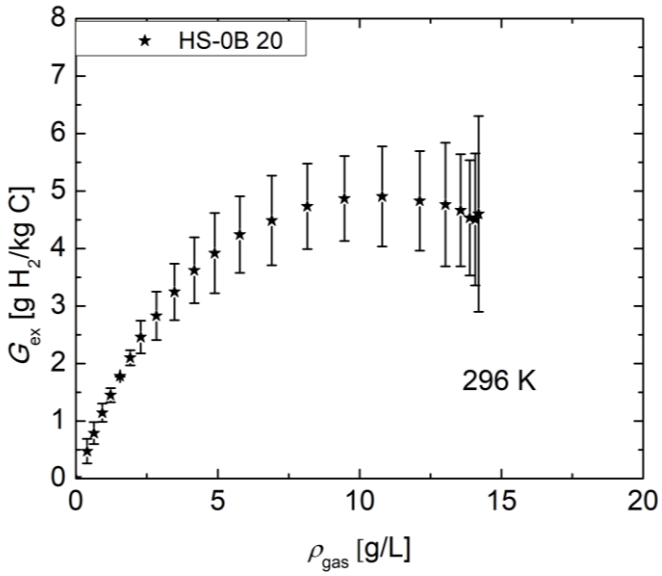

Figure 5. Gravimetric excess adsorption for HS-0B 20.

HS-0B 20 was the only sample measured to exhibit a local maximum at room temperature. The uncertainty in the measurement is fairly large and the linear regime does not appear to be very well defined.

The case for any other samples at non-cryogenic is to estimate the rest of the isotherm with a quality model. The model of our choice for these excess adsorption fits is the Ono-Kondo adsorption model [21,22], which is expressed as

$$G_{\mathrm{ex}} = 2a\frac{\left(1-\frac{\rho}{b}\right)\left(1-e^{c/T}\right)}{1+\left(\frac{b}{\rho}-1\right)e^{c/T}} = 2a\frac{\left(1-\frac{\rho_{\mathrm{gas}}}{\rho_{\mathrm{film,sat}}}\right)\left(1-e^{E_B/RT}\right)}{1+\left(\frac{\rho_{\mathrm{film,sat}}}{\rho_{\mathrm{gas}}}-1\right)e^{E_B/RT}} \tag{18}$$

In this model the excess adsorption is a function of gas density (ρ_{gas}). Parameter a is a scaling factor, b is the saturated adsorbed film density ($\rho_{\mathrm{film,sat}}$), and c is the binding energy of the gas-solid interaction (E_B/R), and T is the temperature of the isotherm. The next assumption is that the isothermal data will eventually become linear and scale with the adsorbed film volume [58]. Taking the derivative of the model with respect to the gas density yields

$$\frac{dG_{\mathrm{ex}}}{d\rho_{\mathrm{gas}}} = -\frac{2a\left(1-e^{E_{\mathrm{B}}/RT}\right)}{1+\left(\frac{\rho_{\mathrm{film,sat}}}{\rho_{\mathrm{gas}}}-1\right)e^{E_{\mathrm{B}}/RT}}\left[\frac{1}{\rho_{\mathrm{film,sat}}}-\frac{\left(1-\frac{\rho_{\mathrm{gas}}}{\rho_{\mathrm{film,sat}}}\right)\left(\frac{\rho_{\mathrm{film,sat}}e^{E_{\mathrm{B}}/RT}}{{\rho_{\mathrm{gas}}}^2}\right)}{\left(1+\left(\frac{\rho_{\mathrm{film,sat}}}{\rho_{\mathrm{gas}}}-1\right)e^{E_{\mathrm{B}}/RT}\right)}\right] \tag{19}$$

And in the high-density limit where ρ_{gas} goes to $\rho_{\mathrm{film,sat}}$

$$\frac{dG_{\mathrm{ex}}}{d\rho_{\mathrm{gas}}} = -2a\left(1-e^{E_{\mathrm{B}}/RT}\right)\left[\frac{1}{\rho_{\mathrm{film,sat}}}\right] = -V_{\mathrm{film}} \tag{20}$$

This will be used later in **section 5.2** to approximate the film volume at higher temperatures.

1.4 Packing Fraction

Packing fraction is a measure of how effectively material can be packed into a container. The packing fraction of 0.64, is that of random close packed (RCP) spheres [59]. The largest theoretical packing fraction is 1.

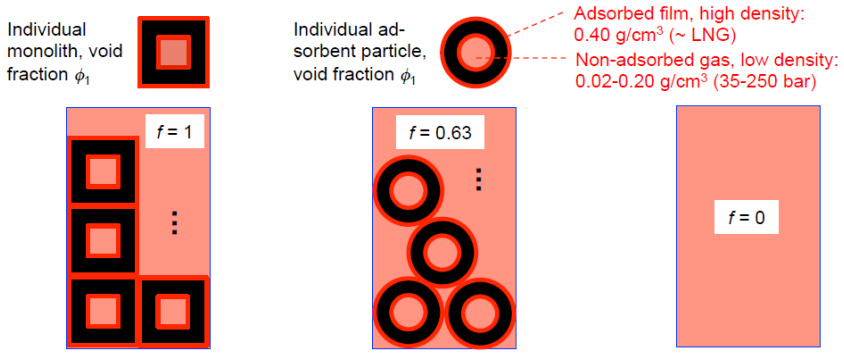

Figure 6. An illustration of different types of material packing. *Left*: The type of packing that monoliths could theoretically achieve for a packing fraction of 1 *Middle:* Packing of RCP spheres, which have inter-particle spacing. *Right:* A container with no adsorbent material i.e. compressed gas.

The packing fraction can be calculated using the porosities of the tank and the crystal. A way the packing fraction, f, can be related to these two different porosities is by [60]

$$\phi_{\text{tank}} = (1 - f) + f\phi_{\text{cryst}} \tag{21}$$

In this relation, if the packing fraction is 1, then

$$\phi_{\text{tank}} = \phi_{\text{cryst}} \tag{22}$$

Recall Eq (5) and Eq (6)

$$\frac{V_{\text{pore}} + V_{\text{inter granular}}}{V_{\text{pore}} + V_{\text{skel}} + V_{\text{inter granular}}} = \frac{V_{\text{pore}}}{V_{\text{pore}} + V_{\text{skel}}} \tag{23}$$

Cross multiplying and cancelling terms we arrive at

$$V_{\text{skel}} V_{\text{inter granular}} = 0 \tag{24}$$

and since V_{skeletal} cannot be zero so long as there is sample in the tank, $V_{\text{inter granular}}$ must be equal to zero. This is precisely what the left graphic on **Figure 6** represents, complete packing with no inter-particle spacing. Eq (21) can now be solved for the packing fraction

$$f = \frac{1 - \phi_{\text{tank}}}{1 - \phi_{\text{cryst}}} \tag{25}$$

It can also be shown that the packing fraction can be expressed in terms of two bulk densities

$$\rho_{\text{bulk,f}} = \frac{m_{\text{s}}}{V_{\text{tank}}} \tag{26}$$

and

$$\rho_{\text{bulk,1}} = \left(1 - \phi_{\text{cryst}}\right) \rho_{\text{skel}} \tag{27}$$

Where $\rho_{\text{bulk,f}}$ is the bulk density of the entire bed or tank and $\rho_{\text{bulk,1}}$ is the bulk density for an individual envelope or particle. Furthermore

$$f = \frac{\rho_{\text{bulk,f}}}{\rho_{\text{bulk,1}}} \tag{28}$$

Equating Eq (25) and Eq (28) one gets

$$f = \frac{1 - \phi_{\text{tank}}}{1 - \phi_{\text{cryst}}} = \frac{\left(\frac{m_s}{V_{\text{tank}}}\right)}{\left(1 - \phi_{\text{cryst}}\right)\rho_{\text{skel}}} \tag{29}$$

After cancelling terms and solving for the bed porosity we arrive at

$$\phi_{\text{tank}} = 1 - \frac{m_{\text{sorbent}}}{\rho_{\text{skel}} V_{\text{tank}}} \tag{30}$$

With this equation, the porosity of any given bed or tank can be determined using the mass of sample, the total volume of the tank, and the skeletal density of the sample. From there, one can determine the packing fraction with this tank porosity and the crystalline porosity of the sample through Eq (30).

2 Synthesis and Characterization of Monolithic Activated Carbon

Powdered activated carbon (PAC) works very well as an adsorbent material. However, there are practical limitations to PAC. The loose particles are a challenge to keep in the tank despite packing the powder incredibly tight. Furthermore, the tight packing limits the flow and diffusion of hydrogen through the adsorbent bed.

On the other hand, discrete pieces of bound powder, known as monoliths, aid tremendously in terms of the flow restriction. They can also be machined to allow heat to transfer much more easily.

The monoliths used in this work were created from a commercially available precursor powdered activated carbon (PAC), MWV-0260 (MeadWestVaco). The chemical activation involved

metallic potassium from KOH, the activating agent, intercalates between graphitic sheets, causing micropore formation [19,61]. The larger pores are the result of dehydration of KOH to K_2O which reacts with CO to form potassium carbonate [19,51]. Washing of the carbon after activation removes the intercalated potassium, potassium carbonate. Carbonaceous adsorbent materials were chosen for this work because, unlike MOFs, they maintain their high storage capacities while withstanding extreme mechanical stress [62]. The precursor PAC was mixed using a rock tumbler with the binder (polyvinylidene choloride-co-vinyl chloride) (PVDC) in a 0.5:1 binder to PAC ratio. Then 0.5 kg of the mixture was placed inside a cylindrical steel die at 27 °C in 0.1 kg increments where a 760 bar compressive stress was applied after each addition. The monoliths were then heated to 305 °C under stress before being allowed to cool for 16 hours while maintaining the mechanical stress. These carbon monoliths were pyrolized at 700 °C for 1.5 hours under nitrogen prior to measurements. This work was done on 2.86 kg of these carbon monoliths and using BR-0311 as a representative monolith sample. BR-0311 was produced in an incredibly consistent procedure and achieved consistent performance.

2.1 Production of PAC

The powdered activated carbon precursor (we named MWV-0260) was produced by MeadWestVaco (MWV) as described elsewhere (U.S Patents 5,416,056 [63] and 5,965,483 [64]). A two-stage activation process was conducted using wood sawdust as the starting material. In this work, the second stage activation was conducted on one of MeadWestVaco's wood-based activated carbon commercial products, Nuchar™ WV-A 1100.

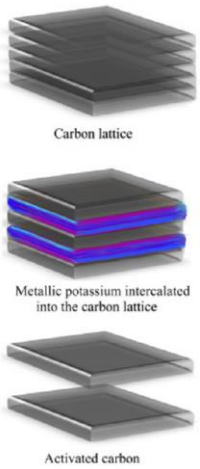

Figure 7. Depiction of the synthesis of our samples.

Preparation of Nuchar^{TM} WV-A 1100 can be found elsewhere (U.S. Patent RE31,093 [65,66]). The second activation was completed by mixing a 60 wt.% potassium hydroxide solution with Nuchar^{TM} WV-A 1100 at a KOH/carbon ratio of 2:1 (dry weight basis). The mixture was heated in a rotary kiln to a temperature of 840 ^{o}C. The alkali laden product was water washed at 80 ^{o}C until the eluent had a pH of 7.5. The wet activated carbon was dried at 110 ^{o}C (Note, this paragraph's content was provided primarily by Billy-Paul Holbrook from MWV).

2.2 Production of Monoliths

The monoliths were produced in batches by mixing MWV-0260 PAC with the binder, polyvinylidene chloride-co-vinyl chloride resin (PVDC), partially thermally decomposing the binder while subjecting the mixture to compressive stress, and carbonizing the resultant green body under nitrogen flow. This production process demonstrated a space time yield (kg of monolith produced per volume of reaction mixture per unit time) of 300 kg/m^3/day. PAC was mixed with the binder with a 0.5:1 binder: carbon mass ratio in rock tumblers for a minimum of 7 hours using 0.635 cm ball bearings.

Figure 8. The die used in the production of monoliths. *Left*: The die assembly. *Right:* An example of one of the finished monoliths that was machined to use in a different tank in our lab.

500 grams of mixture were placed inside a 8.89 cm ID, steel, cylindrical die (see **Figure 8**) at ~27 ^{o}C in 100 gram increments with 760 bar of compressive stress applied by a 45 metric ton press after each increment. The temperature of the die was increased 3 ^{o}C/min until it reached 305 ^{o}C while pressure was maintained for 90 minutes. The die was allowed to cool for ~16 hours while mechanical stress was maintained. Multiple green bodies were produced in parallel by maintaining the stress in multiple dies with the screws shown in **Figure 8**.

After removal from the die, the green bodies were carbonized under nitrogen flow in a quartz tube sealed with PTFE end flanges containing FKM O-rings. The tube was heated at 2 ^{o}C/min until it reached 700 ^{o}C where the temperature was maintained for 90 minutes before cooling naturally. The potentially harmful products (HCl and the salts formed by its reaction with steel) were captured in a series of traps (0 ^{o}C, soda lime, and -78.5 ^{o}C). The size of the compaction die was chosen to produce monoliths slightly smaller in diameter than the tank (see **Figure 8**). The procedure results in remarkably consistent samples; further detail about the production and

characterization of the monoliths can be found in the work by Rash *et al*. [42] or in U.S patent numbers 8,691,177 [67] and 8,926,932 [68].

2.3 Characterization of the Monoliths

Subcritical nitrogen isotherms on MWV-0260 and BR-0311 were measured using a Quantachrome Autosorb-1. The Brunauer-Emmett-Teller (BET) [69] surface areas were measured using a pressure range of 0.03 – 0.1 P/P_0. The cumulative pore volumes were measured at 0.995 P/P_0 by assuming liquid densities within the pores. The pore volume only includes void volume within individual grains and does not include intergranular void space. The skeletal densities were measured with helium pycnometry. These ρ_{skel} fall within the typical range of values for amorphous carbon (1.8 - 2.1 g/cm^3) [19]. The void fraction or porosity is determined by

$$\phi = \left(1 + \left(\rho_{\mathrm{skel}} V_{\mathrm{pore}}\right)^{-1}\right)^{-1} \tag{31}$$

Σ_{BET}, ϕ, V_{pore}, and ρ_{skel} for twelve samples are reported in **Table 2**. Pore size distributions (PSD) were calculated using quenched solid-state density functional theory (QSDFT) [70–74] assuming slit shaped pores, see **Figure 9**. It has also been shown that inelastic neutron scattering can be valuable as a complimentary sub-nanometer characterization technique [75,76].

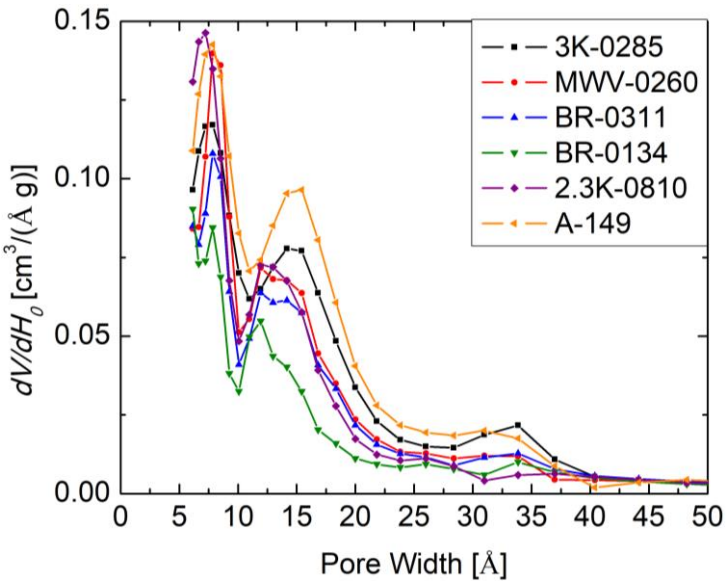

Figure 9. Pore size distribution for six various sample, calculated using QSDFT, assuming slit shaped pores.

The PSDs for both MWV-0260 (powder precursor) and BR-0311(formed monoliths) exhibit consistent features. There is an overall reduction from the monolith production process. Some pores were likely clogged with the binder or crushed from the intense mechanical stress. Surface areas and pore volumes can also be reduced from doping the material with other elements such as Boron [77]. The varying pore widths correspond to varying deepness of the potential wells [8,19,78], see **Figure 10**; narrower pores where the van der Waals potential of each side of the pore overlap are deep, wider pores have shallower potentials. Numerical simulations involving ensemble averages of different pore sizes weighted by the experimental PSD's show this view to be reasonable [79], that narrower pores predominantly adsorb the gases at lower coverage, and that wider pores become more important once the deeper narrow pores are saturated.

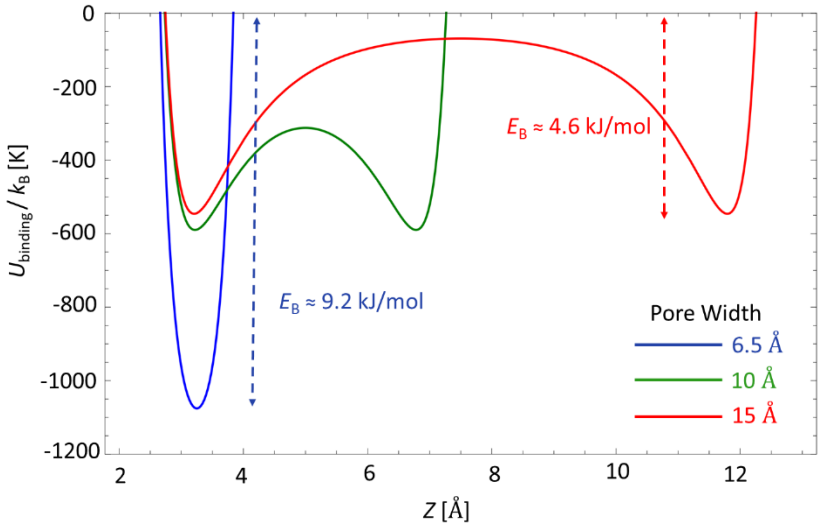

Figure 10. Laterally averaged potential energy for hydrogen in slit shaped pores. Binding energy is largest in narrow pores due to the combined adsorption potentials from both sides of the pore.

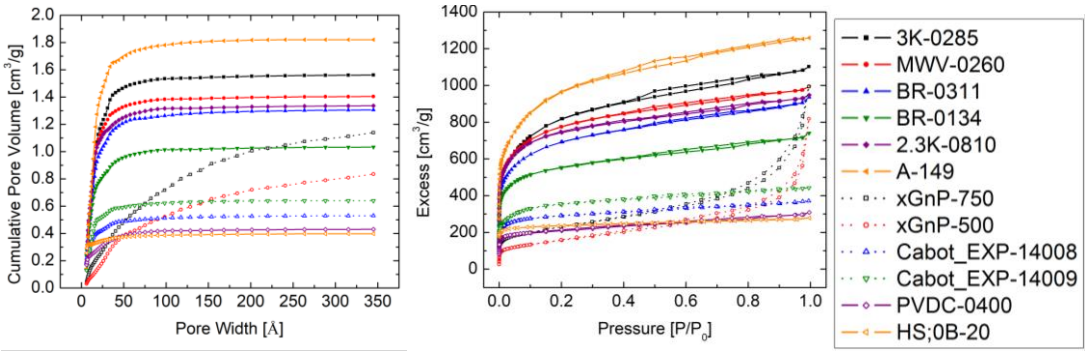

Figure 11. Autosorb measurements on 12 samples. *Left*: Cumulative pore volume. *Right:* Nitrogen adsorption isotherms.

The Autosorb can measure the pore volume of adsorbents. The cumulative pore volume shows that the vast majority of volume is in the sub-50 angstrom pore range. The volume does increase slowly until it reaches the total of 1.45 mL/g. Nitrogen isotherms can also be measured on the Autosorb. **Figure 11** shows the low-pressure regime of the adsorption curve. In the adsorption community, it is common to not differentiate between excess and absolute adsorption, because the difference for nitrogen is negligible.

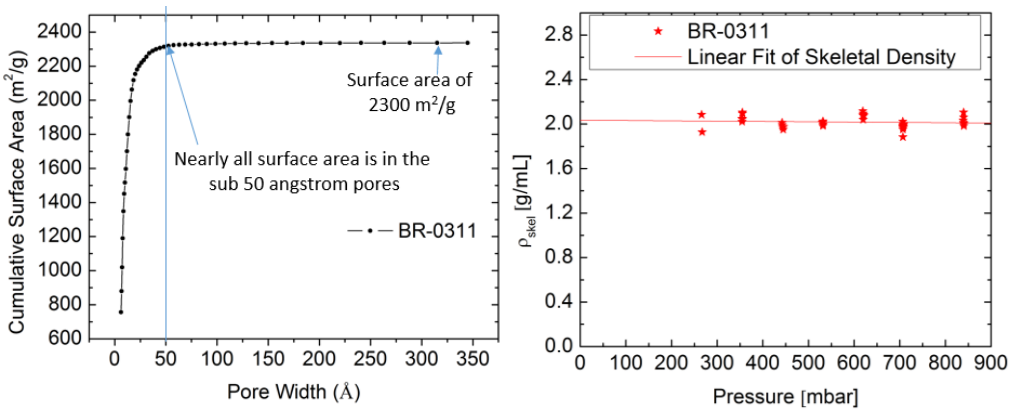

Figure 12. Cumulative surface area and helium pycnometry of BR-0311.

The cumulative surface area increases sharply from the narrower pores. At about 50 Å, the cumulative surface area does not increase. The maximum cumulative surface area for BR-0311 is 2300 m^2/g.

The skeletal density of each sample can be determined with helium pycnometry. From the graph, the skeletal density of BR-0311 is 2.03 g/cm^3. The skeletal density also does not vary much if at all over different pressures. This is important because the skeletal density is a value that factors into many different metrics.

Table 2. Characterization of carbon samples, including: Σ_{BET}, ϕ, V_{pore}

Adsorbent	Σ_{BET} (m^2/g)	ϕ	V_{pore} (cm^3/g)
3K-0285	2600	0.77	1.71
MWV-0260	2600	0.76	1.54
BR-0311	2300	0.74	1.45
BR-0134	2000	0.70	1.15
2.3K-0810	2600	0.77	1.47
A-149	3100	0.80	1.95
xGnP-750	760	0.76	1.54
xGnP-500	500	0.74	1.27
Cabot_EXP-14008	1100	0.54	0.58
Cabot_EXP-14009	1200	0.58	0.69
PVDC-0400	780	0.49	0.48
HS;0B-20	940	0.46	0.43

Table 2 shows important parameters for characterizing adsorbent materials. MWV-0260 is the representative PAC that is examined in the following section. It has a BET surface area of 2600 m^2/g and n crystalline porosity of 0.76. BR-0311 sample is the representative monolith examined in later sections. It has a BET surface area of 2300 m^2/g and an envelope porosity of 0.74. Further detail about the production and characterization of the monoliths can be found in the work by Rash *et al*. [42] or in U.S patent numbers 8,691,177 [80] and 8,926,932 [81].

3 10.6-Liter Hydrogen Storage System

Our 10.6 Liter hydrogen storage system (10LSS) allows us to measure storage capacity and dynamic behavior of our adsorbent material. The 10LSS consists of two 5.3 L modular tanks. Both tanks are identical, thus their behavior is similar. Increasing the number of modules would then increase the total storage of the system. Each of the two 5.3 L tanks can be filled with kilograms of adsorbent material (PAC or monoliths). The tank rests in an insulated thermal reservoir to maintain constant temperature liquid baths. The baths also decrease the amount of time it takes for the tank

to reach thermal equilibrium. Both tanks were built with a safety factor of 10 to be operated at 100 bar.

The top inlet inside the tank is a 28 cm long and 0.635 cm OD tube with an inline two-micron filter. The tube allows hydrogen to flow unimpeded through the adsorbent bed. Hydrogen flowing through the bottom inlet flows through a stainless-steel porous disk. The system measures temperature with two thermocouples (range of -85℃ to 150℃ and precision of 0.1℃). One thermocouple is mounted on the top of the tank and extends inside the tank, the other measures the bath temperature. Each end of the tank has two O-rings to seal the tank. One O-ring wraps around the shaft of the end cap that is inserted into the tank. The second O-ring provides the primary seal, which is a face seal between the end of the cylinder and the inserted end cap. These inserted end caps are secured with large end cap nuts that can be torqued down, to provide a better seal. For room temperature measurements, both O-rings are made of silicone. The 10LSS measures pressure with two pressure transducers. Each transducer can measure pressure up to 200 bar with precision of 0.1 bar. One transducer is able to measure the supply side pressure, one measures the tank pressure. There is also a vacuum gauge in conjunction with a roughing pump that operates between 10^{-6} and 1 bar. The system also uses a heat exchanger to control the temperature of the hydrogen leaving the tank. This is important to ensure the flow meter is not affected by cold temperatures.

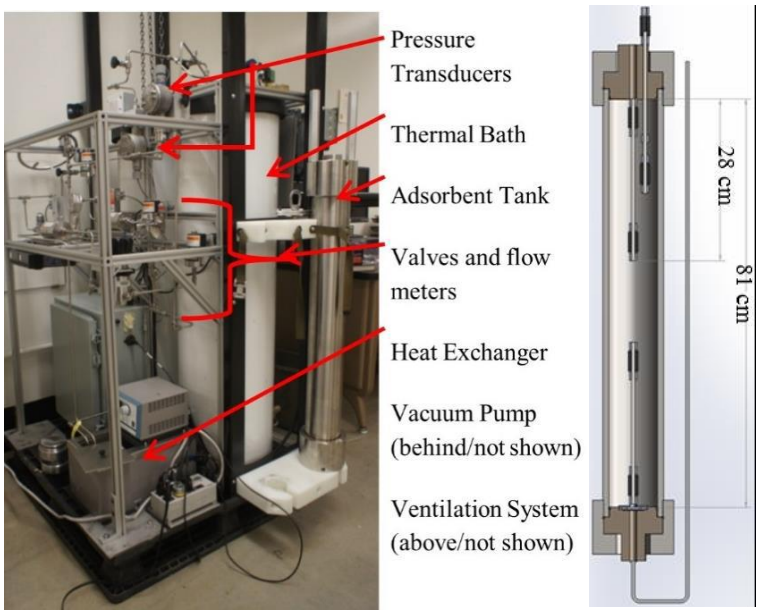

Figure 13. Picture of the 10LSS and labelled components and cross section of the tank.

Filling and discharging are monitored by two digital mass flow meters. The mass flow meter used for measuring discharges is coupled with a mass flow controller. A needle valve is used to control the fill flow rate. Both flow meters measure mass flow up to 36 g/min (random error of 0.5%), but are limited to 18 g/min to avoid overwhelming the system and vent.

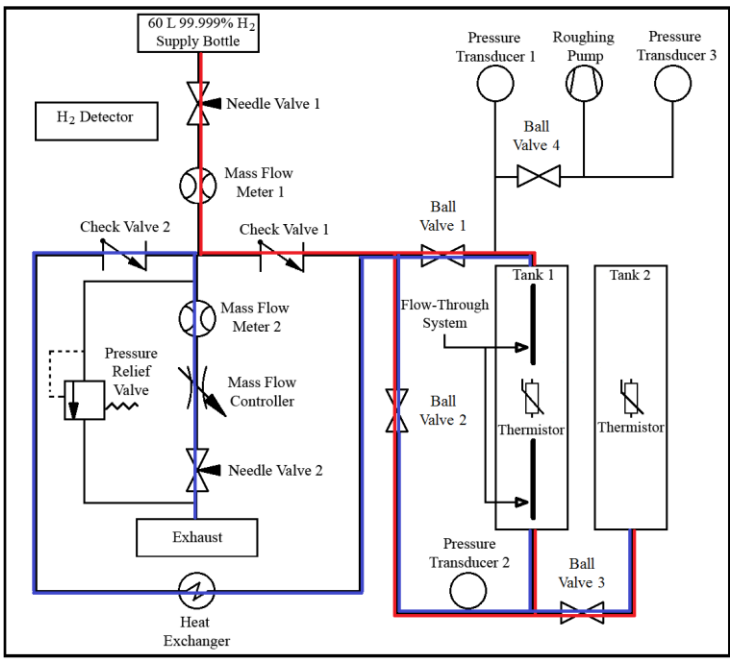

Figure 14. Schematic and flow diagram for the 10LSS. The red path is for filling the tank to measure adsorption. The blue line is for discharging the tank to measure desorption.

For measuring adsorption, flow is measured from mass flow meter 1 and controlled with needle valve 1. The gas is forced clockwise around the loop through two check valves. Opening ball valves 1 and 2 will allow flow into the primary tank. The pressure, temperature, and flow rate are recorded by LabView. The integral of the flow rate is numerically approximated to determine the cumulative amount of gas entering the system. For measuring desorption, needle valve 1 is closed and needle valve 2 is opened. Ball valves 1 and 2 are opened to flow out of the system and clockwise through the check valve loop. In the loop, gas flows through the heat exchanger so the gas temperature does not affect the measurement (below 0℃). Needle valve 2 is used with the flow controller to maintain a consistent flow rate. Prior to each adsorption measurement, the tank was heated to 120℃ and outgassed for 3.5 days.

Hydrogen discharged by the system is deposited into our labs exhaust system, which is driven by an explosion-proof blower. The exhaust combines hydrogen with a continuous air flow of 3000

g/min. If we discharge the tank at the maximum flow meter setting of 18 g/min, the hydrogen concentration in the exhaust is 0.86%. This is well below the lower explosive limit for hydrogen at room temperature of 4%.

A problem originally encountered with the PAC was the restricted flow of hydrogen. Due to packing so much powder so tightly, there was less room for the gas to travel between particles. This also created a pressure gradient which packed the powder even more. This also affected how quickly the tank could be filled and how it thermally equilibrates. The effect was greatest with a significant amount of gas in the system. That is why the 28 cm tubes are critical to allowing gas to be injected or removed from a location closer to the middle of the tank when using PAC.

One of the 5.3 L tanks was able to be packed with 1.5 kg of PAC. Using these values for our volume of the tank and mass of adsorbent, along with a skeletal density of 2 g/cm^3 we obtain a tank porosity of 0.86. The crystalline porosity for this PAC was measured to be 0.78. These two porosities yield a packing fraction of 0.636, which is for all practical purposes equivalent to the packing fraction of RCP spheres.

One of the great benefits of our monolithic carbon is that they do not fill the whole internal volume of the tank in the same way powder does. Because the monoliths are discrete cylinders with slightly less diameter than the tank's inner diameter, gas can flow more easily around the sides and between individual monoliths. This helps the transfer of heat tremendously and the rigid monoliths do not pack tighter to impede flow.

When filling the tank with several monoliths, we could fit 2.86 kg of carbon into the 5.3 L tank. This leads to a bed porosity of 0.73.

Table 3. Porosity and packing fraction of monoliths in the 10LSS

Monolith Name	Mass (g)	Volume (cm^3)	Density (g/cm^3)	Porosity	Packing Fraction
BR-0626A	365.564	649.7	0.5627	0.719	0.96
BR-0626B	366.036	639.3	0.5726	0.714	0.94
BR-0627A	341.253	609.1	0.5602	0.72	0.96
BR-0627B	371.375	638.9	0.5813	0.709	0.93
BR-0630	374.744	661.3	0.5667	0.717	0.95
BR-0633	383.317	660.8	0.5801	0.71	0.93
BR-0634	375.141	662.1	0.5666	0.717	0.95
BR-0635	369.441	667.2	0.5537	0.723	0.98
BR-0640	367.316	652.5	0.5629	0.719	0.96
Average			0.5674	0.716	0.95
Standard Deviation			0.0091	0.005	0.02

Table 3 lists the mass and volume of each monolith used in the tank. Each monolith was measured macroscopically to determine each of their envelope porosities. The envelope porosity for each monolith was very consistent, which shows that our synthesis process was repeatable. The average of these porosities yields a packing fraction of 0.95. This is very close to perfect packing of material into our tank. Each of these monoliths are discrete pieces that are not in complete contact with all surfaces inside the tank. Thus, the remaining 5% can likely be attributed to the spacing between monoliths and the space between the tank walls and the monoliths.

4 Hydrogen Adsorption Measured with the 10LSS

Our gravimetric excess adsorption measurements were taken on two instruments. A large sample (2.86 kg) was measured with the 10LSS and a small sample (~300 mg) was measured on the commercially available Hiden HTP1-V.

Gravimetric excess adsorption is determined by measuring the total mass of hydrogen in the system, knowing the gas density inside the system from measuring the temperature and pressure[82], and

measuring or estimating the skeletal volume[8] of the adsorbent of the system[9]. The skeletal volume was determined here by using a measured skeletal density of 2 g/mL [39] and measuring the mass of carbon in the system.

Gravimetric and volumetric storage is determined by integrating the hydrogen flow rate measured with the mass flow meter and subtracting the gas that remains in ancillary pipes. The volume of gas in the pipes is determined by subtracting the volume of the empty tank from the volume of the empty system. The volume of each 5.3-L tank was provided by the tank manufacture and verified with a micrometer and tape measure. The volume was also verified from blank isotherms that were measured.

4.1 Room Temperature (296 K) Experimental Set Up

Prior to the room temperature measurement on the monoliths, there had been several slight alterations to the sealing grooves and the variation of O-rings used. Each of the tanks end caps have two locations for O-rings to seal the tank.The end cap pictured in **Figure 15** is the top end cap for the tank. The long thin rod is the thermocouple used to measure the internal temperature of the tank. The tube sticking through is the inlet through which the gas flows. The groove that the orange silicone O-ring rests in is described as the shaft groove and the empty groove is described as the face seal. The bottom end caps have the same groove geometry.

For the 1st room temperature isotherm on the monoliths, the O-rings on the top end cap were changed from the ones used for the PAC measurements. The shaft seal used a thicker silicone O-ring in order to apply more compression between the tank wall and the groove on the end cap. The face seal was replaced by a larger diameter silicone O-ring so the O-ring would not be stretched as much.

Figure 15. Tank being outgassed with heating jackets and top end cap with silicone O-ring around the shaft groove and no O-ring on the face seal.

The tank was outgassed with 3 of our heating jackets with no temperature controller (**Figure 15**). The tank stood vertically with the jackets wrapped around the tank, stacked from the bottom. The tank reached an internal temperature of 160℃ for 2 days. When the tank was tested for a room temperature isotherm, a small leak occurred at 50 bar and grew larger with increased pressure. This leads to larger measured excess adsorption due to extra mass entered into the system. The leak seemed to be a result of the amount of heat applied during outgassing and this heat being localized to the bottom of the tank near one of the seals.

For the second room temperature isotherm, the shaft O-rings for both top and bottom of the tank returned to original, less thick, silicone O-rings. Both face seals used the larger diameter, non-stretched, silicone O-rings. The tank was outgassed at 120℃ for 18 hours. The outgassing was accomplished by suspending just one of the heating jackets mid-way up the tank and allowing the heat to radiate from that spot. This was all to ensure the O-rings would not be damaged from excess heat. All room temperature isotherms including blanks were conducted in a water bath to achieve

faster and more stable thermal equilibrium. After outgassing, the tank was placed in the water bath and allowed to cool to room temperature overnight. The lines were filled to our target pressure of 145 psi for the first data point. Then the tank was opened and filled to 145 psi at a rate of 3 g/min while the mass flow meter integrated the mass of gas passing through. The tank was overfilled by about 5 psi for the first point (more for higher pressures) so that when the tank equilibrated it would rest at 145 psi.

4.2 273 K Experimental Set Up

The O-rings remained the same as they were for the second room temperature isotherm. The tank was outgassed at 120℃ for 18 hours using the same method for wrapping the tank. The tank was then lowered into the bath reservoir and ice was added around the tank. The ice was continually replenished as it melted while the tank cooled. It was allowed to cool overnight down to 0℃.

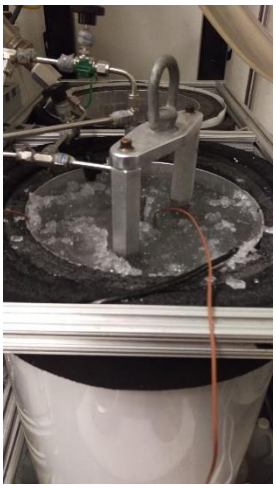

Figure 16. Tank in ice bath for the 273 K isotherm.

Then the tank was topped off with ice and filled with some water to a set mark on the tank's anchor piece (**Figure 16**). The isotherm measurement was done using the same gas dosing method as the 0℃ blank and the room temperature measurements. During the measurement, the bath level was constantly checked and ice was replenished as needed.

4.3 198 K Experimental Set Up

In order to measure an isotherm at 198 K, a dry ice and acetone bath was used. The original face sealing silicone O-rings were replaced with Teflon O-rings so the seal would not be compromised by the acetone. With these Teflon O-ring outer seal and silicone O-ring inner seal, we were able to measure the isotherm up to 50 bar.

Despite only measuring the isotherm up to 50 bar, the storage capabilities are in line with the small scale measurement on the Hiden instrument. The fact that we were able to seal and cool such a large tank and get accurate results is very encouraging. However, pressurizing beyond 50 bar caused the tank to leak. This has led us to investigate other methods for providing a seal.

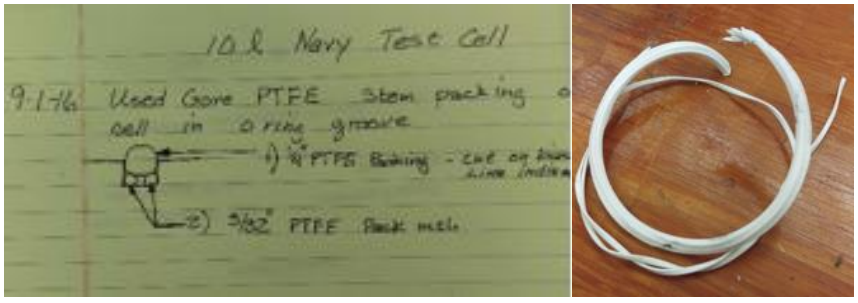

Figure 17. Teflon tape for use as a sealant. *Left*: Schematic drawing of how to fill the groove with the tape. *Right:* Teflon tape after being used in the tank.

The next attempt we used PTFE packing material (we referred to it as Teflon tape). The idea was to fill the face sealing groove with 10% extra material to apply enough compression (Figure 17). This Teflon tape was fairly malleable and it flattened out a bit, however the discrete pieces of material did not form a uniform seal together. The more widely used method for sealing vessels with this material is to apply it to the interface of two flat surfaces that will be in contact. Then apparently the material is completely flattened and provides an adequate seal.

Another attempt was made with Flexiseal O-rings from Parker. These O-rings are specifically designed to handle low temperature and high pressure. They have a Teflon exterior in the shape of a U or a V and have a spring inside the crevasse. These O-rings utilize the spring to apply extra compression to the sealing faces. The geometry of the O-rings also direct the increasing pressure on the inside of the tank along the inside of the U or V to apply even more compression to each face. Despite these promising attributes, the Flexiseal O-rings also failed to seal past 50 bar. The more common (and more expensive) solution that could possibly seal the tank would be indium O-rings. The indium comes in a wire type form and can be wound around in the groove with added material, similar to what we attempted to do with the Teflon tape. The indium is much more malleable and should actually form into a uniform piece when sealing the tank. Otherwise, fairly major redesigns to the tank would need to occur.

4.4 Isotherm Results and Discussion

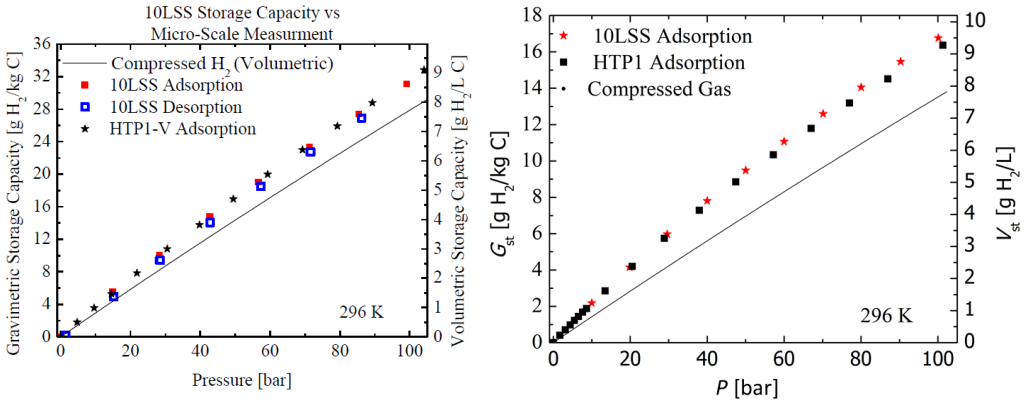

Figure 18. Storage capacity agreement between 10LSS and Hiden instruments with PAC and monoliths. *Left*: The PAC is in agreement within 1% at all pressures. *Right:* The monolith is in agreement within 2%.

Gravimetric and volumetric storage capacity values measured on the kilogram scale system (10LSS) agree within 1% to the values measured on the milligram scale system (Hiden) across all pressures. This demonstrates that despite the amorphous structure of these carbon samples, they are scalable (by a factor of 10,000) and provide consistent structural and storage performance results [44]. Gravimetric and volumetric storage capacities on the Hiden were determined using excess adsorption and the measured bulk density of PAC in the 10LSS (0.28 kg/L). This measured bulk density corresponds to a packing fraction of 0.63, which is reflective of the packing of random close packed spheres [59]. Further detail about the 10LSS can be found in our previous work [83] and the work done by Rash *et al* [42].

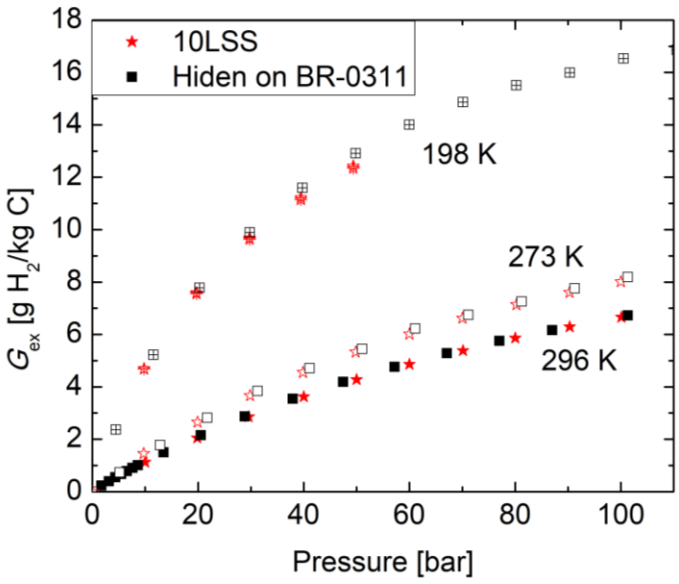

Figure 19. Gravimetric excess instrument agreement at all three measured isotherms.

The graph above contains the first several isotherms measured on the 10LSS with the carbon monoliths. They were measurements taken at 23℃, 0℃ , and -80℃. The -80℃ data for the 10LSS stops at 50 bar due to a leak occurring. Comparing gravimetric excess adsorption data measured on the 10LSS with data measured on the Hiden HTP1-V demonstrates that they are in very close agreement. One of the perks of using excess adsorption is that no assumptions on the packing fraction need to made. These experiments demonstrate that the 10LSS can accurately measure the total mass of hydrogen with the flow meters. This indicates that filling and discharging rates of the system can also be accurately measured. In our analysis, in order to mitigate uncertainties [39], we ensured all instruments were well calibrated and leak proof, samples were outgassed and thermally controlled, ultra-purified hydrogen gas was used. The extremely large sample size aided in reducing the relative error of our excess adsorption measurements.

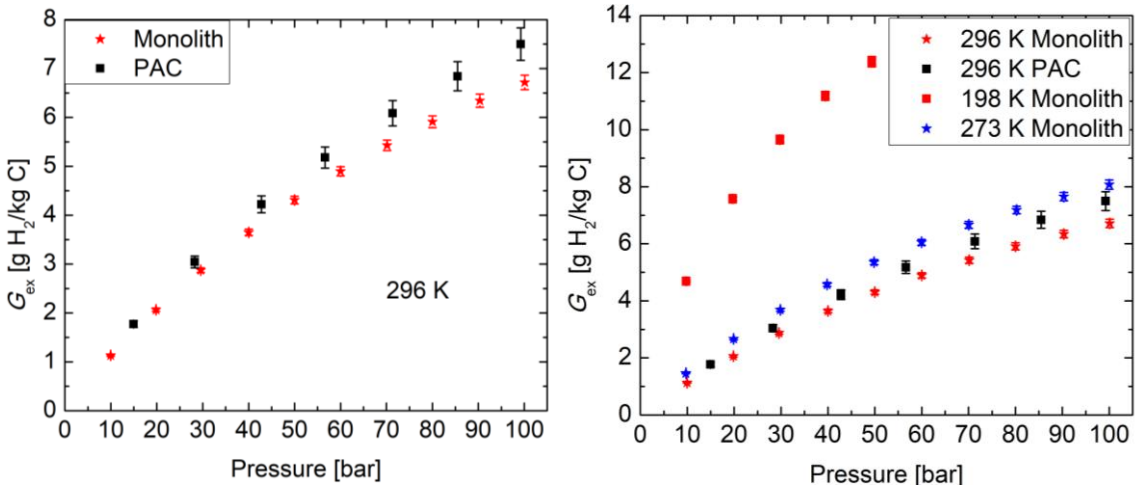

Figure 20. Gravimetric excess adsorption comparisons. *Left*: Monolith vs PAC at room temperature. *Right:* All isotherms measured on the 10LSS.

The left graph shows the excess adsorption of the carbon monoliths and PAC at room temperature are compared. The PAC does have greater excess adsorption at higher pressures (7.5 g/kg at 99.2 bar vs 6.7 g/kg at 100.1 bar). **Figure 20** compares all measurements on the 10LSS. The 0℃ measurement does outperform both room temperature PAC and monoliths, which is to be expected. The -78℃ measurement does significantly increase the excess adsorption, despite the measurement not being completed to 100 bar.

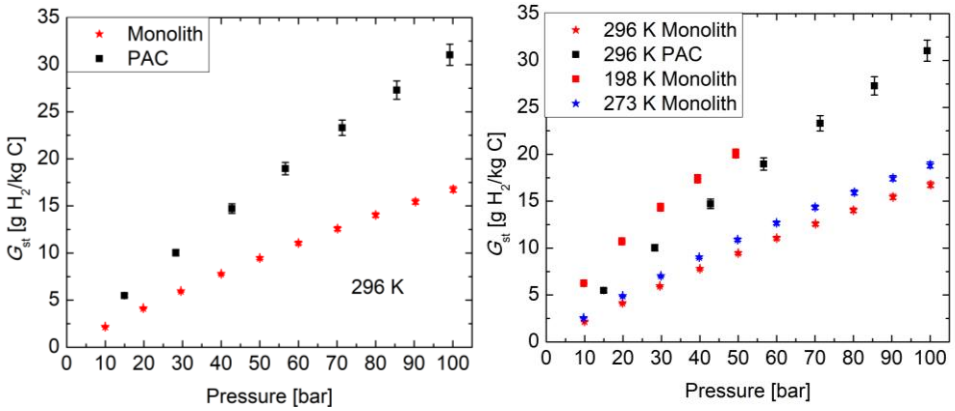

Figure 21. 10LSS gravimetric storage capacity comparisons. *Left*: Monolith vs PAC at room temperature. *Right:* All isotherms measured on 10LSS.

Figure 21 shows that the PAC has larger gravimetric storage capacity at room temperature. On the right it is even competitive with -78℃ on the monoliths.

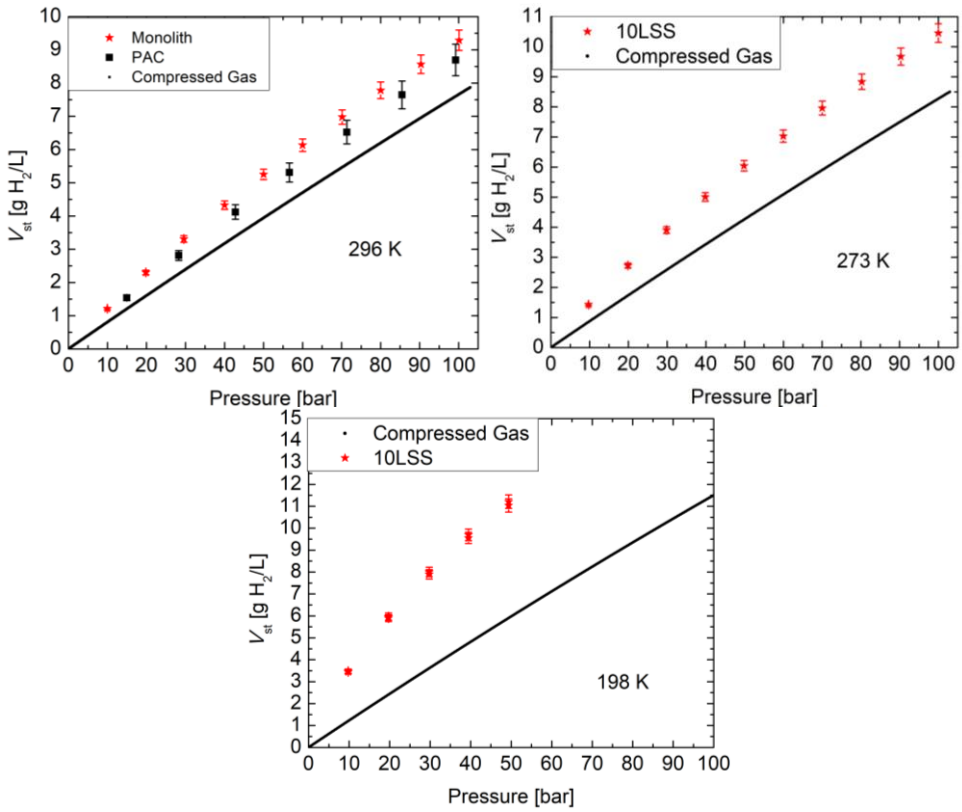

Figure 22. 10LSS volumetric storage capacity comparisons with compressed gas. *Left*: 296 K monolith vs compressed gas. *Right:* 273 K monolith and PAC vs compressed gas. *Bottom:* 198 K monolith vs compressed gas.

On the left, both PAC and monoliths are plotted with the storage capacity of compressed gas. At room temperature the PAC and monoliths outperform compressed gas at 100 bar by 114% and 119%, respectively. The percent increase over compressed gas is larger at 50 bar (118% and 131%). The graph on the right is storage for the monoliths at 0℃. The percent increase over compressed gas for 100 bar and 50 bar are 124 % and 140%, respectively. For the monoliths at -78℃ and 50 bar, the storage increase is 185%.

Table 4. Summary of equilibrium storage data at 100 bar. G_{st} and V_{st} were calculated from G_{ex}, ρ_{skel}, ϕ and Eqs. (7,8). G_{ex} values were from Eq. (2) and tank data, for PAC at 296 K, Monolith at 296 K, and Monolith 273 K. For Monolith 198 K, G_{ex} was determined with manometric data measured on the Hiden instrument because the tank data ends at 50 bar.

Adsorbent Temperature (K)	Σ_{BET} (m^2/g)	ϕ (tank)	G_{ex} (g/kg)	G_{st} (g/kg)	V_{st} (g/L)	Mass H_2 stored (g)	Ratio V_{st}/ρ_{gas}
PAC 296	2600	0.86	7.5	31	8.7	46	1.1
Monolith 296	2300	0.73	6.6	17	9.2	49	1.2
Monolith 273	2300	0.73	8.0	19	10.4	55	1.3
Monolith 198	2300	0.73	16.6	32	17	93	1.5

Table 4 provides a good summary of all of the different storage metrics used. To determine the total mass of hydrogen in our tank, the volumetric storage capacity was multiplied by the volume of our tank (5.3-L). As for the compressed gas mass, the gas density at the given pressure and temperature was multiplied by the volume of our tank.

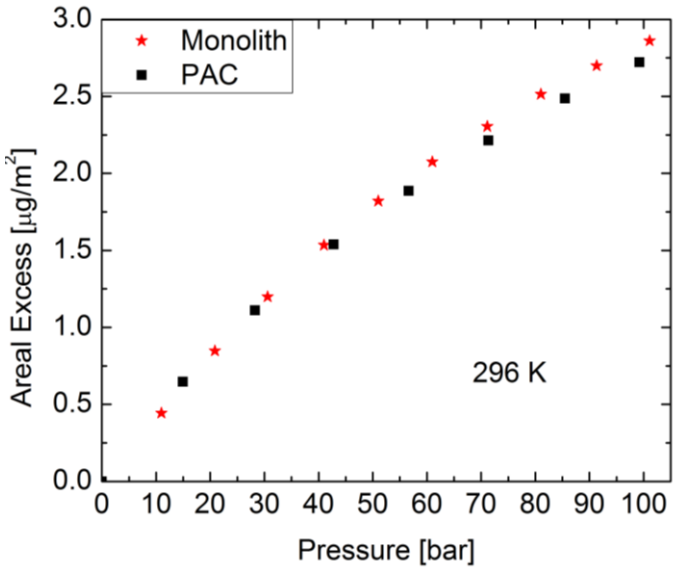

Figure 23. Areal excess adsorption for monoliths and PAC, at room temperature.

While the PAC had slightly larger excess adsorption than the monoliths, this is largely due to PAC's larger specific surface area (more adsorption sites). Areal excess is a metric that normalizes the excess adsorption to the specific surface area (2600 m^2/g for PAC and 2300 m^2/g for monolith). Converting to areal excess demonstrates that there is not much of a difference between the true performances of the two samples. The monolith actually performs slightly better, but not much outside uncertainty.

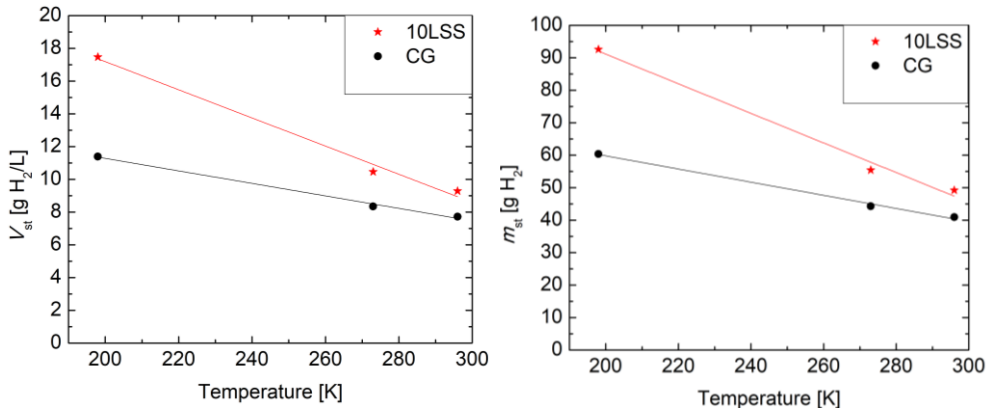

Figure 24. Increase in storage with decreasing temperature. *Left*: Volumetric storage capacity of the monoliths compared to gas density. *Right:* Mass of hydrogen stored with the monoliths compared to compressed gas.

Figure 24 demonstrates that the storage capacity measured on the 10LSS increases roughly linearly (R^2= 0.9824) with decreasing temperature in this temperature regime. The rate of this increase in mass stored is also more than two times greater than the rate of increase in compressed gas (0.45 g/K and 0.20 g/K).

5 Determination of Saturated Film Densities and Volumes for Adsorbed Hydrogen, and Application to the Calculation of the Enthalpy of Adsorption at Room Temperature

The enthalpy of adsorption ΔH of a gas onto a surface is one of the most important characteristics of the process; its value along with the specific surface area determine the overall performance of the material for storage or gas separation. Normally, the determination of ΔH for hydrogen is challenging. A common approach is to apply the Clausius-Clapeyron equation [9] to two isotherms at close temperatures. A difficulty is that whereas experimentally the excess adsorption is obtained, it is the absolute adsorption that needs to be used for this determination [52]; the relationship between absolute and excess adsorption requires knowing the volume of the adsorbed film, which is normally not available. In addition, cryogenic adsorption isotherms have obvious technical complications (e.g., well-controlled refrigeration/cryostats) and careful calibration (e.g., cold vs. hot volumes) [84]. In this section, we will show how to determine the film volumes and densities, and use these results to calculate the enthalpy of adsorption at cryogenic and room temperatures. We show that once the saturated film density $\rho_{\text{film,sat}}$ is determined, it is a characteristic of the gas (not the adsorbent, or temperature). The knowledge of $\rho_{\text{film,sat}}$ then permits us to fit a full Ono-Kondo [21,22] adsorption curve for any material even at high temperatures to determine the adsorbed film volume, and thus the absolute adsorption curves and enthalpy of adsorption.

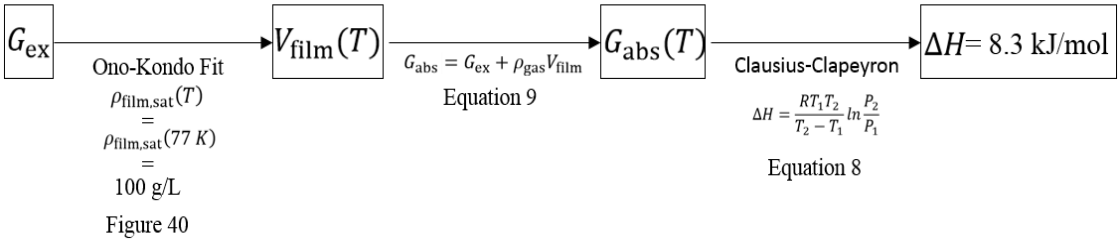

Figure 25. Summary of the procedure used to determine the isosteric heat from 23 ºC and 0 ºC isothermal data measured on the 10LSS.

5.1 Cryogenic Determination of Adsorbed Film Densities and Volumes

As discussed above, it is necessary to determine the saturated adsorbed film volume and saturated film densities. In this section we show that the cryogenic determinations of the adsorbed film density are not significantly temperature dependent and may be applied even at room temperatures.

Figures 4 and **5** show gravimetric excess adsorption isotherms measured using the Hiden HTP1-V instrument. This instrument, while only capable of using samples up to 1 cm^3, can span a broader range of temperatures (77-400 K) and pressures (0-200 bar) than the 10LSS. This capability allows it to reach the high gas density regime, where the adsorbed film becomes saturated and the excess adsorption isotherms exhibit a linear decay with the gas density. **Figure 26 (a)** shows adsorption isotherms for a variety of activated carbons including powders, monoliths and polymer-based at 77 K. Donhke *et al*. [58] have shown that, in this regime, the saturated adsorbed film volume is given by the slope $V_{\text{film}} = dG_{\text{ex}}/d\rho_{\text{gas}}$, whereas the extrapolation to where the line crosses the abscissa ($G_{\text{ex}} = 0$) provides a good estimate for the saturated film density, $\rho_{\text{film,sat}}$. It is remarkable that in all samples, the estimation of $\rho_{\text{film,sat}}$ (97-107 g/L) is higher than that of liquid H_2 (71 g/L) and is quite independent of the sample specific surface area, see **Figure 26 (b)** [40,46,58]. Additionally, the almost linear relation between V_{film} and specific surface area, in **Figure 26 (c)**, indicate a common film thickness $t_{\text{film}} = V_{\text{film}}/\Sigma_{\text{BET}} \approx 3$ Å. Remarkably, significantly lower than the typical pore sizes > 7 Å. It is also remarkable that across a wide range of temperatures (77-173 K), the estimation of $\rho_{\text{film,sat}}$ (100-112 g/L) on BR-0311 is also higher than that of liquid H_2 (71 g/L) and is quite independent of temperature, see **Figure 27** and **Figure 28 (b)** [40,58]. Additionally, V_{film} tends to decrease with increasing temperature, see **Figure 27** and **Figure 28 (c)**. It has also been shown that V_{film} for methane continues to decrease at higher temperatures [85].

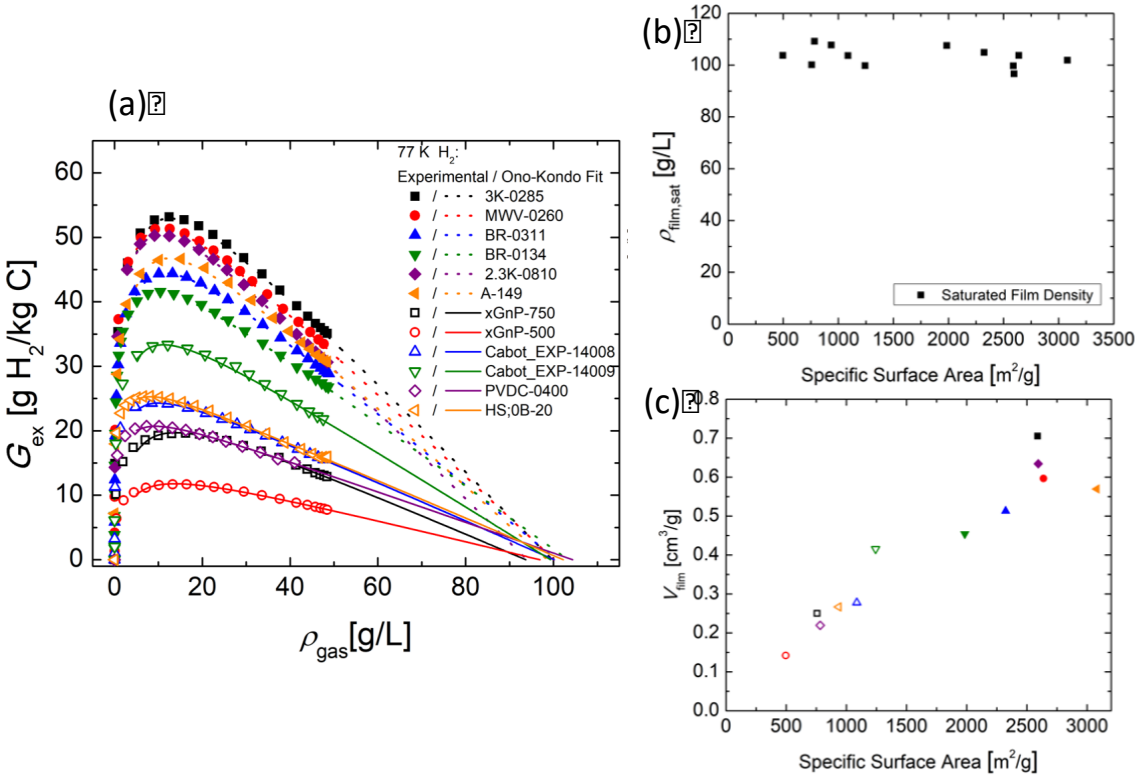

Figure 26. Cryogenic Hiden isotherm measurements on a wide variety of samples with Ono-Kondo fits. (a) G_{ex} vs ρ_{gas} at 77 K measured on the Hiden for a variety of samples. The better performing samples exhibit the linear regime to experimentally determine the V_{film} and $\rho_{film,sat}$. (b) $\rho_{film,sat}$ vs specific surface area, demonstrating no clear dependence. (c) V_{film} vs specific surface area, demonstrates a linear trend.

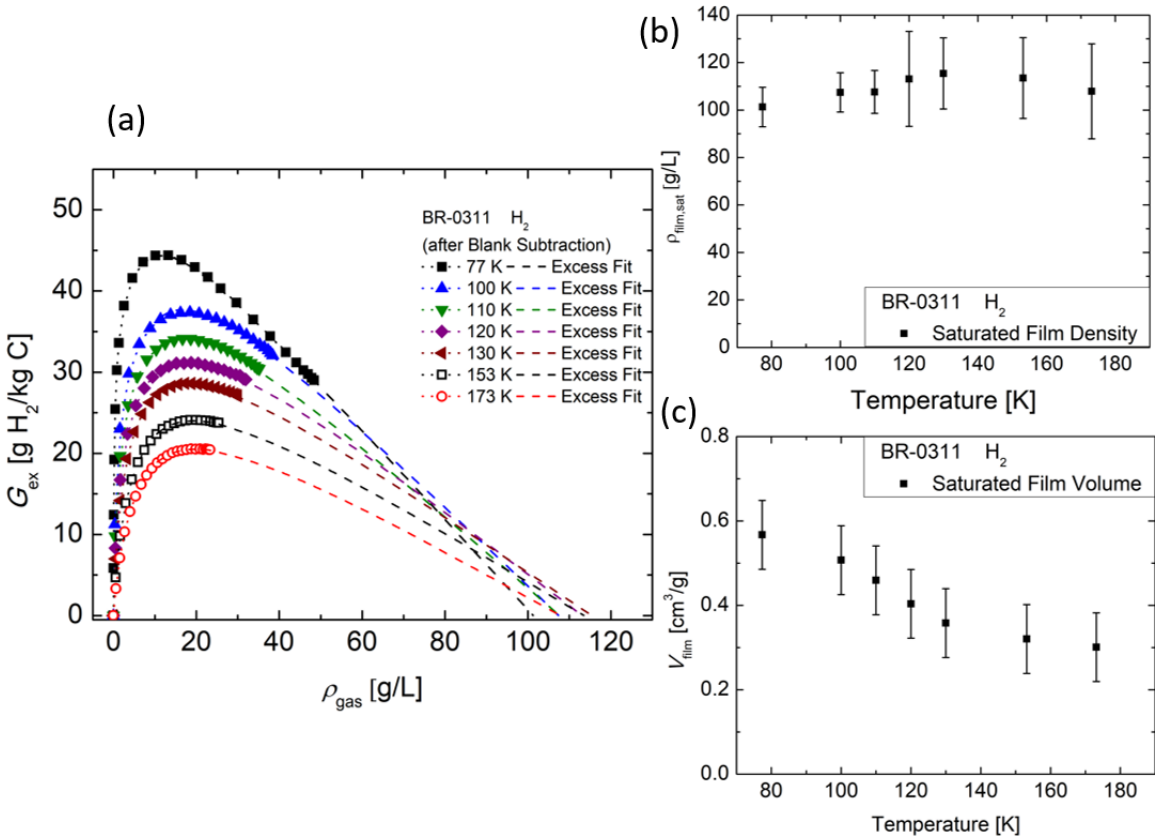

Figure 27. Cryogenic Hiden isotherm measurements on BR-0311 over a broad range of temperatures with Ono-Kondo fits. (a) G_{ex} vs ρ_{gas} measured on the Hiden for temperature range of 77-173 K. (b) $\rho_{film,sat}$ vs temperature, demonstrating no clear temperature dependence. (c) V_{film} vs temperature, demonstrates the decreasing V_{film} with increasing temperature.

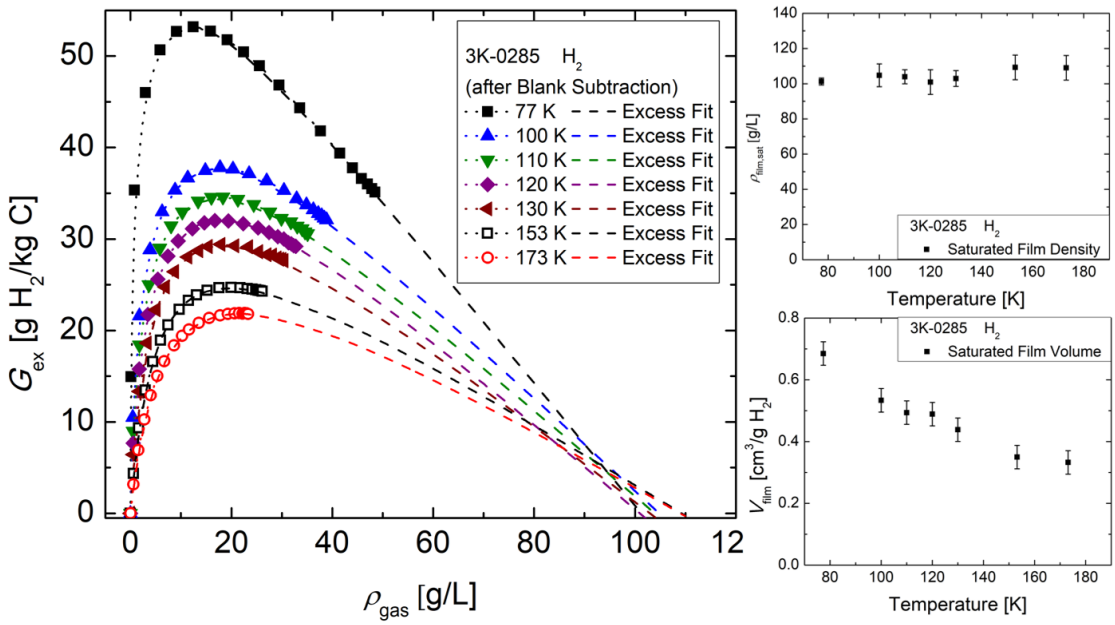

Figure 28. Cryogenic Hiden isotherm measurements on the PAC 3K-0285 over a broad range of temperatures with Ono-Kondo fits. (a) G_{ex} vs ρ_{gas} measured on the Hiden for temperature range of 77-173 K. (b) $\rho_{film,sat}$ vs temperature, demonstrating no clear temperature dependence. (c) V_{film} vs temperature, demonstrates the decreasing V_{film} with increasing temperature.

The fact that $\rho_{film,sat}$ is sample and temperature independent, makes it a property of the adsorbate gas, i.e., a cryogenic temperature determination in one particular sample would still be valid for almost any sample at almost any range of temperatures. This determination is quite useful for future developments. The reason for this robustness is that at saturation the film is so densely packed that the dominant effect is the hydrogen to hydrogen repulsion.

Conversely, V_{film} is surprisingly seen to decrease with increasing temperature. We speculate that the reason for this behavior is that at higher temperatures, the adsorption occurs only in the deepest binding sites, normally associated with narrower pores (whereas at lower temperatures the adsorbate gas would have access to more binding sites). **Figure 29** illustrates this idea: more pore sizes contribute to the overall V_{film} as temperature decreases.

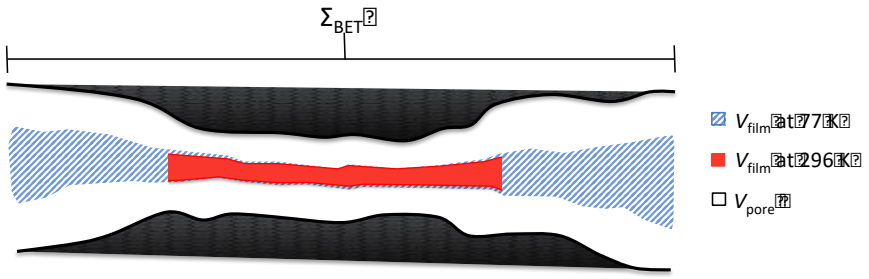

Figure 29. Illustration of the decrease of V_{film} with increase of temperature. At lower temperature narrow and wide pores contribute to the adsorption; at higher temperatures only the narrower pores do.

5.2 Room Temperature Determination of Adsorbed Film Volume Through the Application of the Ono-Kondo Adsorption Model

In **Sec. 5.1**, we observed how the linear decay of the excess adsorption isotherms at high gas densities results in a determination of film volumes. Unfortunately, at higher temperatures (~ 300 K), this extrapolation to large ρ_{gas} is not possible without going to extremely high pressures, as shown in **Figure 19** and **Figure 30** where no local maximum or decaying regime for G_{ex} is observed. Here, we use the Ono-Kondo adsorption model [21,22]

$$G_{ex} = 2a \frac{\left(1 - \frac{\rho_{gas}}{\rho_{film,sat}}\right)\left(1 - e^{E_B/RT}\right)}{1 + \left(\frac{\rho_{film,sat}}{\rho_{gas}} - 1\right)e^{E_B/RT}}, \tag{18}$$

to extrapolate to the high gas density, ρ_{gas} , regime, see **Figure 30** (where a is a scaling factor, $\rho_{film,sat}$ is the saturated adsorbed film density, E_B is the binding energy of the gas-solid interaction, and R is the ideal gas constant). It may appear unlikely that the relatively narrow range of ρ_{gas} accessible would yield a trustworthy fit. However, our observation that the saturation density $\rho_{film,sat}$ is quite robust (97 to 107 g/L for a wide variety of adsorbents at 77 K, **Figure 26 4 (b)**, 100 and 112 g/L for BR-0311 between 77 K and 173 K [40], **Figure 27 (b)**) adds one important

fixed point to the isotherm ($G_{\text{ex}}(\rho_{\text{film,sat}}) = 0$), see **Figure 30**. For the calculations that follow, we chose $\rho_{\text{film,sat}} = 100 \pm 20$ g/L. Calculating the slope of the Ono-Kondo fit in the high gas density regime then yields the volume of the adsorbed film V_{film} [86,87].

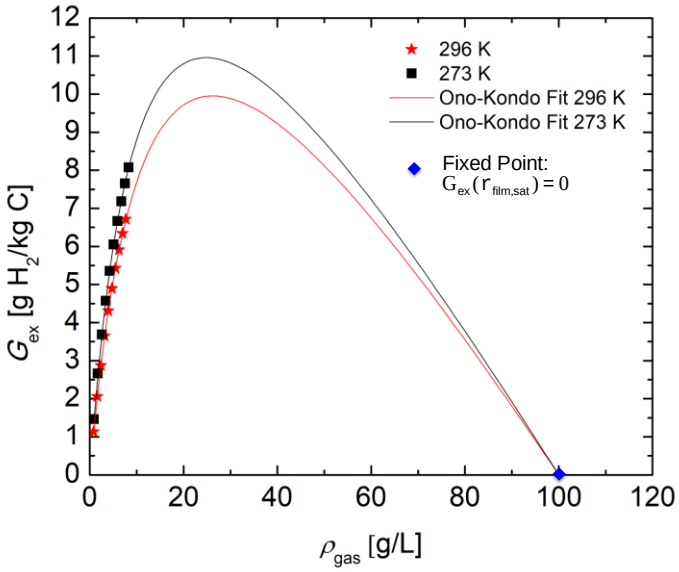

Figure 30. G_{ex} isotherms for 273 K and 296 K up to 100 bar on the 10LSS, with the accompanying Ono-Kondo fits using the fixed point $G_{\text{ex}}(\rho_{\text{film,sat}}) = 0$, with $\rho_{\text{film,sat}} = 100$ g/L.

Assuming that $\rho_{\text{film,sat}}$ = 100 g/L, results in an excellent fit to the data (R^2 = 0.9998) that shows a reasonable extrapolated local maximum and high gas density regime, see **Figure 30**. With the high-quality fit, V_{film} can be calculated from the slope of the high gas density regime

$$\frac{dG_{\text{ex}}}{d\rho_{\text{gas}}} = -2a\left(1 - e^{E_{\text{B}}/RT}\right)\left[\frac{1}{\rho_{\text{film,sat}}}\right] = -V_{\text{film}} \tag{20}$$

Interestingly, the calculated V_{film} (**Table 5**) are only 12% of the total V_{pore} (1.45 cm^3/g); the uncertainty predominantly comes from the chosen uncertainty range for $\rho_{\text{film,sat}}$ (± 20 g/L). As

discussed earlier (**Sec. 5.1**), the volume of the adsorbed film at higher temperatures is lower than both the pore's and the results obtained under cryogenic conditions (also see **Figure 27**).

Table 5. Adsorbed film volume and ratio to total pore volume at 296 and 273 K

T (K)	a	E_B (kJ/mol)	R^2	V_{film} (cm^3/g)	V_{film}/V_{pore}
296	10.5	5.08 ± 0.04	0.99993	0.17 ± 0.05	0.12
273	10.6	5.02 ± 0.03	0.99985	0.18 ± 0.05	0.12

5.3 Determination of the enthalpy of adsorption using calculated absolute adsorption isotherms

A common approach to calculating the enthalpy of adsorption ΔH is to apply the Clausius-Clapeyron relation [9,51] to isotherms data from two different temperatures:

$$\Delta H = \frac{RT_1T_2}{T_2 - T_1} \ln \frac{P_2}{P_1}, \tag{11}$$

where T_1 and T_2 are the temperatures at which the two adsorption measurements were taken and P_1 and P_2 are the pressures at which a constant number of particles exist in the adsorbed phase. As discussed in Ref. [52], the isotherms need to be compared at equal absolute adsorption, G_{abs}. Experimentally, only the excess adsorption G_{ex} is measured directly, thus a conversion is necessary:

$$G_{abs} = G_{ex} + \rho_{gas} V_{film.} \tag{9}$$

Common assumptions are $V_{film} = 0$ (i.e., G_{ex}) and $V_{film} = V_{pore}$ (which overestimates $G_{abs} = G_{st}$, obviously $V_{film} \leq V_{pore}$). The former assumption overestimates ΔH, whereas the latter underestimates it [53–56]. We observed (**Sec. 5.1**) that for BR-0311 V_{film} = 0.58 cm^3/g at cryogenic temperatures (≈ 40% of V_{pore} = 1.45 cm^3/g); at room temperature, the discrepancy is even higher

($V_{\text{film}} \approx 0.12\ V_{\text{pore}}$, **Sec. 5.2)**. Using the Using V_{film} determined earlier (**Sec. 5.2b**), absolute adsorption isotherms for 273 and 296 K are shown in **Figure 31** along with fits to the Modified Redlich-Peterson model (MRP with $R^2 > 0.9999$) [57]:

$$G_{\text{abs}} = \frac{a(bP)^{1-c}}{1 + (bP)^{1-c}}. \tag{13}$$

The fits are used to interpolate between experimental points to determine points of constant coverage at the two temperatures in the Clausius-Clapeyron relation (**Eq. (11))**.

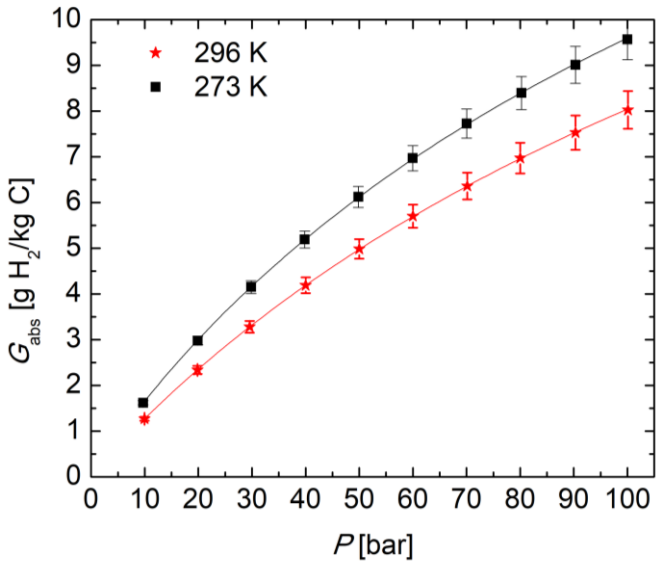

Figure 31. G_{abs} isotherms using the calculated V_{film}**,** with the accompanying Modified Redlich-Peterson fit [57]. Error bars are predominantly due to the uncertainty in V_{film}**.**

Applying the Clausius-Clapeyron relation at cryogenic temperatures demonstrates the initial low coverage enthalpy of adsorption and how it decreases with increasing coverage, see **Figure 32 (a)**. This is because the first binding sites that are occupied at low coverage are the deepest potential wells. Once those sites are filled, shallower sites are filled with increasing coverage.

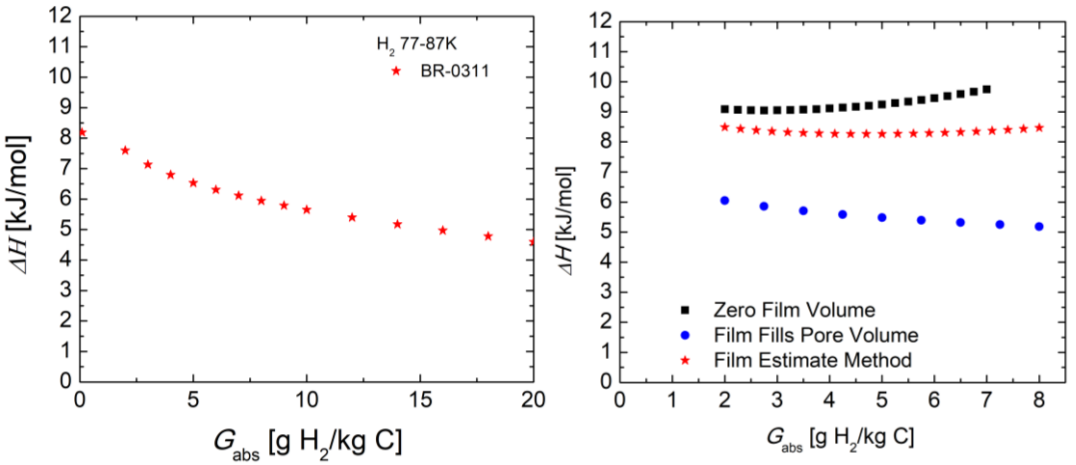

Figure 32. Enthalpy of adsorption calculations under cryogenic conditions and room temperature. (a) Enthalpy of adsorption calculated using 77 and 87 K isotherms. (b) enthalpy of adsorption using three different film volumes at room temperature: the calculated film volumes from the Ono-Kondo fits (red), the film volume equal to zero $G_{abs} = G_{ex}$ (isoexcess) (black), and the film volume equal to the pore volume $G_{abs} = G_{st}$ (isostorage) (blue). Error bars are not included to simplify the visualization.

In **Figure 32 (b)**, three different V_{film} assumptions were used to determine G_{abs} and to calculate the enthalpy of adsorption. For $V_{film} = 0$ ($G_{abs} = G_{ex}$), this leads to a larger enthalpy of adsorption (9 kJ/mol) and an unphysical increase at larger coverage (as discussed, at larger coverage shallower sites should be filled, so for heterogeneous samples ΔH should decrease with coverage). The assumption $V_{film} = V_{pore}$ ($G_{abs} = G_{st}$) leads to a enthalpy of adsorption that is smaller (6 kJ/mol). Since these too approximations are the most extreme assumptions regarding the V_{film}, an upper and lower bound are set on the enthalpy of adsorption. This narrows the possible values of the enthalpy of adsorption to a 3 kJ/mol range, a 30-50% error!

Using our V_{film} estimate yields a relatively constant 8.3 kJ/mol at 273 and 296 K. This is extremely close to the enthalpy of adsorption calculated at 77 and 87 K of 8.2 kJ/mol at low coverage. As

expected, at higher temperature, only the sites with the deepest potentials are populated (these deep potential sites are the ~8 kJ/mol wells, at cryogenic temperatures, the high binding energy sites are occupied first at low coverage and then more shallow potential sites down to 5 kJ/mol become occupied).

6 Deliverable Storage Capacity

When considering the benefits of adsorption technology in a full scale tank, an important metric is the amount of gas that can actually be delivered from the tank. This quantity, just like so many other metrics will depend on the tradeoffs between porosity, surface area, and binding energy. When examining the factors that increase volumetric storage, it would seem advantagous to use an adsorbent with low porosity, high surface area, and a high binding energy. Low porosities and high surface areas promote larger volumetric storage capacites. Materials with high binding energies form a fully saturated film at lower pressures than materials with lower binding energies. Types of samples with very large binding energies, such as MOFs, will not perform as strongly when it comes to deliverable storage. They will tend to have larger quanties of gas still bound at low pressure. This would then require external heating or pumping to deliver the desorb the bound gas. Something with a more reversible adsorption process would be desired. Therefore, even if an adsorbent outperforms compressed gas, it may not be beneficial to use in a storage tank depending on the maximum operating pressure and the rail (or delivery) pressure of the tank. In order to determine the deliverable storage capacity of a tank, one must know the amount of gas stored at the maximum operating pressure of the tank, P_{max}, and at the rail pressure of the system, P_{rail}. The volumetric storage capacity can be defined as

$$V_{\mathrm{st,Del}} = V_{\mathrm{st}}(P_{\mathrm{max}}) - V_{\mathrm{st}}(P_{\mathrm{rail}}) \tag{10}$$

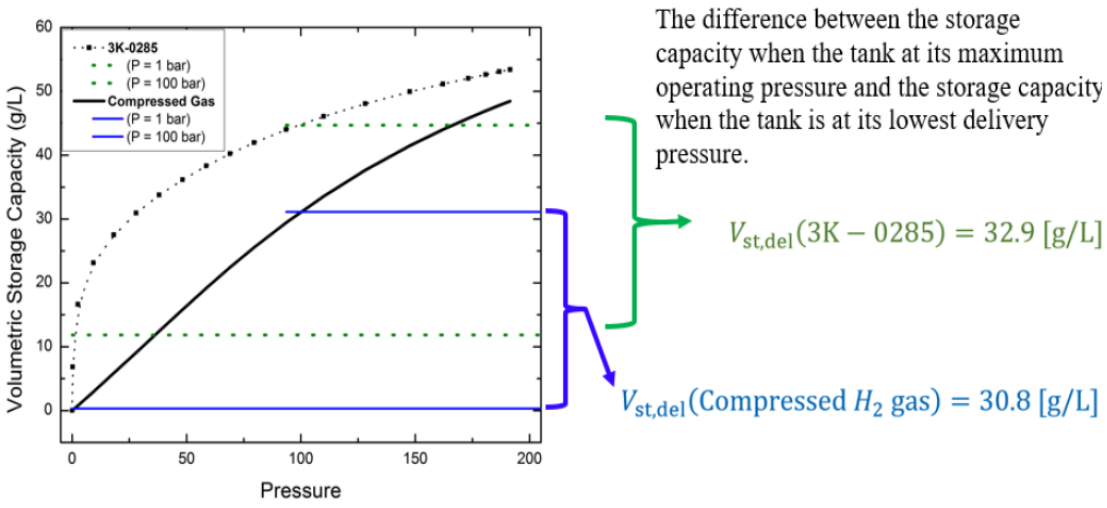

Figure 33. Deliverable storage capacity of a PAC operating between 100 and 1 bar compared to compressed hydrogen [40].

While the adsorbent clearly has a larger volumetric storage capacity, it increases so rapidly during the low pressure that it will have a non-trivial amount of gas unusable without pumping or heating. The adsorbent still has the edge in deliverable storage over compression, but only by 2 g/L for a tank operating from 100-1 bar at 77 K. It is important to note that the choice of operating pressures could bias the process of screening samples in terms of their deliverable storage. Samples like MOFs (high surface area and binding energies) would benefit in the analysis if the lowest possible rail pressure was chosen. This is because of how rapidly the storage increases at low pressures, and could make it appear there is much more deliverable storage than in reality. Likewise, choosing the largest possible rail pressure would bias deliverable storage capacity in favor of low binding energy adsorbents or compressed gas. Including an adsorbent material is most beneficial at lower pressures (25-50 bar) because this is where the increased performance over compressed gas is maximized.

Unless otherwise indicated, for the purposes of this document I will be using the pressures 100 bar and 2 bar for P_{max} and P_{rail}, respectively. Various other configurations will be discussed and will be indicated. In order to accurately determine the storage capactity at these specific pressures, The Modified Redlich Peterson model was used to interpolate between raw data measured on the monoliths and PAC at various temperatures. All data on the PAC 3K-0285 and the monolith BR-0311 were measured with the Hiden instrument by Gillespie [40]. All methodology and analysis is new work first reported in this document.

6.1 Monolith Deliverable Storage

When investigating storage capacities, it is important to recognize that while excess adsorption will be the same for a given sample, the volumetric storage capacity will vary depending on the choice of porosity. One can use the porosity of the individual crystal or that of the entire tank. For our monolith BR-0311 and our 10LSS the porosities are 0.72 and 0.73, respectively. These values are so similar because of the near perfect packing of sample into the tank (packing fraction of 0.96).

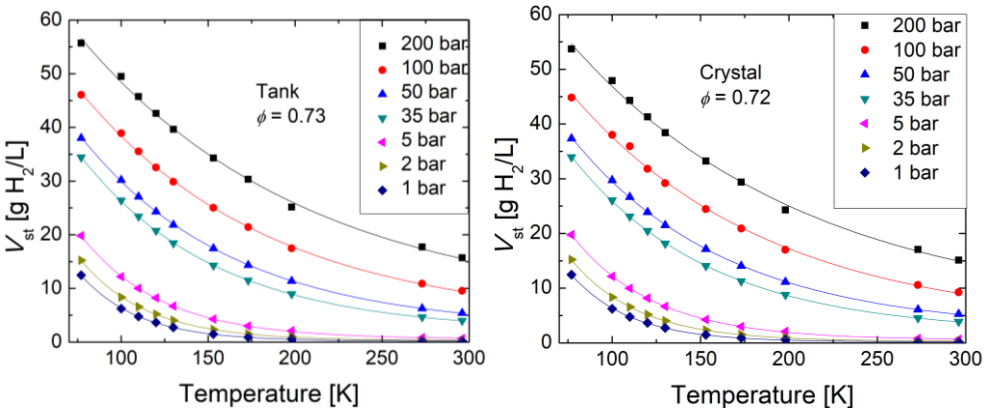

Figure 34. Volumetric Storage Capacities for crystal and tank porosities on monoliths. *Left*: The storage capacity for individual monoliths/crystals. *Right:* Storage capacity for our tank packed with monoliths.

From **Figure 34**, we observe fairly small differences in storage capacity for the two different porosities. These plots also contain the information needed to select various different combinations of maximum and rail pressures. Each of these isobars can be fit with a single-term exponential decay given by

$$V_{\mathrm{st}} = y_0 + A_1 e^{-T/t_1} \tag{32}$$

Using these fits, one could interpolate to predict the storage at any desired operating temperature between 77 K and room temperature. The fitting parameters for each of these isobars are listed in the table below.

Table 6. Exponential Decay Fitting Parameters for Monolith Isobars

	Crystal			**Tank**		
Pressure (bar)	**Y_0 (g/L)**	**A_1 (g/L)**	**t_1 (K)**	**Y_0 (g/L)**	**A_1 (g/L)**	**t_1 (K)**
1	0.19	120	34	0.19	120	34
2	0.30	110	38	0.30	110	38
5	0.54	100	47	0.56	100	47
35	1.9	86	79	2.0	87	78
50	2.3	84	88	2.4	86	88
100	3.0	84	110	3.6	87	110
200	5.3	88	130	6.0	91	130

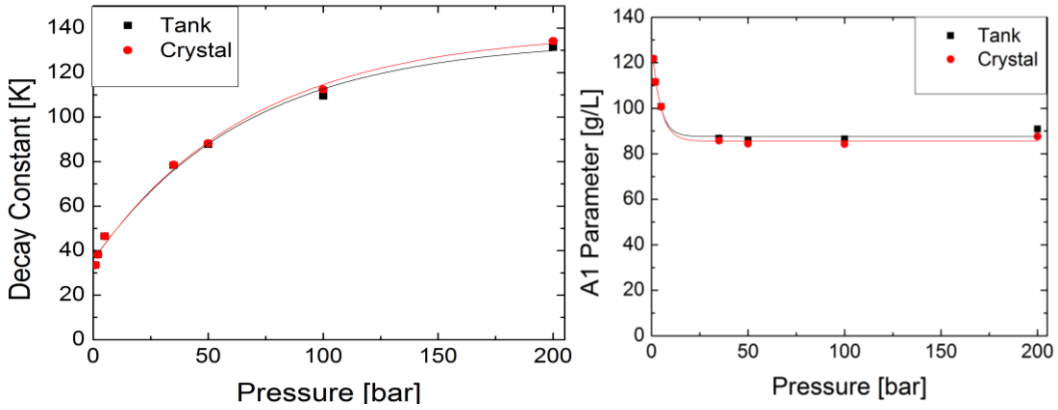

Figure 35. Single-term exponential decay parameters for monolith storage isobars. *Left*: The decay constant for each isobar. *Right:* The A1 parameter for each isobar.

The fitting parameters vary little between the two porosities and the decay constant from the exponential fits increases non-linearly when plotted against pressure. Extracting the decay constants from the isobaric data shows a single-term exponential decay relationship.

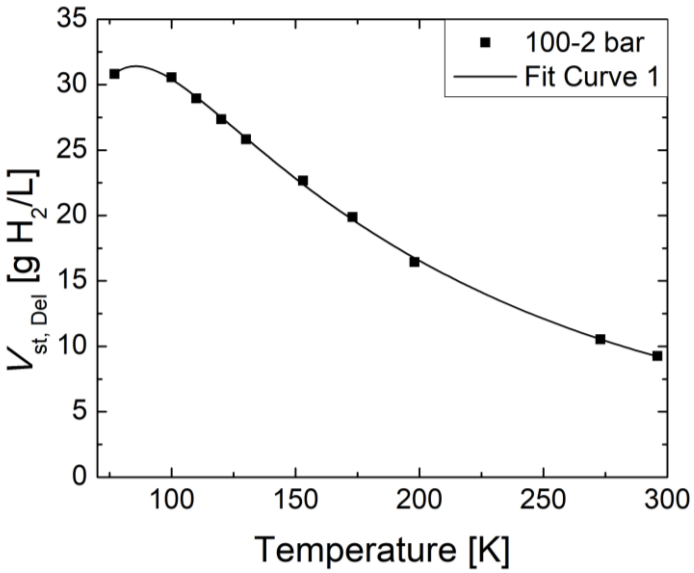

Figure 36. Deliverable volumetric storage capacity vs temperature for monoliths.

Taking the previous data and turning it into deliverable storage capacity for a tank operating between 100 bar and 2 bar yields **Figure 36**. The deliverable storage capacity overall tends to decrease with increasing temperature. This is largely due to the large decreases in volumetric storage at higher temperatures. However, the increase in deliverable storage seems to begin to flatten out somewhere between 100 K and 77 K. This occurs because the amount of gas stored at 2 bar becomes large enough that it detracts noticeably from the performance of the tank. In order to make a storage temperature at 77 K or lower more beneficial, an external source of energy would be needed to extract additional gas.

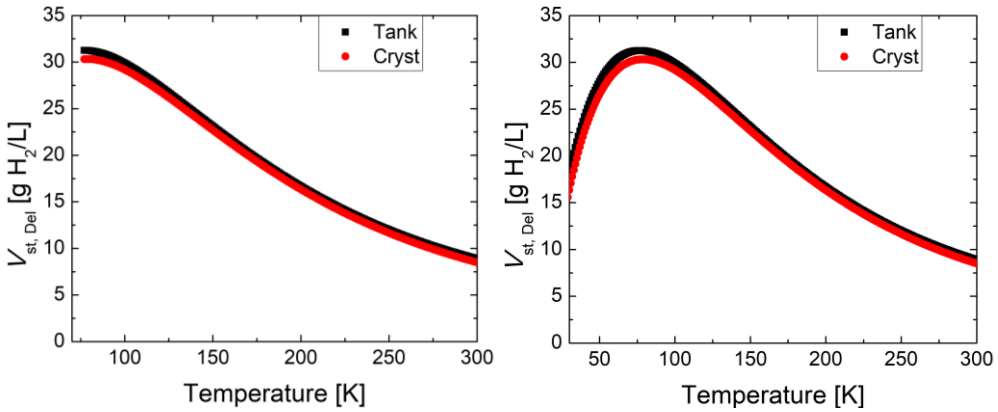

Figure 37. Deliverable storage capacity interpolation and extrapolation for monoliths. *Left*: Deliverable storage interpolated showing strong agreement with data. *Right:* Deliverable storage extrapolated to show maximum.

Using data interpolated from the 100 bar and 2 bar exponential decay fits allows us to plot the deliverable storage capacity more completely. Again, the storage does not change much whether discussing the performance of individual monoliths vs that of the tank. Using the parameters from the two individual exponential decay fits, **Figure 37** can be fit with a two-term exponential decay

$$V_{\mathrm{st,Del}} = y_0 + A_1 e^{-T/t_1} + A_2 e^{-T/t_2} \tag{33}$$

after modifying the fitting parameters to approximate those of the individual fits. Maximizing this relationship indicates a maximum at 76.8 K for the tank and 78.7 K for the crystal. There are ways to drive this maximum to lower temperatures starting with how we defined deliverable storage capacity

$$V_{\mathrm{st,Del}}(P_{\mathrm{max}}, P_{\mathrm{rail}}, T) = V_{\mathrm{st}}(P_{\mathrm{max}}, T) - V_{\mathrm{st}}(P_{\mathrm{rail}}, T) \tag{34}$$

We can then substitute in the exponential decay equations from the two different isobars. Then maximize this relationship

$$\frac{dV_{\mathrm{st,Del}}(P_{\mathrm{max}}, P_{\mathrm{rail}}, T)}{dT} = -\frac{A_{\mathrm{P_{max}}}}{t_{\mathrm{P_{max}}}} e^{-T/t_{\mathrm{P_{max}}}} + \frac{A_{\mathrm{P}_{rail}}}{t_{\mathrm{P}_{rail}}} e^{-T/t_{\mathrm{P_{rail}}}} = 0 \tag{35}$$

Solving for T leaves us with a way to approximate at which temperature the maximum deliverable storage occurs for different operating pressures

$$T_{\mathrm{max}} = \frac{t_{\mathrm{P_{max}}} t_{\mathrm{P}_{rail}}}{t_{\mathrm{P}_{rail}} - t_{\mathrm{P_{max}}}} \ln\left(\frac{A_{\mathrm{P_{max}}} t_{\mathrm{P}_{rail}}}{A_{\mathrm{P}_{rail}} t_{\mathrm{P_{max}}}}\right) \tag{36}$$

Table 7. Tank Operating Pressures and Maximum Deliverable Storage at T_{mas} for monoliths

	Crystal		Tank	
Operating Pressure Range (bar)	**T_{max} (K)**	**$V_{st,Del}$ at T_{max} (g/L)**	**T_{max} (K)**	**$V_{st,Del}$ at T_{max} (g/L)**
200-1	77	42	75	44
200-2	80	39	78	41
200-5	85	35	82	37
100-1	75	33	74	34
100-2	79	30	77	31
100-5	84	26	82	27
50-1	72	25	71	26
50-2	75	22	74	23
35-1	70	22	70	22
35-2	80	19	79	19
50-5	73	18	72	18
35-5	78	14	77	15

Through these various configurations, the temperature at which the maximum deliverable storage can be lowered. However, that does not necessarily yield the largest possible deliverable storage compared to all configurations. A tank operating from 35 to 1 bar will have the lowest temperature (of the ones analyzed) at 69.6 K, but only have a deliverable storage capacity of 22.2 g/L at that temperature. All of the tank configurations operating at 200 or 100 bar outperform this at slightly higher temperatures. The highest deliverable storage comes from the 200 to 1 bar tank because of the large pressure difference.

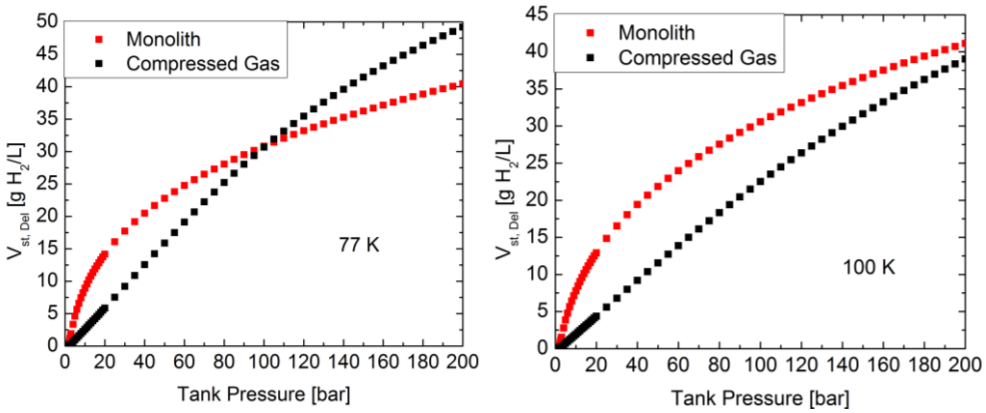

Figure 38. Deliverable storage capacity for monoliths compared to compressed gas. *Left*: Deliverable storage at 77 K. *Right:* Deliverable storage at 100 K.

However, if these temperatures are decreased to 77 K or colder, there will be pressure regimes where compressed gas will outperform the monoliths. **Figure 38** demonstrates that around 100 bar at 77 K compressed gas can deliver more gas. The monoliths still outperform compressed gas below 100 bar. On the other hand, operating a tank at 100 K allows the monoliths to outperform compressed gas through the entire pressure range (up to 200 bar).

6.2 PAC Deliverable Storage

The analysis from the previous section was applied to the only other sample measured in the 10LSS, the PAC. The porosities of the PAC precursor and the 10LSS are 0.78 and 0.86, respectively. Using the powdered sample, our tank could only be packed as efficiently as random close-packed spheres (packing fraction of 0.64).

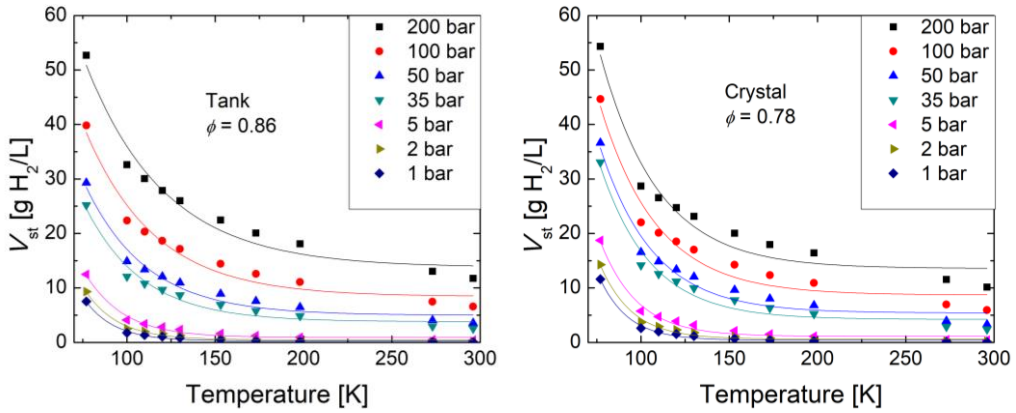

Figure 39. Volumetric Storage Capacities for crystal and tank porosities on PAC fitted with a one term exponential decay. *Left*: The storage capacity for individual crystal. *Right:* Storage capacity for our tank packed with PAC.

The single term exponential decay fits for the PAC are not quite as good (R^2=0.964-0.990). This occurs for both porosities. The analysis is continued with these single term fits and also attempted with a two-term exponential decay fit. The fitting parameters for the single-term fits are listed in the table below.

Table 8. Single-Term Exponential Decay Fitting Parameters for PAC Isobars

	Crystal			**Tank**		
Pressure (bar)	**Y_0 (g/L)**	**A_1 (g/L)**	**t_1 (K)**	**Y_0 (g/L)**	**A_1 (g/L)**	**t_1 (K)**
1	0.40	1300	16	0.30	780	16
2	0.60	1000	18	0.50	580	18
5	1.1	720	21	0.90	400	22
35	4.2	420	29	3.8	230	32
50	5.4	390	30	5.0	220	35
100	8.7	380	32	8.4	210	39
200	14	420	33	14	210	45

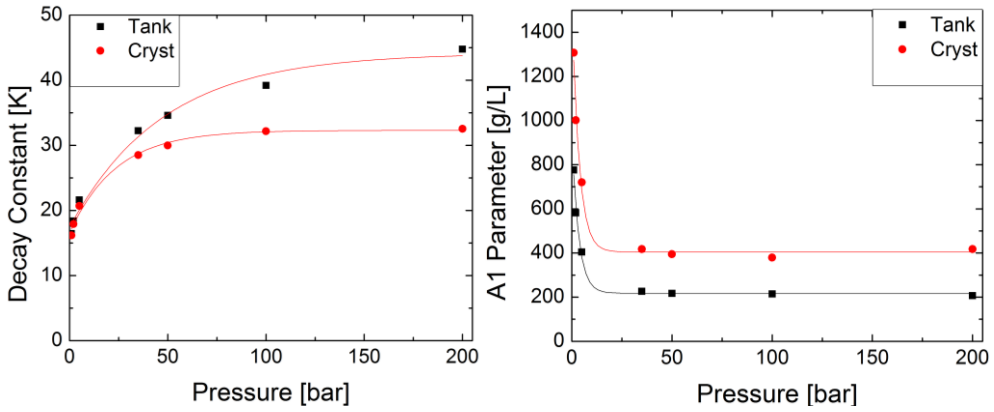

Figure 40. Single-term exponential decay fitting parameters for PAC storage isobars. *Left*: The decay constant for each isobar. *Right:* The A1 parameter for each isobar.

The decay constants increase non-linearly with pressure and range from 16 K to 33 K for the lower porosity and 45 K for the larger porosity. The trend can be fit with an exponential fairly well. The A1 parameter decreases rapidly at lower pressures and by 20 bar seems to almost level off while slightly decreasing.

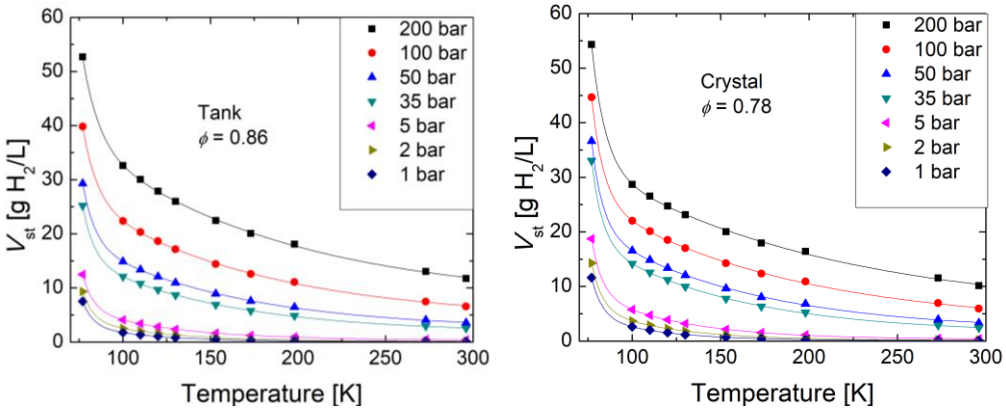

Figure 41. Volumetric Storage Capacities for crystal and tank porosities on PAC two-term exponential decay. *Left*: The storage capacity for individual crystal. *Right:* Storage capacity for our tank packed with PAC.

Fitting the volumetric storage capacity isobars with a two-term exponential decay greatly increases the consistency of the fits (R^2=0.9996-0.9999). Using these fits does make it more difficult to

observe trends in the fitting parameters. The fitting parameters for each of these isobars are listed in the table below.

Table 9. Two-Term Exponential Decay Fitting Parameters for PAC Isobars

	Crystal					Tank				
Pressure (bar)	**Y_0 (g/L)**	**A_1 (g/L)**	**t_1 (K)**	**A_2 (g/L)**	**t_2 (K)**	**Y_0 (g/L)**	**A_1 (g/L)**	**t_1 (K)**	**A_2 (g/L)**	**t_2 (K)**
1	0.10	31	39	3.6E+06	5.9	0.10	19	40	2.0E+06	5.9
2	0.10	35	43	5.3E+06	5.8	0.10	22	44	2.7E+06	5.9
5	0.30	39	50	7.6E+06	5.7	0.30	25	52	3.6E+06	5.9
35	1.7	44	80	6.4E+06	5.9	1.7	35	81	2.3E+06	6.2
50	2.3	44	89	5.1E+06	6.1	2.3	38	88	9.0E+05	6.8
100	3	46	110	2.2E+06	6.6	4.1	46	100	1.8E+05	8.1
200	7.6	48	130	5.8E+05	7.6	7.6	57	120	7.8E+04	9.1

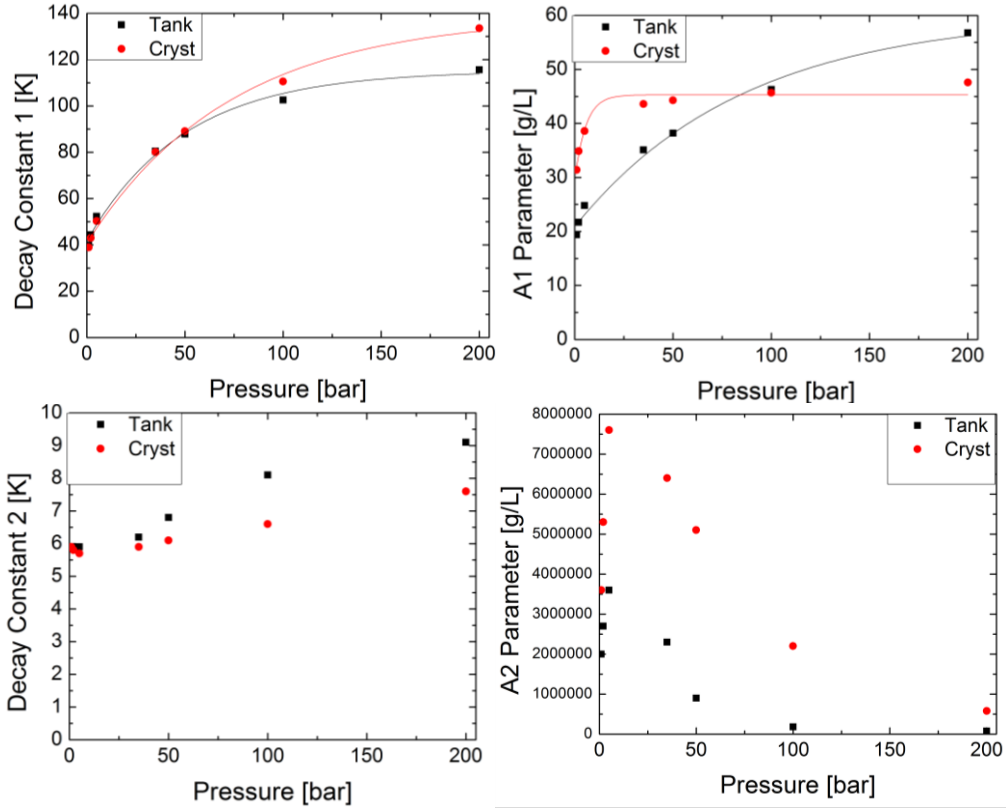

Figure 42. Two-term exponential decay fitting parameters for PAC storage isobars. *Top Left*: The Decay constant 1 for each isobar. *Top Right:* The A1 parameter for each isobar. *Bottom Left*: The decay constant 2 for each isobar. *Bottom Right:* The A2 parameter for each isobar.

The A2 parameter seems the most out of place having values orders of magnitude larger than the A1 parameter. The parameter still seems to have similar structure between the two porosities. The values increase some from 1 bar to 5 bar, but the values decrease through the rest of the pressures. The decay constant 2 that is associated with the exponential term A2 does not vary much (range of 3 K), but does increase with pressure and diverges with the higher tank porosity having larger values. The A1 for the crystal increases at low pressure and levels off around 20 bar, but does increase overall. The parameter for the tank has a more gradual and ongoing increasing trend. Both trends can be fit with an exponential decay with some accuracy (R^2 = 0.930 and 0.986). The decay constant 1 has a continually increasing trend similar to the single-term fit, but with larger values.

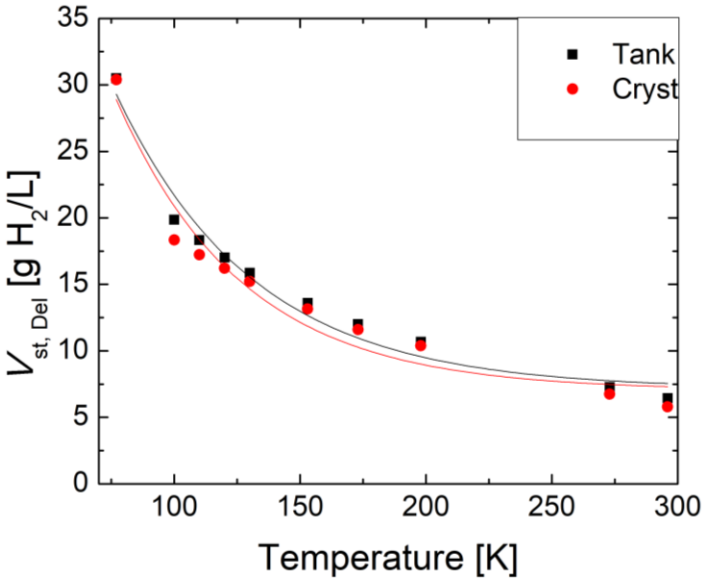

Figure 43. Deliverable storage capacity at measured temperatures with two-term exponential fit**.**

From **Figure 43**, the deliverable storage data can be fit with a two-term exponential decay, regardless of the chosen fit for storage. This graph of deliverable storage is from the collected data for a tank operating between 100-2 bar and does not require exponential interpolation of storage data. The curve for tank data is more gradual and doesn't have such a dramatic of a bend from 100 K to 77 K. However, these data are not fit very well by a single-term fit (R^2 of 0.94 to 0.96). These fits also do not seemingly relate to the individual 100 bar and 2 bar fitting parameters.

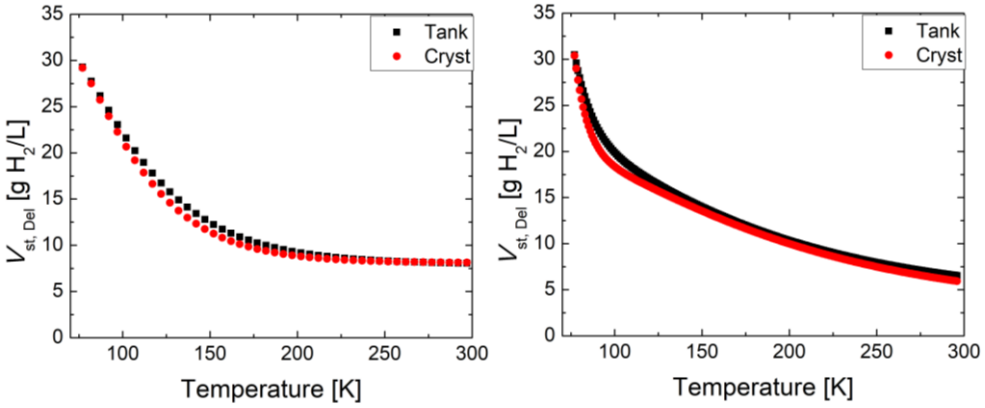

Figure 44. Deliverable storage interpolation for PAC. *Left*: Deliverable storage interpolation calculated with single-term exponential. *Right:* Deliverable storage interpolation calculated with two-term exponential.

Using the parameters from the single-term and two-term exponential fits for the individual 100 bar and 2 bar fits, we can interpolate the deliverable storage at any temperature from 77 K to 296 K. The difference between the porosities is not very large for the single-term interpolation. During the middle temperature range from 100 K to 200 K, the tank has a slightly larger deliverable storage. The two-term interpolation is more similar to the fits to the data in **Figure 44**. The tank porosity yields a more gradual curve, thus slightly larger deliverable storage from 77 K to 125 K.

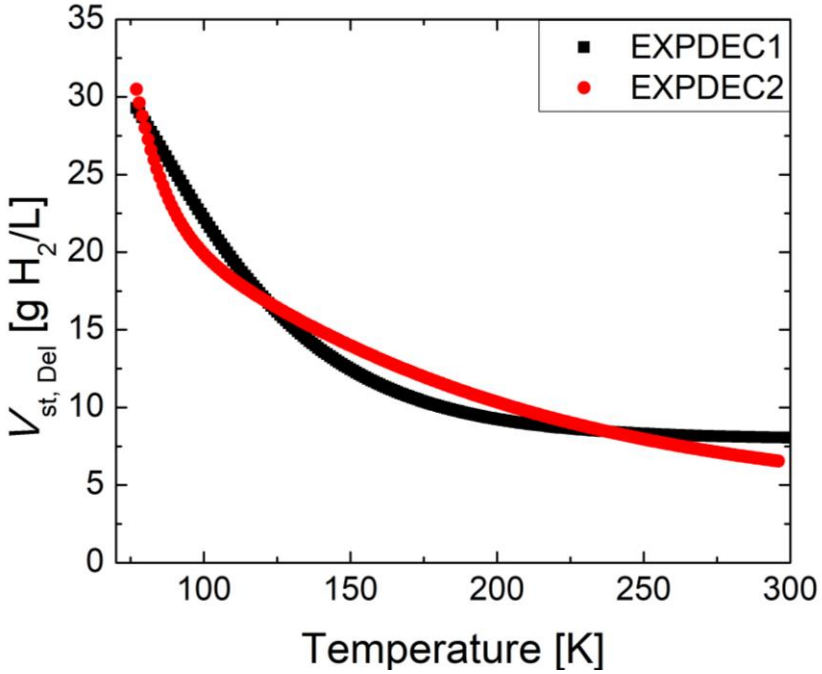

Figure 45. Deliverable storage capacity comparing the single-term and two-term exponential interpolations.

Figure 45 shows the differences in the two different exponential interpolation methods. The single-term method indicates a larger deliverable storage from 77 K until a crossover around 125 K. Then the two-term is larger until a second crossover around 240 K.

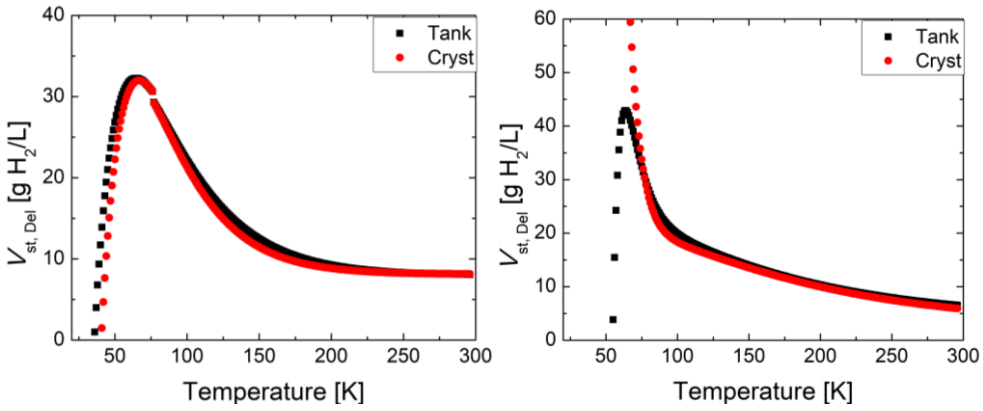

Figure 46. Deliverable storage extrapolation for PAC. *Left*: Deliverable storage calculated with single-term exponential. *Right:* Deliverable storage calculated with two-term exponential.

Extrapolating data from these two different exponential fits yields a prediction as to what temperature the maximum deliverable storage capacity occurs. The peak for both of these graphs is less broad than that of the monolith deliverable storage. The single-term extrapolation is broader than the two-term and occurs around 62 K for a maximum deliverable storage of 32 g/L. The two-term extrapolation yields much sharper peaks and is different for the two porosities. The maximum deliverable storage for the tank porosity is 43 g/L at 64 K, but the crystal porosity indicates ~295 g/L at 46 K. This seems a bit extreme and suggests the extrapolation from the two-term exponential may not be as accurate.

Table 10. Tank Operating Pressures and Maximum Deliverable Storage at T_{max} for PAC

	Crystal		**Tank**	
Operating Pressure Range (bar)	**T_{max} (K)**	**$V_{st,Del}$ at T_{max} (g/L)**	**T_{max} (K)**	**$V_{st,Del}$ at T_{max} (g/L)**
200-1	59	47	60	48
200-2	59	44	60	45
200-5	57	39	58	42
100-1	63	35	61	34
100-2	63	32	61	32
100-5	63	27	59	29
50-1	64	27	63	23
50-2	64	24	63	21
35-1	64	23	64	19
50-5	65	18	63	17
35-2	64	20	64	17
35-5	65	15	64	13

Through these various configurations, the temperature at which the maximum deliverable storage occurs, can be lowered. Yet, that does not necessarily yield the largest possible deliverable storage compared to all configurations. A tank operating from 200 to 5 bar will have the lowest temperature (of the ones analyzed) at 58.4 K, but only have a deliverable storage capacity of 42 g/L at that temperature. Only the tank configurations operating at 200 bar and with lower rail pressures

outperform this at slightly higher temperatures. The highest deliverable storage comes from the 200 to 1 bar tank because of the large pressure difference.

6.3 Deliverable Storage Comparisons with Compressed Gas

It is ultimately of importance to analyze the deliverable storage performance of compressed gas. This can then be compared to the performance of the monoliths and the PAC. All compressed gas densities were calculated from the NIST database.

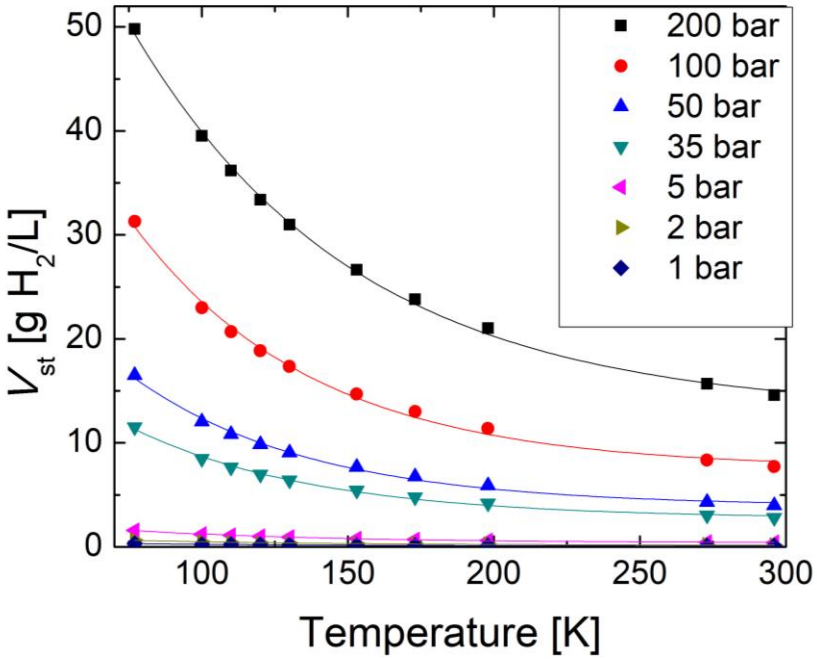

Figure 47. Volumetric Storage Capacities for compressed gas isobars.

From **Figure 47**, we observe that the compressed gas density exhibits exponential behavior. The lower rail pressure isobars are extremely small compared to any of the maximum operating pressure isobars. This will lead to deliverable storage capacities that are not much less than the storage capacities at the max operating pressure. Each of these isobars can be fit with a single-term exponential decay.

Using these fits, one could interpolate to predict the storage at any desired operating temperature between 77 K and room temperature. The fitting parameters for each of these isobars are listed in the table below.

Table 11. Exponential Decay Fitting Parameters for Compressed Gas Isobars

Pressure (bar)	**Y_0 (g/L)**	**A_1 (g/L)**	**t_1 (K)**
1	0.10	0.7	72
2	0.10	1.4	71
5	0.40	3.6	70
35	2.7	29	63
50	3.9	43	61
100	7.6	81	62
200	13	99	77

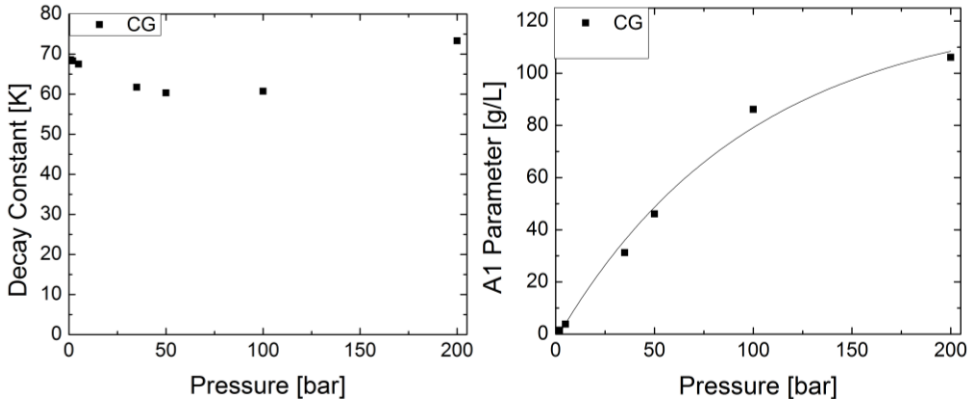

Figure 48. Single-term exponential decay parameters for compressed gas storage isobars. *Left*: The decay constant for each isobar. *Right:* The A1 parameter for each isobar.

The decay constants for the isobars do not have a clear trend. They range from 60 K to 75 K. The A1 scaling parameter does tend to increase with pressure and can be fit with an exponential fit.

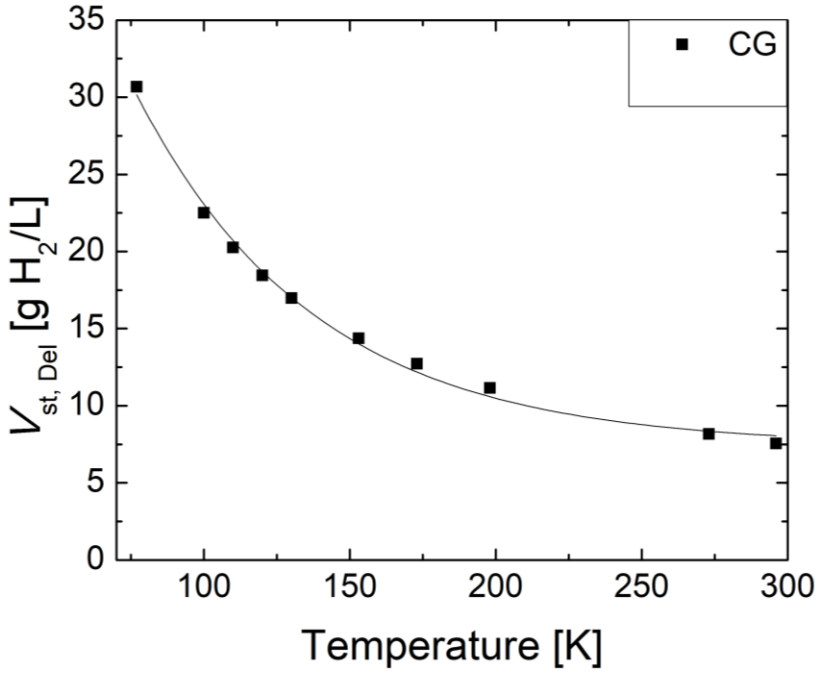

Figure 49. Deliverable volumetric storage capacity vs temperature for 100-2 bar tank with compressed gas.

Taking the previous data and turning it into deliverable storage capacity for a tank operating between 100 bar and 2 bar yields **Figure 49**. The deliverable storage capacity overall tends to decrease with increasing temperature. The storage at 2 bar ranges from 0.2-0.6 g/L (296-77 K). This indicates that around 98% of all the hydrogen stored is deliverable, even at 77 K. The deliverable storage capacity can be fit with a single-term exponential (R^2 = 0.9948).

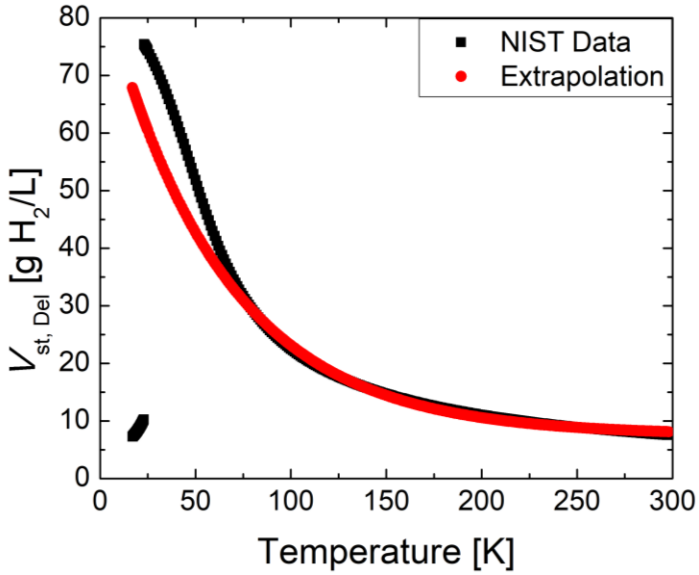

Figure 50. Deliverable storage capacity interpolation and extrapolation for compressed gas. *Left*: Deliverable storage interpolated showing strong agreement with data. *Right:* Deliverable storage extrapolated to show divergence.

The fit of the deliverable storage capacity can be used to interpolate to any temperature between 77 K and 296 K. This interpolation is in close agreement with NIST data. Taking this fit and extrapolating to lower temperatures proves unreliable. The extrapolation diverges by 5% around 70 K and 10% around 60 K. The NIST data begins to increase more rapidly and ultimately shoots down around the boiling point of hydrogen (20 K). This makes sense that the deliverable storage would become small when the density at both 100 bar and 2 bar are nearly the same when hydrogen is liquid.

After investigating the deliverable storage capacity of hypothetical tanks with the monoliths, PAC, and compressed gas individually, we will now compare and contrast the three. It will also be important to investigate the advantages or disadvantages our samples possess.

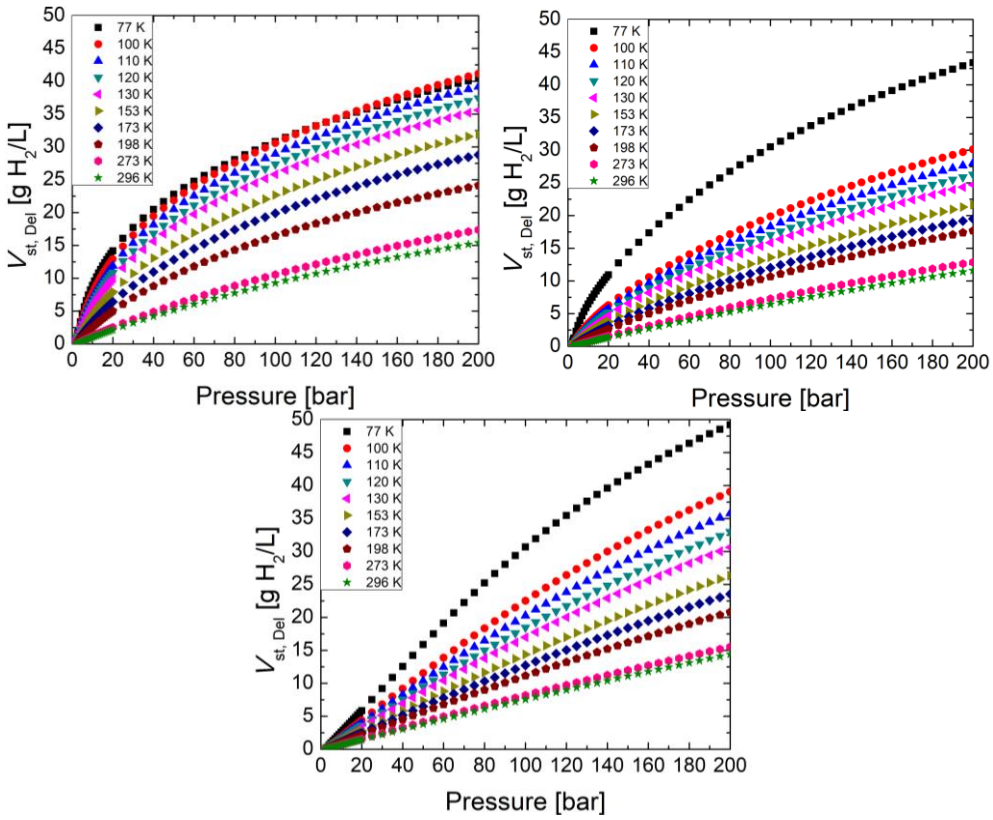

Figure 51. Deliverable storage capacity across for each temperature vs pressure. *Top Left*: Monolith. *Top Right:* PAC. *Bottom:* Compressed gas.

Figure 51 was created using the rail pressure of 2 bar to then investigate how the maximum pressure changes deliverable storage capacity. The monoliths seem to experience a crossover between the 100 K and 77 K deliverable storage capacity curves. This is reflected by the leveling off around 77 K observed previously. The PAC has quite a large increase in deliverable storage going from 100 K to 77 K. This is likely due to the larger porosity of a tank packed with PAC (0.86). There is therefore more volume for the gas, which is becoming more dense to fill. Since this gas is in the bulk phase, it would more readily discharge from the tank not having bound by adsorption.

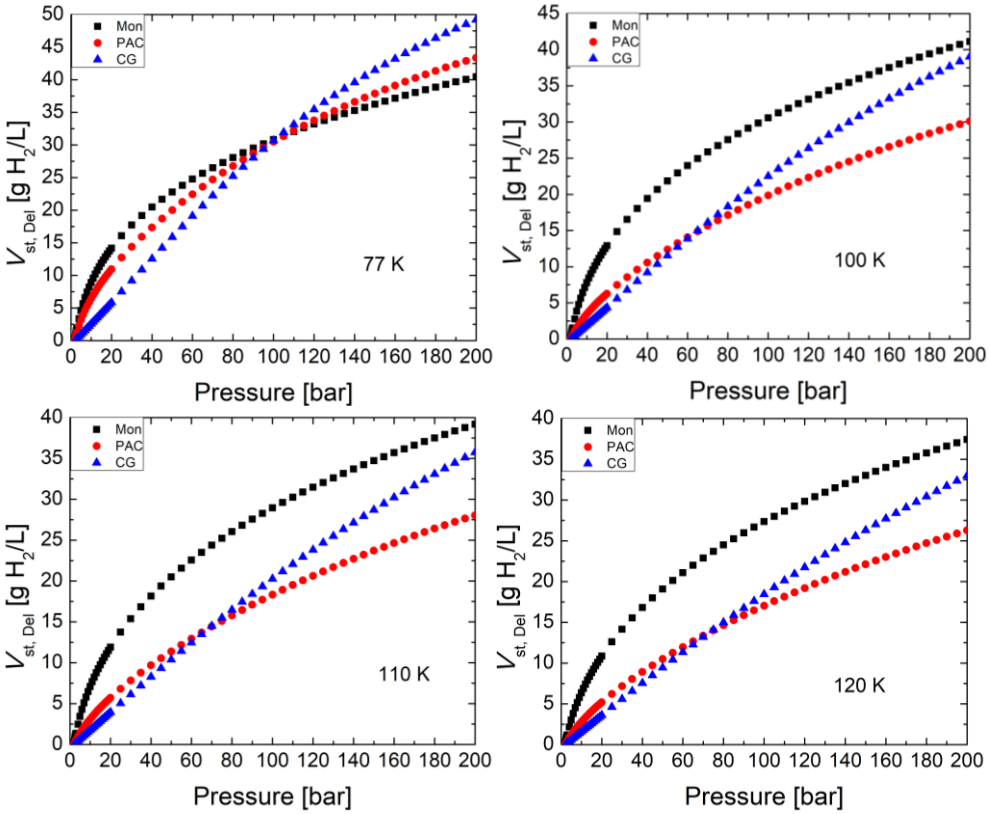

Figure 52. Deliverable storage capacity compared to compressed gas at 77 K through 120 K. *Top Left*: Deliverable storage at 77 K. *Top Right:* Deliverable storage at 100 K. *Bottom Left:* Deliverable storage at 110 K. *Bottom Right:* Deliverable storage at 120 K.

Both the monoliths and the PAC are outperformed by compressed gas after 100 bar at 77 K. The monoliths also perform better than the PAC up to 100 bar. Then it appears the PAC has more deliverable storage from 100 bar to 200 bar. At 100 K, the monoliths outperform compressed gas up through the entire pressure range, while the PAC only does better than compressed gas up to 60 bar and only slightly.

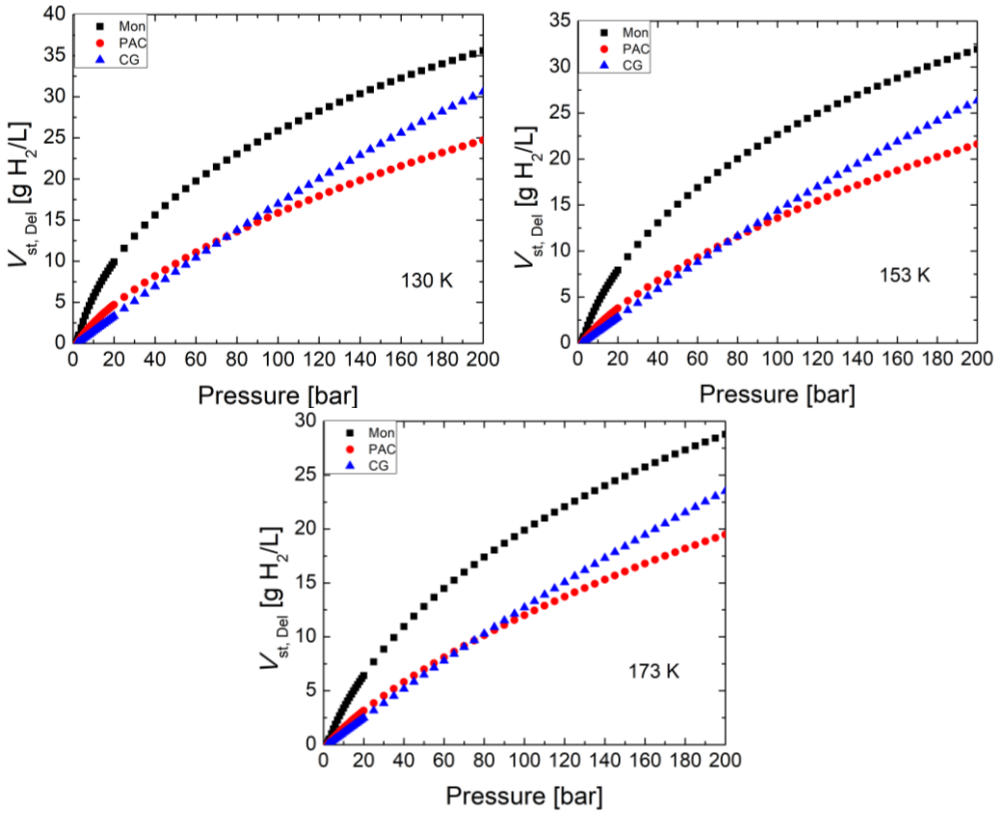

Figure 53. Deliverable storage capacity compared to compressed gas at 130 K through 173 K. *Top Left*: Deliverable storage at 130 K. *Top Right:* Deliverable storage at 153 K. *Bottom:* Deliverable storage at 173 K.

The monoliths are consistently able to deliver more gas than compressed gas across the majority of the temperature range investigated for a tank operating from 100-2 bar.

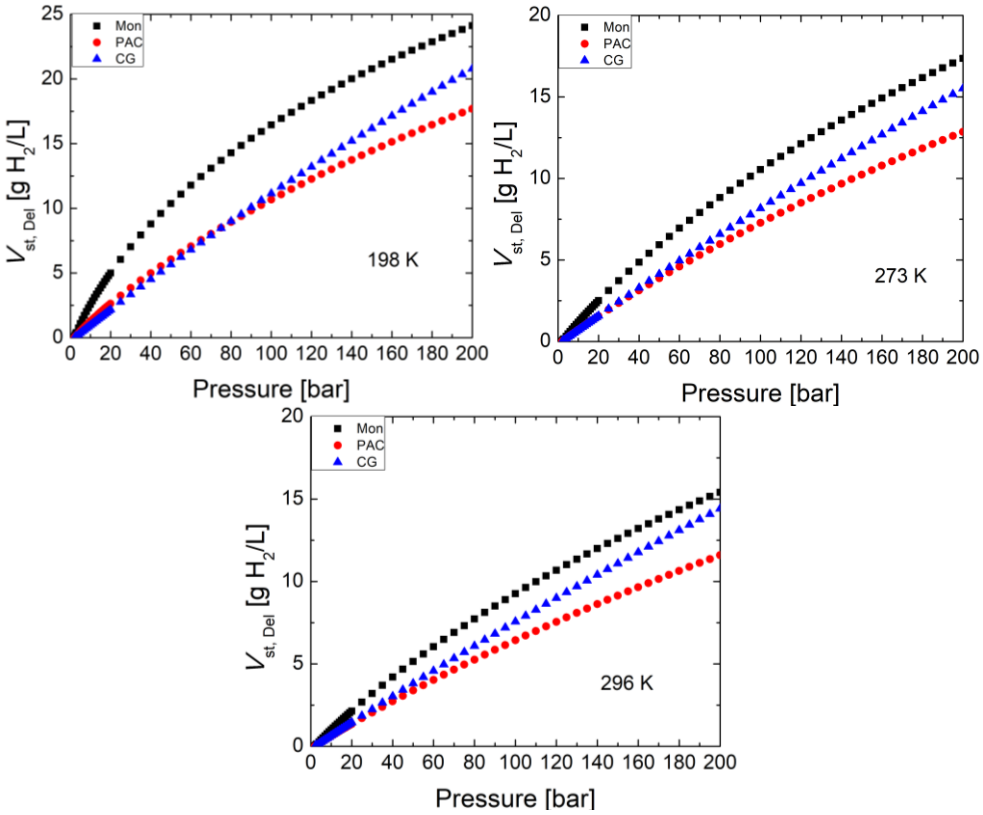

Figure 54. Deliverable storage capacity compared to compressed gas at 198 K through 296 K. *Top Left*: Deliverable storage at 198 K. *Top Right:* Deliverable storage at 273 K. *Bottom:* Deliverable storage at 296 K.

At the three temperatures that have been tested on the 10LSS (at least for the monoliths), the monoliths are still better in terms of storage capacity delivered. If the PAC were implemented in a tank at room temperature, compressed gas would be able to deliver close to the same or more, even at 198 K.

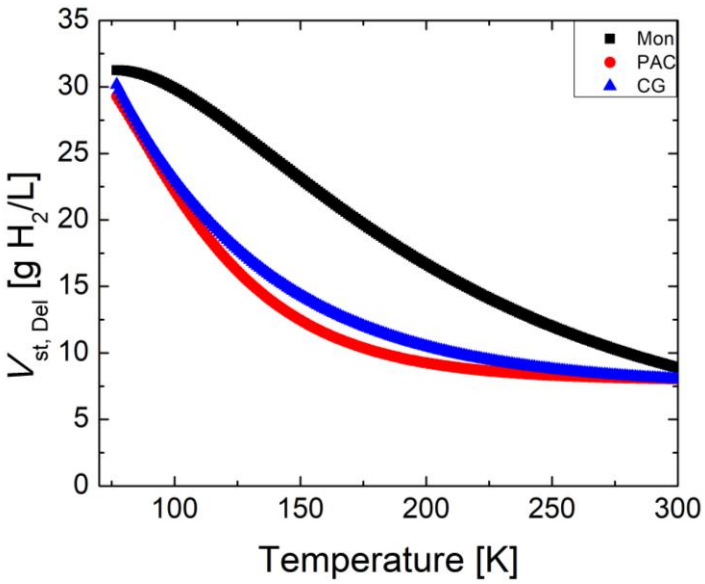

Figure 55. Deliverable storage capacity compared to compressed gas and PAC for a tank operating from 100-2 bar across all temperatures.

For a tank operating from 100-2 bar (similar to our 10LSS), the monoliths outperform compressed gas and the PAC from 77 K to 296 K. Close to 77 K the monoliths begin to level off, while compressed gas and the PAC continue to increase.

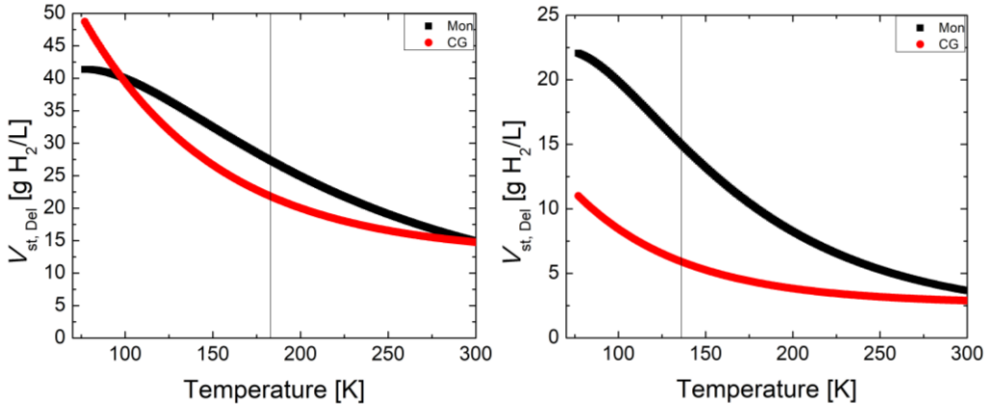

Figure 56. Deliverable storage capacity compared to compressed gas for different operating pressures. *Left*: Tank operating from 200-2 bar. *Right:* Tank operating from 35-1 bar.

Figure 56 compares two different tank configurations across all temperatures with compressed gas. A tank operating from 200-2 bar has a larger deliverable storage capacity than other configurations (20 g/L-40 g/L), but the difference between the monolith performance and compressed gas is less prominent. Also, around 100 K compressed gas begins to win against the monoliths and towards room temperature the two curves begin to converge. The vertical line on the graph indicates the temperature at which the maximum performance gain occurs. The maximum percent increase over compressed gas is 125% and occurs at 183 K. This is the lowest maximum percent increase of the configurations analyzed, but has the highest temperature at which the maximum increase occurs. This temperature is not much less than a dry ice bath. The configuration on the right is for a tank operating from 35-1 bar. This configuration yields the lowest operating temperature for maximum percent increase at 136 K. The percent increase is 254% and the deliverable storage continues to increase with decreasing temperature, just no longer faster than compressed gas. This makes sense because adsorption wins over compression at lower pressures.

Table 12. Compared Monolith Tank Configurations

Operating Pressure (bar)	Temperature Max Percent Increase Occurs (K)	Percent Increase Over Compressed Gas
35-1	136	254
35-2	143	241
50-1	147	220
50-2	153	212
100-1	166	167
100-2	170	164
200-1	178	127
200-2	183	125

7 Kinetic Behavior of the 10LSS

This section discusses some of the dynamic behaviors of the 10LSS. Some of the ramifications of using PAC or monolithic carbon are explored. Also, differences from using different temperature thermal baths are observed.

7.1 Room Temperature PAC

This section contains data that was collected with the tank in its original construction with PAC under Rash [83]. The dynamic data collected includes a small discharge (100-84 bar) and a fast fill (0-100 bar).

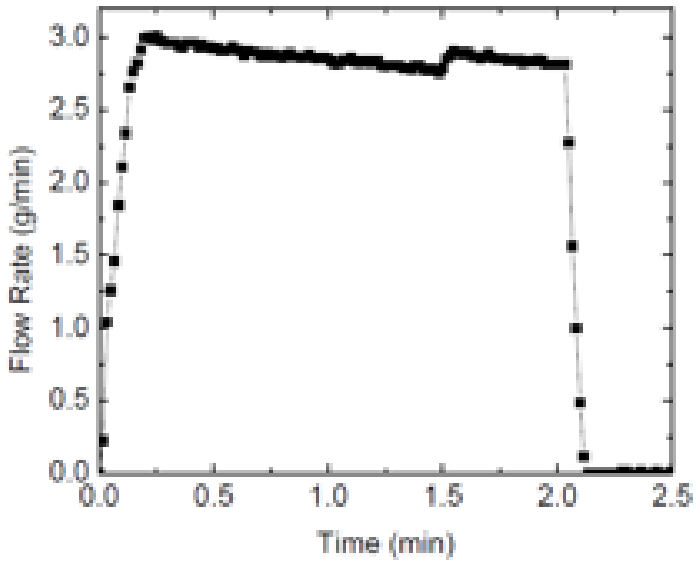

Figure 57. The flow rate that was measured between the 100 bar and 84 bar desorption data.

The flow rate was maintained around a constant 3 g/min for 2 minutes. During this desorption measurement, the tank is the supply for the gas. When the tank is more filled, it can supply a constant flow more easily than our pressure booster. However, as the tank discharges gas, desorption cools the tank making the hydrogen gas less able to leave the tank, reducing flow. Also,

as the supply of hydrogen in the tank decreases, the flow paths through and around the carbon become more important. The PAC is packed so tightly that the ability for the hydrogen to diffuse through and around the sample is greatly diminished.

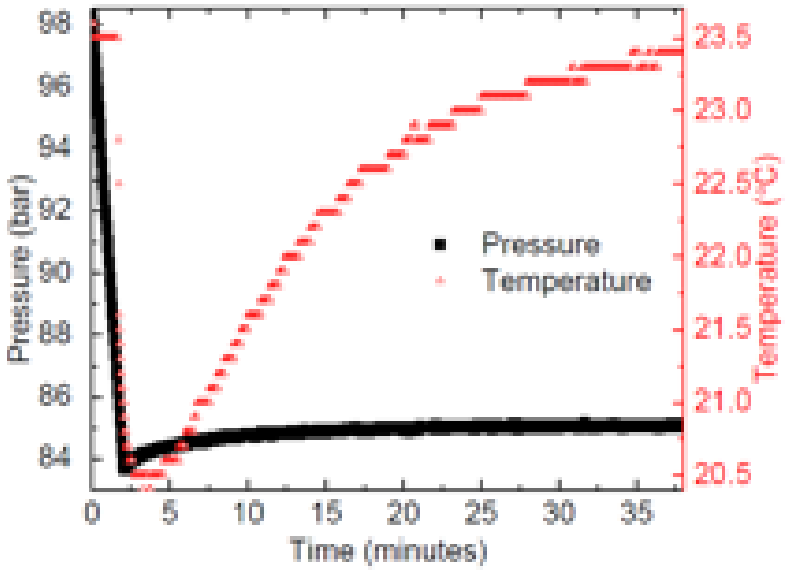

Figure 58. The temperature and pressure profiles are shown for the transition between 100 bar and 84 bar desorption data.

The pressure decreases from 100 bar to 84 bar in 2.5 minutes. During the discharge, the temperature dropped about 3℃. After about 40 minutes the tank appears to have thermally equilibrated.

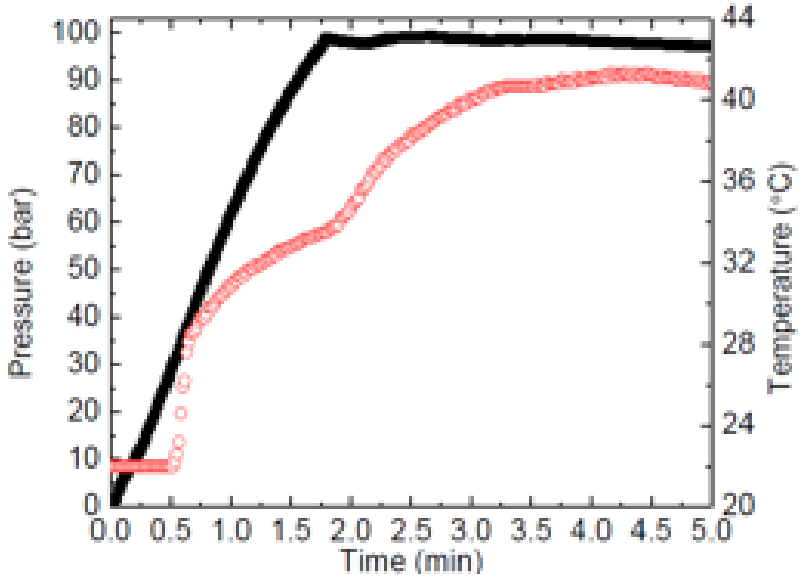

Figure 59. The pressure and temperature inside the 10LSS during a fast fill with PAC.

After 3.3 minutes of filling the 10LSS, 95% of the maximum gravimetric storage capacity was achieved. Despite the 28 cm inlet extensions, the temperature at the center of the tank trailed the application of pressure by 32 seconds. The extension tubes did allow the hydrogen to only have to diffuse through 13 cm of PAC to reach the center of the tank. Cusp and increase in slope of temperature vs time plot at 2 minutes are due to a reduction in gas flow into the system (**Figure 59**). At 3.3 minutes, the flow into the system was permanently stopped. Gas flowing into the system has a cooling effect which has lead others[88] to explore flow-through cooling to aid in removing heat from hydrogen adsorbent systems during filling.

7.2 Monolith Fast Fill and Discharge at 296 and 273 K

This section is an examination of the dynamics of filling the 10LSS from 2-100 bar as quickly as possible at room temperature and 0 ºC. These experiments were broken up into four segments. The segments are the fast fill (2-100 bar), the following thermal equilibration, the fast discharge of the

tank (100-2 bar), and the following thermal equilibration. These measurements are new work that is original to this document.

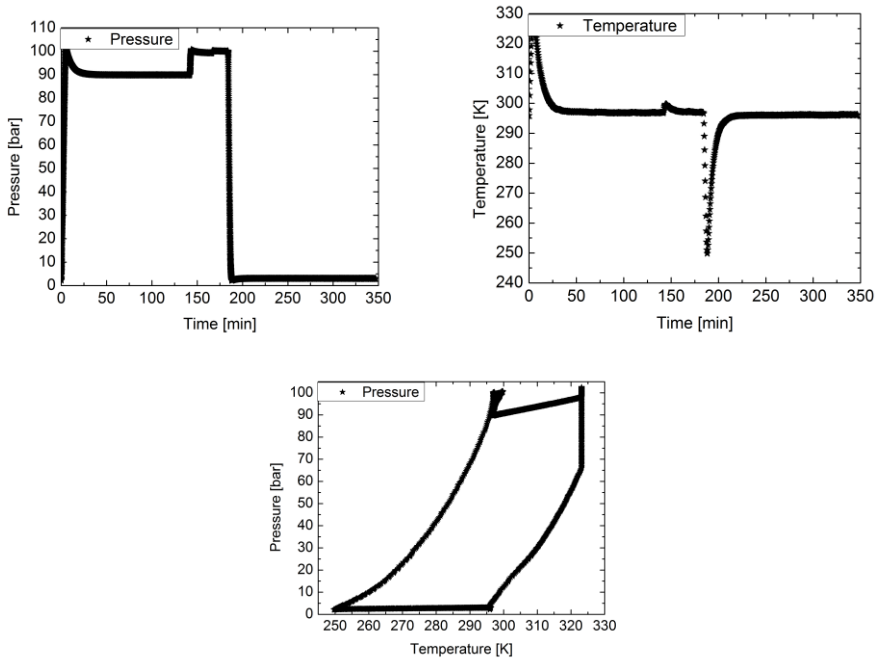

Figure 60. 296 K fast fill and discharge total cycle. *Left*: Pressure vs time. *Right:* Temperature vs time. *Bottom:* Pressure vs temperature.

The plots for the entire cycle are shown above. The sharp peaks on the pressure vs time and temperature vs time graphs are when the primary filling (first 5 minutes) and discharging (at 175 minutes) occur. The flat regions of the graph are when the tank achieved thermal equilibration. The smaller features on both graphs (between 125 and 150 minutes) occur due to filling the tank back up to 100 bar, because the pressure dropped from the tank cooling. Below is a more in-depth analysis of each region.

Fast Fill 2-100 bar:

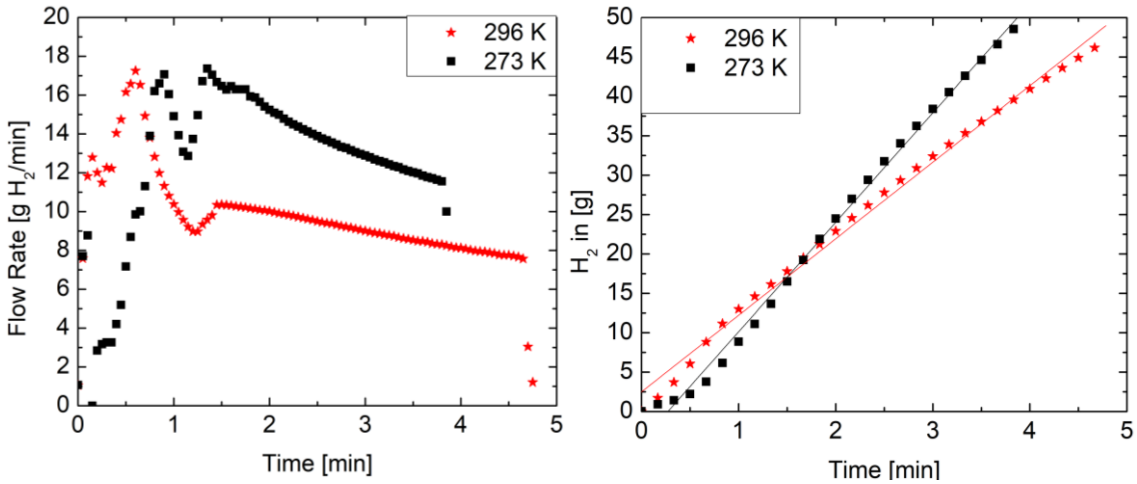

Figure 61. Hydrogen flow rate for both temperatures during the fast fill. *Left*: Flow rate into the tank vs time. *Right:* Hydrogen filled into the tank vs time.

Prior to filling, the lines were pressurized to 2 bar. The tank was opened and the pressure booster was turned on the highest setting. The maximum flow rates the flow meter can handle is 18 g/min. A constant flow rate of 18 g/min could not be maintained due to the time required to boost the supply pressure (average flow of 9.7 g/min), see **Figure 61**. After peaking at 18 g/min around 3 seconds in, the flow rate leveled off around 10 g/min for the remainder of the fill (average flow of 12.6 g/min). The 273 K fill flow rate was kept higher than the bulk of the room temperature fill. Some of this is likely due to some tweaking of the pressure booster settings. After peaking at 18 g/min around 1 minute in, the flow rate steadily decreased, but never dropped as low as 10 g/min. The tank reached 100 bar after about 5 minutes (21.6 bar/min) and 4 minutes (28.2 bar/min) for 296 K and 273 K, respectively (**Figure 62**) and the tank was filled ~94% maximum capacity (9.7 and 13.9 g/min slope) (**Figure 61**).

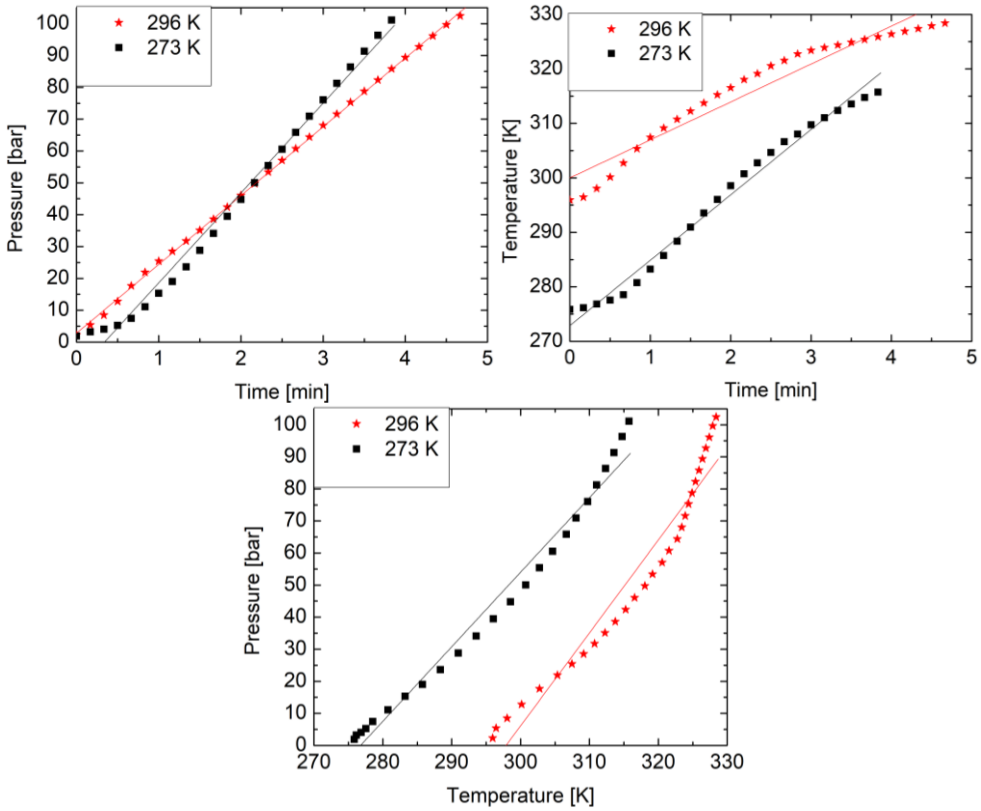

Figure 62. Fast fill pressure and temperature for both temperatures. *Left*: Pressure vs time. *Right:* Temperature vs time. *Bottom:* Pressure vs temperature.

The maximum temperatures observed were 56 ℃ (6.9 ℃/min) and 42 ℃ (12.0 ℃/min) for 296 K and 273 K, respectively. These large temperature excursions are due to the rapid adsorption in addition to the high binding energy sites being occupied. $\Delta P/\Delta T$ were 2.9 bar/ ℃ and 2.3 bar/ ℃.

Fast Fill Thermal Equilibration:

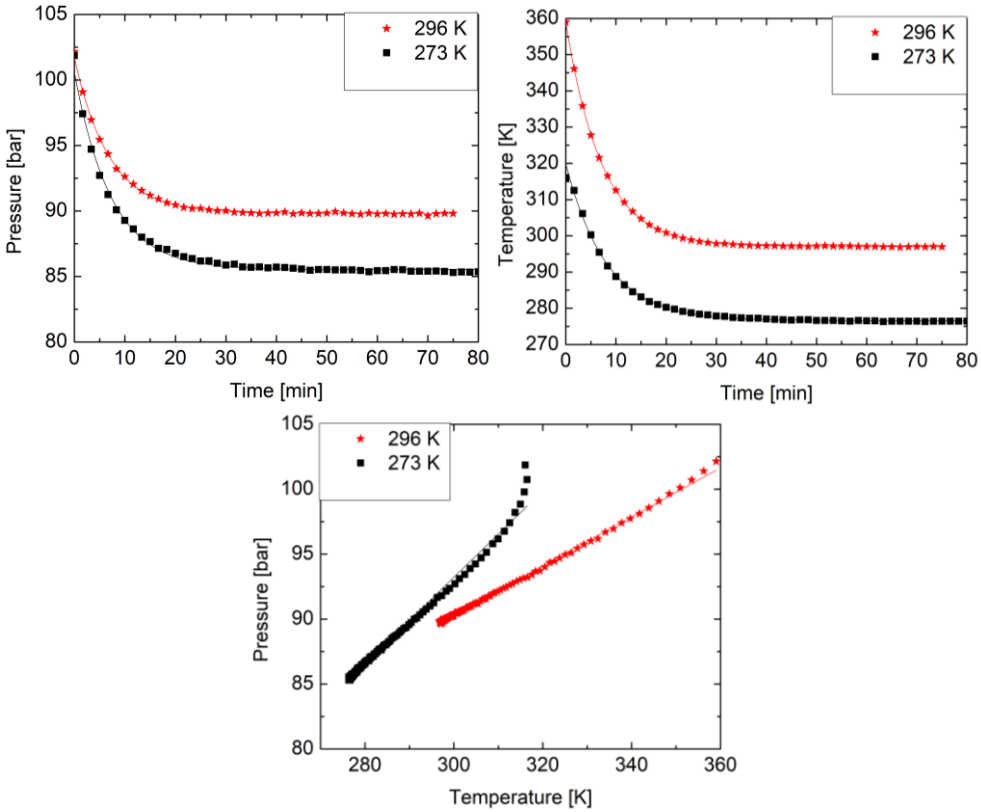

Figure 63. Fast fill thermal equilibration for both temperatures. *Left*: Pressure vs time. *Right:* Temperature vs time. *Bottom:* Pressure vs temperature.

Once the fill was complete, the tank was closed off in order to monitor the thermal equilibration of the tank. For the 296 K fill, data was collected for 70 minutes to ensure full equilibration. Both graphs for pressure and temperature appear to fit an exponential decay well (time constants 6.9 min and 7.2 min, respectively). The pressure drops around 10 bar during equilibration. The pressure vs temperature graph appears to be linear (Slope = 0.19 bar/℃).

For the 273 K fill, data was collected for 90 minutes to ensure full equilibration. Both graphs for pressure and temperature appear to fit an exponential decay well (time constants 7.2 min and 8.1

min, respectively). The pressure drops around 14 bar during equilibration. The pressure vs temperature graph appears to be linear (Slope = 0.33 bar/℃).

Fast Discharge 100-2 bar:

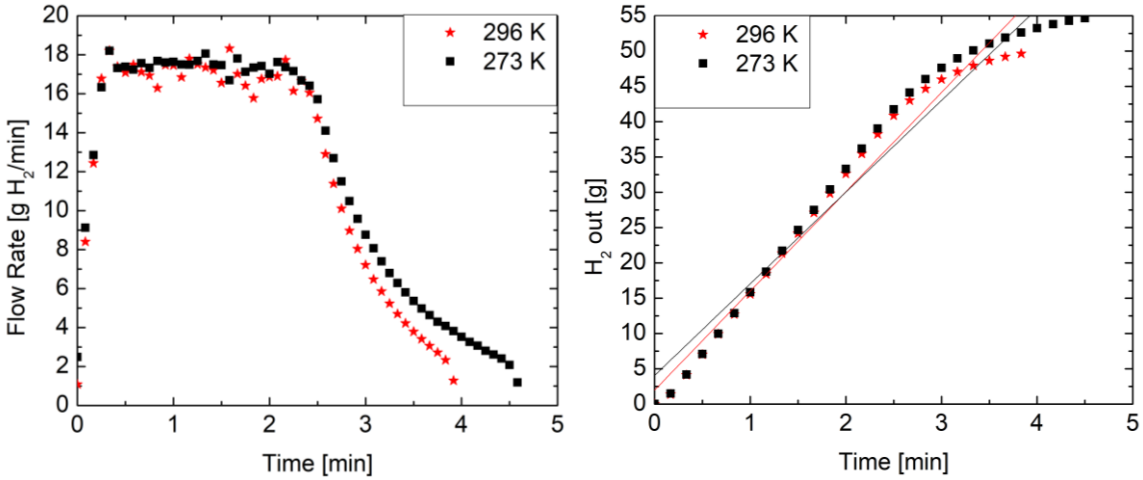

Figure 64. Fast discharge flow rate and mass of hydrogen discharged over time for each temperature.

After the tank equilibrated from being topped off to 100 bar, the lines were filled to 100 bar and the tank was opened. The discharge flow was controlled to not exceed 18 g/min. The tank provided a much more consistent flow until after 2 minutes, then the flow began to decrease (average flow of 12.6 and 11.8 g/min) (**Figure 64**). The tank was able to empty to 2 bar in just 4 minutes (26.2 bar/min) and 4.5 minutes (21.4 bar/min) for 296 K and 273 K, respectively (**Figure 65).**

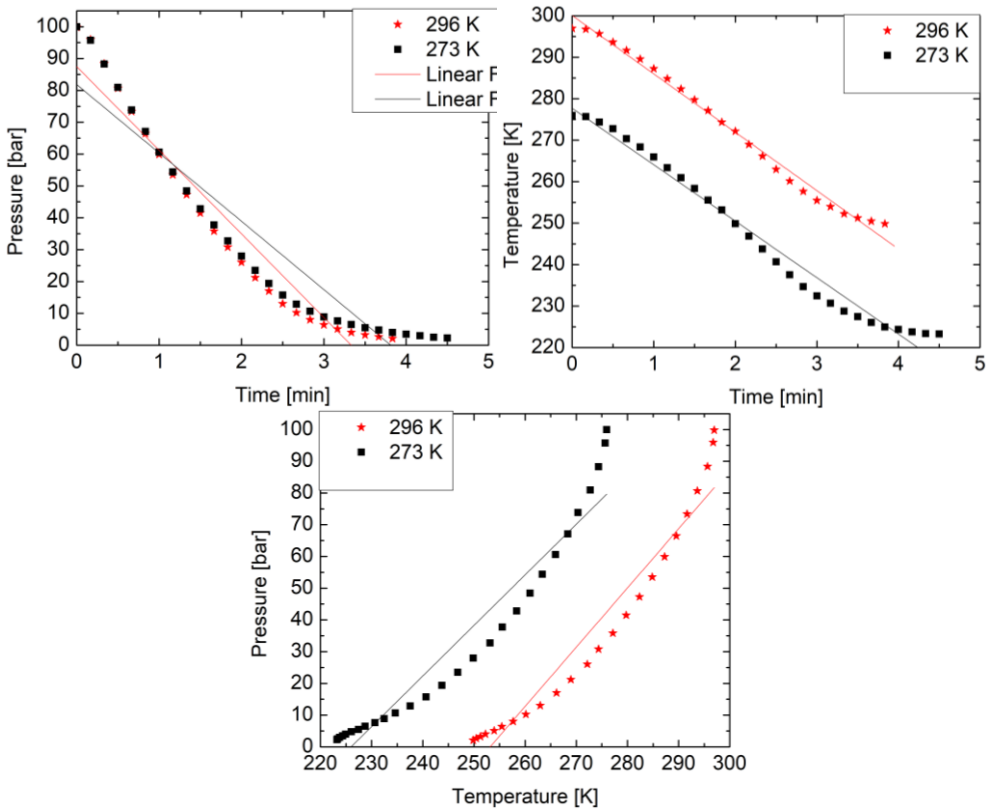

Figure 65. Fast discharge pressure and temperature for each temperature. *Left*: Pressure vs time. *Right:* Temperature vs time. *Bottom:* Pressure vs temperature.

The minimum temperatures observed were -25 ℃ (-14.1 ℃/min) and -50 ℃ (-13.6 ℃/min) for 296 K and 273 K, respectively. These large temperature excursions are due to the rapid desorption in addition to the high binding energy sites being vacated. $\Delta P/\Delta T$ were 1.9 bar/℃ and 1.6 bar/℃. (**Figure 65**).

Fast Discharge Thermal Equilibration:

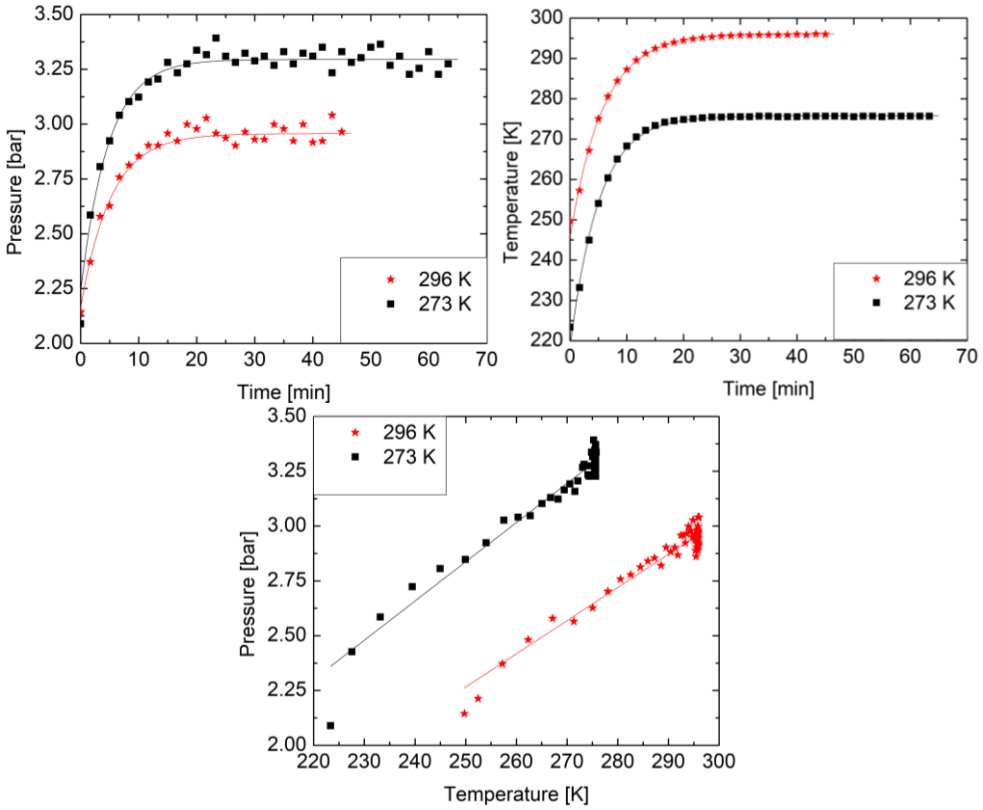

Figure 66. Fast discharge thermal equilibration for each temperature. *Left*: Pressure vs time. *Right:* Temperature vs time. *Bottom:* Pressure vs temperature.

Once the tank reached 2 bar, the tank was closed off in order to monitor the thermal equilibration of the tank. For the 296 K fill, data was collected for 50 minutes to ensure full equilibration. Both graphs for pressure and temperature appear to fit an exponential decay well (time constants 5.2 min and 5.8 min, respectively). The pressure drops around 10 bar during equilibration. The pressure vs temperature graph appears to be linear (Slope = 0.015 bar/℃).

For the 273 K fill, data was collected for 60 minutes to ensure full equilibration. Both graphs for pressure and temperature appear to fit an exponential decay well (time constants 4.8 min and 5.1

min, respectively). The pressure drops around 14 bar during equilibration. The pressure vs temperature graph appears to be linear (Slope = 0.018 bar/℃).

Table 13. Summary of Fast Fill and Discharge Experiments

	Filling or Discharging		**Thermal Equilibration**		
Configuration	**Time (min)**	**Max/min T (K)**	**Time constant P (min)**	**Time constant T (min)**	**Slope P vs T (bar/℃)**
Fill 2-100 bar 296 K	4.8	329	6.9	7.2	0.19
Discharge 100-2 bar 296 K	4	248	5.2	5.8	0.015
Fill 2-100 bar 273 K	3.9	315	7.3	8.1	0.33
Discharge 100-2 bar 273 K	4.6	223	4.8	5.1	0.018

Table 14. Summary of the Thermal Conductivities of Carbon Materials and Calculated Time Constants

Material	**Thermal Conductivity (W/mK)**	**Δt (min) radial**
Graphene	(4840±440)-(5300±480) [89]	0.29-0.27
Graphite	25-470 [90]	57-3.0
Longitudinal	146-246	9.8-5.8
Radial	92-175	15-8.1
Carbon nanotubes (bulk)	2.5-35-200 [91]	570-41-7.1
Carbon nanotubes (single)	3180-3500 [92–95]	0.45-0.41

The time constants were calculated by

$$\Delta t \approx \frac{c_{\mathrm{m}} \rho_{\mathrm{bulk}} A}{K_{\mathrm{th}}} \tag{37}$$

where c_{m} is the specific heat of graphite (0.7 J/gK), ρ_{bulk} is the bulk density (mass of carbon/volume of tank), A is the surface area (radial $2\pi rh$ or longitudinal πr^2), and K_{th} is the thermal conductivity. The time constants measured from the 10LSS kinetic data range from 5-8 min. Using this range of times, the thermal conductivities are 280-180 W/mK (radial) and 7.8-4.9 W/mK (longitudinal). Since the radial thermal conductivities are within the range of values for graphite (25-470 W/mK) and near the value others have measured graphitic samples to be (337 W/mK) [96], our monoliths are quite graphite-like.

The process of compressing the activated carbon into monoliths seems to align graphite sheets perpendicular to the direction of compression (z-axis). Thus, the predominant direction of the heat transport is radially outward from the cylindrical monoliths. This is similar to bulk carbon nanotubes (single wall, aligned mats) both in alignment interpretation and thermal conductivity (200 W/mK). This shows that our carbon monoliths are quite graphitic and show signs of aligned sheets in the bulk material. These ranges of thermal conductivities reflect the difference in thermal transport in the basal plane (1900 W/mK) vs the c-axis (0.0131W/mK) [97].

8 Conclusions

In this paper we are able to determine some important microscopic characteristics of an adsorbed film from cryogenic adsorption isotherms at high coverage and use these properties to reliably calculate the enthalpy of adsorption for the system at both cryogenic and room temperatures. In particular, we observed that the density of the adsorbed film at saturation $\rho_{\mathrm{film,sat}}$ ($\approx$ 100 g/L for hydrogen, higher than its liquid) is remarkably sample and temperature independent (i.e., a property of the adsorbate), thus its cryogenic determination for one sample should provide a reasonable estimate for almost any sample or temperature. The knowledge of the saturation density was then

used as a fixed point in fitting the Ono-Kondo model to high temperature adsorption data and extrapolate to inaccessible large gas densities, which allowed us to determine the volume occupied by the adsorbed film V_{film}, which was previously unknown. We observed a linear dependence of V_{film} on the specific surface area, and a marked decrease of V_{film} with increasing temperature ($V_{\mathrm{film}} \approx 0.40\ V_{\mathrm{pore}}$ under cryogenic conditions, and $V_{\mathrm{film}} \approx 0.12\ V_{\mathrm{pore}}$ at room temperature). This is understood in terms of the relative population of shallower vs. deeper binding sites and the structure of these. Knowledge of V_{film} permits the calculation of the absolute adsorption, and thus a reliable calculation of the enthalpy of adsorption using Clausius-Clapeyron relation (its value at room temperature, 8.3 kJ/mol agreed within 1.2% of the deepest adsorption sites measured at 77 K). The enthalpy of adsorption thus determined has a much lower uncertainty than the large range permitted by the most common assumptions, and lacks the unphysical rise with coverage sometimes reported.

The fact that the saturated film density is quite robust implies that our determination, coupled with the proposed methodology, may be applied to calculate important properties such as the enthalpy of adsorption of other adsorbents without the cost or effort of cryogenic refrigeration or very large pressures (which may have increased uncertainty in the determination of adsorption isotherms).

First isothermal measurements on a 3 kg sample at 296 K, 273 K, and 198 K were performed using the 10LSS with great precision. This data agrees within 2% with measurements on the Hiden, as well as theoretical predictions. In addition, the first large-scale hydrogen filling and discharging experiments were performed at two different temperatures. Fast fill and discharge data were collected at 296 K and 273 K including tank equilibration behavior. The equilibration time constants ranged from 4.8-8.1 min. This range of values corresponds to thermal conductivities lower than most estimates of graphene, but appears more graphitic than some other activated carbons (280-180 W/mK). These values are well within the range of graphitic samples and of a

high enough order of magnitude to infer the thermal transport is in the basal plane and not the c-axis. This adds credibility to the claim that through the compression process the monoliths appear to transport like sheets of graphite stacked perpendicular to the direction of compression. Filling and discharging could reach the desired target pressure in less than 5 minutes with 94% total capacity filled or delivered, satisfying the DOE target for fill time. During these fills/discharges internal tank temperatures would increase/decrease by ~50 ℃.

A methodology was developed in order to analyze the operating pressure and temperature dependence of deliverable storage, a new metric which had not been thoroughly investigated. Isobaric data for the volumetric storage capacity exhibited a clear exponential decay with increasing temperature. Additionally, the monoliths stopped increasing the deliverable storage capacity at 77 K. This indicates that there are temperatures low enough that the gains made in absolute storage cannot be reversed from the tank without pumping or heating. It was shown that the differences between tank and crystal porosity did not have an effect on the deliverable storage capacity. However, the higher porosity PAC not only was outperformed by the monolith adsorbent, but did not outperform compression for a large range of pressures and temperatures. It was determined that a tank operating from 35-1 bar was maximized over compressed gas (2.54x) at a temperature of 136 K. A tank operating from 200-2 bar was maximized over compressed gas (1.25x), but at a much higher temperature of 183 K. So, depending on the goal of increasing operating temperature or maximizing the benefits over compressed gas, these methods can help inform the choice of adsorbent material (carbon-based, MOF, etc.) and tank operating pressures.

9 Bibliography

[1] G. Saur, A. Milbrandt, Renewable hydrogen potential from biogas in the United States, National Renewable Energy Laboratory, Golden, CO, 2014. http://citeseerx.ist.psu.edu/viewdoc/download?doi=10.1.1.644.5489&rep=rep1&type=pdf.

[2] K. Field, Hydrogen Fuel Cell & Battery Electric Vehicles — Technology Rundown, Clean Tech. (2018). https://cleantechnica.com/2018/08/11/hydrogen-fuel-cell-battery-electric-vehicles-technology-rundown/.

[3] G. Thomas, Overview of storage development DOE hydrogen program, Sandia Natl. Lab. 9 (2000).

[4] Department of Energy Office of Fuel Cell Technologies, Hydrogen Storage, (2018). https://www.energy.gov/eere/fuelcells/hydrogen-storage.

[5] K. Field, Toyota Mirai Hydrogen Fuel Cell Vehicle Review, Clean Tech. (2018). https://cleantechnica.com/2018/06/16/toyota-mirai-hydrogen-fuel-cell-vehicle-review-cleantechnica-exclusive/.

[6] U. Eberle, B. Müller, R. von Helmolt, Fuel cell electric vehicles and hydrogen infrastructure: status 2012, Energy Environ. Sci. 5 (2012) 8780–8798. doi:10.1039/c2ee22596d.

[7] G.D. Berry, S.M. Aceves, Onboard storage alternatives for hydrogen vehicles, Energy Fuels. 12 (1998) 49–55. doi:10.1021/ef9700947.

[8] J. Burress, M. Kraus, M. Beckner, R. Cepel, G. Suppes, C. Wexler, P. Pfeifer, Hydrogen storage in engineered carbon nanospaces, Nanotechnology. 20 (2009) 204026. doi:10.1088/0957-4484/20/20/204026.

[9] J. Rouquerol, F. Rouquerol, K.S.W. Sing, Adsorption by Powders and Porous Solids: Principles, Methodology and Applications, Academic Press, 1998.

[10] P. Pfeifer, J.W. Burress, M.B. Wood, C.M. Lapilli, S.A. Barker, J.S. Pobst, R.J. Cepel, C. Wexler, P.S. Shah, M.J. Gordon, G.J. Suppes, S.P. Buckley, D.J. Radke, J. Ilavsky, A.C. Dillon, P.A. Parilla, M. Benham, M.W. Roth, High-Surface-Area Biocarbons for Reversible On-Board Storage of Natural Gas and Hydrogen, in: MRS Proc., 2007. doi:10.1557/PROC-1041-R02-02.

[11] M. Golebiowska, M. Roth, L. Firlej, B. Kuchta, C. Wexler, The reversibility of the adsorption of methane–methyl mercaptan mixtures in nanoporous carbon, Carbon. 50 (2012) 225–234. doi:10.1016/j.carbon.2011.08.039.

[12] R.D. McCarty, J. Hord, H. Roder, Selected properties of hydrogen (engineering design data), National Bureau of Standards, 1981.

[13] L.J. Murray, M. Dincă, J.R. Long, Hydrogen storage in metal–organic frameworks, Chem. Soc. Rev. 38 (2009) 1294–1314. doi:10.1039/b802256a.

[14] L. Firlej, S. Roszak, B. Kuchta, P. Pfeifer, C. Wexler, Enhanced hydrogen adsorption in boron substituted carbon nanospaces, J. Chem. Phys. 131 (2009) 164702. doi:10.1063/1.3251788.

[15] B. Kuchta, L. Firlej, P. Pfeifer, C. Wexler, Numerical estimation of hydrogen storage limits in carbon-based nanospaces, Carbon. 48 (2010) 223–231. doi:10.1016/j.carbon.2009.09.009.

[16] B. Kuchta, L. Firlej, S. Roszak, P. Pfeifer, A review of boron enhanced nanoporous carbons for hydrogen adsorption: numerical perspective, Adsorption. 16 (2010) 413–421. doi:10.1007/s10450-010-9235-0.

[17] B. Kuchta, L. Firlej, R. Cepel, P. Pfeifer, C. Wexler, Structural and energetic factors in designing a nanoporous sorbent for hydrogen storage, Colloids Surf. Physicochem. Eng. Asp. 357 (2010) 61–66. doi:10.1016/j.colsurfa.2010.01.020.

[18] A.J. Lachawiec, G. Qi, R.T. Yang, Hydrogen Storage in Nanostructured Carbons by Spillover: Bridge-Building Enhancement, Langmuir. 21 (2005) 11418–11424. doi:10.1021/la051659r.

[19] J. Romanos, M. Beckner, T. Rash, L. Firlej, B. Kuchta, P. Yu, G. Suppes, C. Wexler, P. Pfeifer, Nanospace engineering of KOH activated carbon, Nanotechnology. 23 (2012) 015401. doi:10.1088/0957-4484/23/1/015401.
[20] H. Deng, S. Grunder, K.E. Cordova, C. Valente, H. Furukawa, M. Hmadeh, F. Gandara, A.C. Whalley, Z. Liu, S. Asahina, H. Kazumori, M. O'Keeffe, O. Terasaki, J.F. Stoddart, O.M. Yaghi, Large-Pore Apertures in a Series of Metal-Organic Frameworks, Science. 336 (2012) 1018–1023. doi:10.1126/science.1220131.
[21] M. Donohue, G. Aranovich, Classifications of Gibbs Adsorption Isotherms, Adv. Colloid Interface Sci. 76–77 (1998) 137–152. doi:doi.org/10.1016/S0001-8686(98)00044-X.
[22] P. Bénard, R. Chahine, Modeling of High-Pressure Adsorption Isotherms above the Critical Temperature on Microporous Adsorbents: Application to Methane, Langmuir. 13 (1997) 808–813. doi:10.1021/la960843x.
[23] J.E. Jones, On the Determination of Molecular Fields. II. From the Equation of State of a Gas, Proc. R. Soc. Math. Phys. Eng. Sci. 106 (1924) 463–477. doi:10.1098/rspa.1924.0082.
[24] W.H. Keesom, Two theorems concerning the second virial coefficient for rigid spherical molecules which besides collisional forces only exert Coulomb-forces and for which the total charge of the active agent is zero, in: KNAW Proc., Amsterdam, 1915: pp. 868–871.
[25] W.H. Keesom, in: KNAW Proc., Amsterdam, 1920.
[26] W.H. Keesom, Van der Waals attractive force, Phys. Z. 22 (1921).
[27] W.H. Keesom, Die Berechnung der molekularen Quadrupol-momente aus der Zustandsgieichung, Phys. Z. 23 (1922).
[28] P. Debye, Die van der Waalsschen Kohasion-skrafte, Phys. Z. 21 (1920).
[29] P. Debye, Molecular forces and their electrical interpretation, Phys. Z. 22 (1921).
[30] F. London, Zur theorie und systematik der molekularkräfte, Phys. Z. 63 (1930).
[31] F. London, Über einige eigenschaften und anwendungen der molekularkräfte, Z. Für Phys. Chem. 11 (1930).
[32] F. London, The general theory of molecular forces, Trans. Faraday Soc. 33 (1937).
[33] J.T.G. Overbeek, M.J. Sparnaay, Experiments on long-range attractive forces between macroscopic objects, J. Colloid Sci. 7 (1952) 343–345.
[34] K.L. Mittal, Physicochemical Aspects of Polymer Surfaces: Volume 1, Springer US, Boston, MA, 1983. http://public.eblib.com/choice/publicfullrecord.aspx?p=3083266 (accessed October 16, 2018).
[35] H.C. Hamaker, The London—van der Waals attraction between spherical particles, Physica. 4 (1937) 1058–1072.
[36] H.B.G. Casimir, D. Polder, The Influence of Retardation on the London-van der Waals Forces, Phys. Rev. Lett. 73 (1948).
[37] T.L. Hill, Physics, An Introduction to Statistical Thermodynamics, unknown edition, Dover Publications, New York, 1987.
[38] A.M.J.F. Michels, P.G. Menon, C.A. Seldam, Adsorption of nitrogen on alumina at high pressure, Recl. Trav. Chim. Pays-Bas. 80 (1961) 483–501. doi:doi.org/10.1002/recl.19610800504.
[39] D.P. Broom, The accuracy of hydrogen sorption measurements on potential storage materials, Int. J. Hydrog. Energy. 32 (2007) 4871–4888. doi:10.1016/j.ijhydene.2007.07.056}.
[40] A. Gillespie, Properties of Adsorbed Hydrogen and Methane Films on Nanoporous Solids, University of Missouri–Columbia, 2017.
[41] BS EN, Natural Stone Test Methods. Determination of Real Density and Apparent Density and of Total and Open Porosity., (2006). https://www.scribd.com/document/276530524/BS-en-1936-1999-Natural-Stone-Test-Methods-Determination-of-Real-Density-and-Apparent-Density-and-of-Total-and-Open-Porosity-1.

[42] T.A. Rash, A. Gillespie, B.P. Holbrook, L.H. Hiltzik, J. Romanos, Y.C. Soo, S. Sweany, P. Pfeifer, Microporous carbon monolith synthesis and production for methane storage, Fuel. 200 (2017) 371–379. doi:10.1016/j.fuel.2017.03.037.
[43] M.J. Prosniewski, T.A. Rash, E.W. Knight, A.K. Gillespie, D. Stalla, C.J. Schulz, P. Pfeifer, Controlled charge and discharge of a 40-L monolithic adsorbed natural gas tank, Adsorption. 24 (2018) 541–550. doi:10.1007/s10450-018-9961-2.
[44] P. Pfeifer, R. Little, T. Rash, J. Romanos, B. Maland, Advanced Natural Gas Fuel Tank Project, California Energy Commission, Sacramento, 2016.
[45] P. Pfeifer, C. Wexler, G. Suppes, F. Hawthorne, S. Jalisatgi, M. Lee, D. Robertson, Multiply Surface-Functionalized Nanoporous Carbon for Vehicular Hydrogen Storage, (2011). https://www.hydrogen.energy.gov/pdfs/review11/st019_pfeifer_2011_o.pdf.
[46] P. Pfeifer, A.K. Gillespie, D. Stalla, E. Dohnke, Multiply Surface-Functionalized Nanoporous Carbon for Vehicular Hydrogen Storage—Final Technical Report., U.S. Department of Energy, Washington, DC, 2017. https://www.osti.gov/scitech/biblio/1344383.
[47] L. Schlapbach, A. Züttel, Hydrogen-storage materials for mobile applications, Nature. 414 (2001) 353–358. doi:10.1038/35104634.
[48] P. Bénard, R. Chahine, Modeling of Adsorption Storage of Hydrogen on Activated Carbons, Int. J. Hydrog. Energy. 26 (2001) 849–855.
[49] N. Shang, P. Papakonstantinou, P. Wang, S. Ravi, P. Silva, Platinum Integrated Graphene for Methanol Fuel Cells, J. Phys. Chem. 114 (2010) 15837–15841. doi:10.1021/jp105470s.
[50] H.K. Chae, D.Y. Siberio-Perez, J. Kim, Y. Go, M. Eddaoudi, A.J. Matzger, M. O'Keeffe, O.M. Yaghi, A route to high surface area, porosity and inclusion of large molecules in crystals, Nature. 427 (2004) 523–527. doi:10.1038/nature02311.
[51] M. Beckner, A. Dailly, Adsorption Enthalpy Calculations of Hydrogen Adsorption at Ambient Temperature and Pressures Exceeding 300 bar, Am. J. Anal. Chem. 04 (2013) 8–16. doi:10.4236/ajac.2013.410A3002.
[52] A. Myers, P. Monson, Physical adsorption of gases: The case for absolute adsorption as the basis for thermodynamic analysis, Adsorption. 20 (2014) 591–622. doi:10.1007/s10450-014-9604-1.
[53] G. Aranovich, M. Donohue, Determining Surface Areas from Linear Adsorption Isotherms at Supercritical Conditions, J. Colloid Interface Sci. 194 (1997) 392–397. doi:doi.org/10.1006/jcis.1997.5099.
[54] D. Saha, Z. Wei, S. Deng, Equilibrium, kinetics and enthalpy of hydrogen adsorption in MOF-177, Int. J. Hydrog. Energy. 33 (2008) 7479–7488. doi:10.1016/j.ijhydene.2008.09.053.
[55] N.P. Stadie, M. Murialdo, C.C. Ahn, B. Fultz, Anomalous Isosteric Enthalpy of Adsorption of Methane on Zeolite-templated Carbon, J. Am. Chem. Soc. 135 (2013) 990–993. doi:10.1021/ja311415m.
[56] E. Poirier, A. Dailly, Thermodynamics of Hydrogen Adsorption in MOF-177 at Low Temperatures: Measurements and Modelling, Nanotechnology. 20 (2009). doi:10.1088/0957-4484/20/20/204006.
[57] O. Redlich, D.L. Peterson, A Useful Adsorption Isotherm, J. Phys. Chem. 63 (1959) 1024–1024. doi:10.1021/j150576a611.
[58] E. Dohnke, On the High Density Hydrogen Films Adsorbed in Carbon Nanospaces, University of Missouri–Columbia, 2015. https://mospace.umsystem.edu/xmlui/handle/10355/49088.
[59] R.S. Farr, R.D. Groot, Close packing density of polydisperse hard spheres, J. Chem. Phys. 131 (2009) 244104. doi:10.1063/1.3276799.
[60] P. Pfeifer, C. Wexler, P. Yu, G. Suppes, F. Hawthorne, S. Jalisatgi, M. Lee, D. Robertson, DOE 2012 Annual Progress Report Hydrogen Program IV.C.3: Multiply Surface-

Functionalized Nanoporous Carbon for Vehicular Hydrogen Storage, (2012). https://www.hydrogen.energy.gov/pdfs/progress12/iv_c_3_pfeifer_2012.pdf.
[61] T. Otowa, R. Tanibata, M. Itoh, Production and Adsorption Characteristics of MAXSORB: High-Surface Area Active Carbon, Gas Sep. Purif. 7 (1993) 241–245. doi:doi.org/10.1016/0950-4214(93)80024-Q.
[62] M.E. Casco, M. Martínez-Escandell, E. Gadea-Ramos, K. Kaneko, J. Silvestre-Albero, F. Rodríguez-Reinoso, High-Pressure Methane Storage in Porous Materials: Are Carbon Materials in the Pole Position?, Chem. Mater. 27 (2015) 959–964. doi:10.1021/cm5042524.
[63] F.S. Baker, Production of highly microporous activated carbon products, US5416056 A, 1995. http://www.google.com/patents/US5416056 (accessed January 17, 2017).
[64] F.S. Baker, R.K. Beckler, J.R. Miller, Z.Q. Yan, Highly microporous carbons and process of manufacture, US5965483 A, 1999. http://www.google.com/patents/US5965483 (accessed January 17, 2017).
[65] E.D. Tolles, R.L. Stallings, C.E. Miller, Process for making activated carbon with control of metal ion concentration in phosphoric acid, Google Patents, 1979. http://www.google.com/patents/US4155878 (accessed January 17, 2017).
[66] F.S. Baker, C.E. Miller, A.J. Repik, E.D. Tolles, Carbon, Activated, in: Kirk-Othmer Encycl. Chem. Technol., John Wiley & Sons, Inc., 2000. http://onlinelibrary.wiley.com/doi/10.1002/0471238961.0103200902011105.a01.pub2/abstract (accessed January 17, 2017).
[67] P. Pfeifer, G. Suppes, P.S. Shah, J. Burress, High surface area carbon and process for its production, 8,691,177 B2, 2014.
[68] P. Pfeifer, G. Suppes, P.S. Shah, J. Burress, High surface area carbon and process for its production, 8,926,932 B2, 2015.
[69] S. Brunauer, P.H. Emmett, E. Teller, Adsorption of Gases in Multimolecular Layers, J. Am. Chem. Soc. 60 (1938) 309–319. doi:10.1021/ja01269a023.
[70] A. Neimark, P. Ravikovitch, Y. Lin, M. Thommes, Quenched solid density functional theory and pore size analysis of micro-mesoporous carbons, Carbon. 47 (2009) 1617–1628. doi:doi.org/10.1016/j.carbon.2009.01.050.
[71] P.I. Ravikovitch, A.V. Neimark, Density Functional Theory Model of Adsorption on Amorphous and Microporous Silica Materials, Langmuir. 22 (2006) 11171–11179. doi:10.1021/la0616146.
[72] M. Thommes, Physical Adsorption Characterization of Nanoporous Materials, Chem. Ing. Tech. 82 (2010) 1059–1073. doi:10.1002/cite.201000064.
[73] G. Gor, M. Thommes, K. Cychosz, A.V. Neimark, Quenched solid density functional theory method for characterization of mesoporous carbons by nitrogen adsorption, Carbon. 50 (2012) 1583–1590. doi:doi.org/10.1016/j.carbon.2011.11.037.
[74] Y. Zhu, S. Murali, M. Stoller, K. Ganesh, W. Cai, P. Ferreira, A. Pirkle, R. Wallace, K. Cychosz, M. Thommes, D. Su, E. Stach, R. Ruoff, Carbon-based supercapacitors produced by activation of graphene., Science. 332 (2011) 1537–1541. doi:doi: 10.1126/science.1200770.
[75] R.J. Olsen, L. Firlej, B. Kuchta, H. Taub, P. Pfeifer, C. Wexler, Sub-nanometer characterization of activated carbon by inelastic neutron scattering, Carbon. 49 (2011) 1663–1671. doi:10.1016/j.carbon.2010.12.051.
[76] R.J. Olsen, M. Beckner, M.B. Stone, P. Pfeifer, C. Wexler, H. Taub, Quantum excitation spectrum of hydrogen adsorbed in nanoporous carbons observed by inelastic neutron scattering, Carbon. 58 (2013) 46–58. doi:10.1016/j.carbon.2013.02.026.
[77] J. Romanos, M. Beckner, D. Stalla, A. Tekeei, G. Suppes, S. Jalisatgi, M. Lee, F. Hawthorne, J.D. Robertson, L. Firlej, B. Kuchta, C. Wexler, P. Yu, P. Pfeifer, Infrared study of boron–

carbon chemical bonds in boron-doped activated carbon, Carbon. 54 (2013) 208–214. doi:10.1016/j.carbon.2012.11.031.
[78] L. Firlej, B. Kuchta, A. Lazarewicz, P. Pfeifer, Increased H2 gravimetric storage capacity in truncated carbon slit pores modeled by Grand Canonical Monte Carlo, Carbon. 53 (2013) 208–215. doi:10.1016/j.carbon.2012.10.049.
[79] L. Ortiz, B. Kuchta, L. Firlej, M.W. Roth, C. Wexler, Methane adsorption in nanoporous carbon: the numerical estimation of optimal storage conditions, Mater. Res. Express. 3 (2016) 055011. doi:10.1088/2053-1591/3/5/055011.
[80] P. Pfeifer, G. Suppes, P. Shah, J. Burress, High surface area carbon and process for its production, 8691177, 2014.
[81] P. Pfeifer, G. Suppes, P. Shah, J. Burress, High surface area carbon and process for its production, 8926932, 2015.
[82] J.W. Leachman, R.T. Jacobsen, S.G. Penoncello, E.W. Lemmon, Fundamental equations of state for parahydrogen, normal hydrogen, and orthohydrogen, J. Phys. Chem. Ref. Data. 38 (2009) 721–748. doi:doi.org/10.1063/1.3160306.
[83] T. Rash, A Comprehensive Report on Preparing and Analyzing Adsorptive Materials Suitable for Hydrogen and Methane Storage, University of Missouri–Columbia, 2014. https://mospace.umsystem.edu/xmlui/handle/10355/48219.
[84] J. Burress, D. Bethea, B. Troub, Combination volumetric and gravimetric sorption instrument for high accuracy measurements of methane adsorption, Rev. Sci. Instrum. 88 (2017) 053902. doi:10.1063/1.4982889.
[85] M. Prosniewski, A. Gillespie, E. Knight, T. Rash, D. Stalla, J. Romanos, A. Smith, Evaluating methane adsorbed film densities on activated carbon in dynamic systems, J. Energy Storage. 20 (2018) 357–363. doi:10.1016/j.est.2018.10.017.
[86] M. Beckner, Hydrogen adsorption studies of engineered and chemically modified activated carbons, University of Missouri–Columbia, 2012. https://mospace.umsystem.edu/xmlui/handle/10355/35149 (accessed November 28, 2016).
[87] E. Poirier, A. Dailly, Investigation of the Hydrogen State in IRMOF-1 from Measurements and Modeling of Adsorption Isotherms at High Gas Densities, J. Phys. Chem. C. 112 (2008) 13047–13052. doi:10.1021/jp800981f.
[88] B. Hardy, C. Corgnale, R. Chahine, M.-A. Richard, S. Garrison, D. Tamburello, D. Cossement, D. Anton, Modeling of adsorbent based hydrogen storage systems, Int. J. Hydrog. Energy. 37 (2012) 5691–5705. doi:10.1016/j.ijhydene.2011.12.125.
[89] A.A. Balandin, S. Ghosh, W. Bao, I. Calizo, D. Teweldebrhan, F. Miao, C.N. Lau, Superior Thermal Conductivity of Single-Layer Graphene, Nano Lett. 8 (2008) 902–907. doi:10.1021/nl0731872.
[90] R.A. Buerschaper, Thermal and Electrical Conductivity of Graphite and Carbon at Low Temperatures, J. Appl. Phys. 15 (1944) 452–454. doi:10.1063/1.1707454.
[91] A. Agarwal, S. Bakshi, D. Lahiri, Carbon nanotubes : Reinforced metal matrix composites, 1st ed., CRC Press, 2017.
[92] P. Silotia, S. Dabas, A. Saxena, S.-P. Tewari, On the Thermal Conductivity of Single-Walled Carbon Nanotube Ropes, Soft Nanosci. Lett. 3 (2013) 7–10. doi:10.4236/snl.2013.31002.
[93] P. Kim, L. Shi, A. Majumdar, P.L. McEuen, Thermal Transport Measurements of Individual Multiwalled Nanotubes, Phys. Rev. Lett. 87 (2001). doi:doi.org/10.1103/PhysRevLett.87.215502.
[94] E. Pop, D. Mann, Q. Wang, K. Goodson, H. Dai, Thermal Conductance of an Individual Single-Wall Carbon Nanotube above Room Temperature, Nano Lett. 6 (2005) 96–100. doi:10.1021/nl052145f.

[95] S. Berber, Y.-K. Kwon, D. Tománek, Unusually High Thermal Conductivity of Carbon Nanotubes, Phys. Rev. Lett. 84 (2000) 4613–4616. doi:10.1103/PhysRevLett.84.4613.
[96] L.W. Wang, S.J. Metcalf, R.E. Critoph, R. Thorpe, Z. Tamainot-Telto, Thermal conductivity and permeability of consolidated expanded natural graphite treated with sulphuric acid, Carbon. 49 (2011) 4812–4819. doi:10.1016/j.carbon.2011.06.093.
[97] K. Sun, M.A. Stroscio, M. Dutta, Graphite C-axis thermal conductivity, Superlattices Microstruct. 45 (2009) 60–64. doi:10.1016/j.spmi.2008.11.018.

10 VITA

Ernest William Knight was born in November 1991 to Ernest Charles Knight and Vicki Knight in Naperville, Illinois. He spent his youth actively participating in Boy Scouts and Karate. He finished scouting with the rank of Star, and left Karate with a Sand Belt. In high school, Ernie played football and volleyball. He also enjoyed working on his project Bradley GT kit car with his father and his uncle Jeff. The three of them would attend Sunday car shows and Tuesday cruise nights to show off all their hard work. While still in high school, Ernie sat in on his father's Statistics for the Social Sciences course offered by Lewis University. He would have earned the top grade in the class, had he shown his work. One summer, Ernie worked for KeHe Food Distributors with his uncle Jeff. The work consisted of 10-hour days of welding and installing rack legs and safety gates in the warehouse. The money from the summer work was for Ernie and his father to travel to Dallas, Texas for that year's only performance of Ozzfest. In 2010, Ernie enrolled at Lewis University for his undergraduate studies. After taking AP Physics and Calculus in high school, Ernie breezed through his general university physics and calculus courses. It was Dr. Hooper's Particle Physics elective course that provided a first (of many) humbling experiences. During his sophomore year, Ernie began dating Kimberly Deasy. They spent time together cheering each other on during their intramural volleyball games. That summer, Ernie started a one-year internship at Argonne National Lab. He worked in the cryogenics group for their linear accelerator. In May 2014, Ernie graduated with the largest class of physics majors that Lewis University had seen and was one of three Lewis graduates that continued their physics education at Mizzou. That fall, Ernie passed the Qual at the PhD level on his first attempt, much to the chagrin of the other first year graduate students. Whenever Ernie had the chance to return home, he loved to spend time with his nephews Colton, Logan and Trevor. After four and a half years, Ernie graduated from the University of Missouri with his PhD on December 14, 2018.